UNIVERSIDAD POLITÉCNICA DE VALENCIA

DEPARTAMENTO DE COMUNICACIONES

Slow Light Effects in Photonic Integrated Circuits with Application to Microwave Photonics

Ph.D. THESIS

by

Juan Antonio Lloret Soler

Valencia, June 2012

UNIVERSITAT POLITÈCNICA DE VALÈNCIA

DEPARTAMENT DE COMUNICACIONS

Slow Light Effects in Photonic Integrated Circuits with Application to Microwave Photonics

Juan Antonio Lloret Soler, M.Sc.
Optical and Quantum Communications Group (OQCG)
ITEAM Research Institute
Universitat Politècnica de València (UPV)
Camí de Vera s/n, 46022 València, SPAIN
jualloso@upvnet.upv.es

Ph.D. Supervisors:
Prof. Salvador Sales Maicas
Prof. Francisco Ramos Pascual

Valencia, June 2012

In memorian of
C. B. O.

Ideas don't last long.
Something has to be done with them.

Santiago Ramón y Cajal
Nobel prize in 1906

Acknowledgements

I would like to express my warmest gratitude to my supervisors, professors Salvador Sales and Francisco Ramos. Both are an inexhaustible fountain of ideas and their valuable assistance have always helped me to keep my research in the right direction. Not only they have offered me the possibility to develop outstanding professional skills, but also and most important, a human experience that I will never forget.

I am pleased to thank professor José Capmany. His knowledge, highlight skills, experience and useful remarks have been crucial in many steps of this work. The whole staff of the *Optical and Quantum Communications Group* is also thanked for creating an ideal job atmosphere, since in most cases, the professional relationships have become in nice friendships. Special mention is deserved by my colleague and friend Juan Sancho, whom I have been extremely fortunate to work with. He has also been responsible for the success of this work and we have lived memorable moments during these years which will be unforgettable for me.

I am also deeply grateful to professor Geert Morthier, from *Universiteit Gent-imec*. For the second time and after 3 years, Prof. Morthier hosted me again in his group and he made me feel as an important part from the beginning. At this point, I wish to thank researchers from *imec* for their friendly attitude and nice collaborations, specially to Rajesh, Thijs and Pauline. Fruitful research together with meeting old colleagues have made special the time spent in Gent. My warmest gratitude also goes to all the colleagues being part in the GOSPEL project, specially to whom I have directly had the chance to collaborate with.

I would like to acknowledge all my friends, those from my home town and those met elsewhere in the world, for all their support in both good and difficult moments.

I feel an immeasurable gratitude to all my family, but in particular to my parents, sister and brother. They have always respected my decisions and encouraged me to accomplish them. I owe special gratitude to my parents, because I can never thank them enough all their effort and sacrifices. Despite my education period, I really feel that the most important and useful lessons in my life have been passed on by them. Hence, this work is dedicated to them.

Last but not least, I would like to thank Ángeles for her understanding, affection and love. She is a worthy person, because she accepts me for who I am, with both my goodness and faults. Everyday, she makes me feel like the luckiest guy in the world. This work is also dedicated to her.

Abstract

This PhD thesis focuses on the design and implementation of novel approaches with the aim of developing photonic-assisted RF signal processing tasks by exploiting slow and fast light (SFL) effects in different media. For this purpose, different technology platforms such as semiconductor waveguides, silicon-on-insulator (SOI) and III-V compounds based resonant-type structures have been investigated. In this work, RF photonic phase shifting and true time delaying line functionalities have been proposed and demonstrated in the microwave and millimetre spectral bands. Analytical and numerical models, properly validated through experimental results, have been performed so as to describe the behavior of the proposed approaches in the context of delay/phase-shift features as a function of the delay/phase-shift tunable mechanism. A noise performance evaluation of semiconductor-based microwave photonics (MWP) phase shifting stages has been accomplished. A customized MWP phase shifting stage has been presented resulting in noise performance enhancement while keeping unaltered the functionality as a phase shifter. Different approaches implementing RF signal processing tasks have also been demonstrated through the use of SOI microring resonators (MRR). A novel concept enabling bandwidth enlargement on certain MWP signal processors based on a modification of the so-called separate carrier tuning (SCT) technique has been introduced. In addition, the implementation of photonic-assisted RF and data signal processors has been addressed by exploiting SFL effects in III-V-on-Si microdisk resonators (MDR). The design, technology and fabrication of this device have been detailed in-depth. All the proposed SFL-based approaches have been integrated as key elements in the implementation of more complex signal processing tasks, such as, tunable and reconfigurable complex-valued multi-tap MWP filters, multi-channel true time delaying tunable lines operating at high aggregate bit rates or high-bandwidth phase modulators. Finally, the performance of the developed signal processors have been evaluated with respect of significant figures of merit.

Resumen

Esta tesis doctoral tiene como objetivo el diseño y la implementación de dispositivos ópticos novedosos capaces de realizar tareas de procesado de señales de radiofrecuencia, concretamente en las bandas de microondas y milimétricas, explotando para ello efectos de luz lenta que tienen lugar sobre algunos medios físicos que presentan características especiales. Con este propósito, se han investigado estructuras basadas en tecnología de semiconductor en guiaonda, además de estructuras de naturaleza resonante sobre circuitos en silicio y compuestos híbridos fabricados con materiales activos pertenecientes a los grupos III-V sobre silicio. En concreto, se han propuesto diferentes circuitos ópticos capaces de desarrollar tareas propias de desfasador y retardador verdadero de banda ancha para señales de radiofrecuencia. El comportamiento de dichos circuitos ópticos bajo estudio se ha caracterizado mediante modelado teórico, quedando éstos adecuadamente validados a través de resultados experimentales. En primer lugar, se han llevado a cabo estudios concernientes a la degradación producida por ruido en estructuras desfasadoras formadas por amplificadores ópticos de semiconductor. Como resultado, se ha propuesto una nueva estructura que ha revertido en un rendimiento optimizado en términos de ruido sin que ello suponga una alteración en su funcionalidad básica como desfasador. Esta estructura desfasadora ha sido el elemento clave en el ensamblado de un filtro elimina banda sintonizable. En segundo lugar, se han utilizado diferentes configuraciones basadas en anillos de silicio con dimensiones micrométricas para el desarrollo e implementación de diferentes procesadores de señal, tales como filtros reconfigurables y sintonizables y retardadores multicanal. Concretamente, se ha introducido un nuevo concepto inspirado en la técnica conocida como SCT, cuyo beneficio redunda en un aumento considerable del ancho de banda útil de las señales de radiofrecuencia a procesar gracias a la naturaleza periódica de los resonadores en anillo y a la utilización de esquemas de modulación en banda lateral única. Por último, la demostración de diferentes procesadores operando tanto con señales de radiofrecuencia como con señales digitales se ha realizado mediante la utilización de discos compactos de pocas micras de radio, los cuales se han fabricado con tecnología híbrida gracias a la combinación de compuestos activos pertenecientes a los grupos III-V y de silicio, otorgándoles un alto rendimiento en términos de velocidad de sintonización. Finalmente, se ha realizado una comparativa en base a un conjunto de figuras de mérito con el propósito de discernir qué tecnología se adecua mejor a cada situación en particular.

Resum

Aquesta tesi doctoral perseguix l'objectiu de dissenyar i implementar nous dispositius òptics capaços de realitzar tasques de processat de senyals de radiofreqüència, més en concret a les bandes de microones i milimètriques, mitjançant efectes de llum lenta que ocorren a alguns soports físics amb propietats especials. Amb aquest propòsit en ment, s'han investigat estructures basades en guiaones de semiconductor, a més a més d'altres de tipus ressonant fabricades amb silici i amb compostos híbrids de materials actius pertanyents als grups III-V sobre silici. En concret, s'han proposat diferents circuits òptics amb la capacitat de desenvolupar tasques pròpies de desfasador i retardador veritable de banda ampla per a senyals de radiofreqüència. El funcionament d'aquests circuits s'ha caracteritzat fent servir modelatge teòric, el qual ha estat adequadament validat per resultats experimentals. En primer lloc, s'han dut a terme estudis relatius a la degradació produïda per soroll en estructures desfasadores formades per amplificadors òptics de semiconductor. A partir d'aquests resultats, s'ha proposat una nova estructura que ha revertit en un rendiment optimitzat en termes de soroll sense que això supose cap canvi en la seua funcionalitat bàsica. Addicionalment, aquesta estructura desfasadora ha estat l'element clau en l'emboetat d'un filtre elimina banda sintonitzable. En segon lloc, s'han utilitzat diferents configuracions basades en anells de silici amb dimensions micromètriques per al desenvolupament i implementació de processadors de senyal, com ara filtres reconfigurables i sintonitzables o retardadors multicanal. A més a més, s'ha introduït un nou concepte inspirat en la tècnica coneguda com a SCT. El benefici redunda en un augment considerable de l'ample de banda útil dels senyals en processament gràcies a la naturalesa periòdica dels ressonadors en anell i a la utilització de esquemes de modulació de banda lateral única. Per últim, la demostració de diferents processadors capaços d'operar tant amb senyals de radiofreqüència com amb senyals digitals s'ha realitzat mitjançant la utilització de discs compactes de poques micres de radi, els quals s'han fabricat emprant tecnología híbrida sorgida de la combinació de compostos actius pertanyents als grups III-V i de silici, atorgant-lis un alt rendiment en termes de velocitat de sintonització. Finalment, s'ha realitzat una comparativa en base a un conjunt de figures de mèrit amb el propòsit de discernir la tecnología que s'adequa millor a cada cas en particular.

List of Acronyms

AGC	Automatic gain control
ASE	Amplified spontaneous emission
ASPIC	Application specific photonic integrated circuit
BCB	Benzo cyclo butene
BPSK	Binary phase shift keying
CMOS	Complementary metal oxide semiconductor
CPO	Coherent population oscillations
CROW	Coupled resonator optical waveguide
DC	Direct current
DFB	Distributed feedback
DPSK	Differential phase shift keying
DSB	Double sideband
EDFA	Erbium doped fiber amplifier
EIT	Electromagnetically induced transparency
EMI	Electromagnetic interference
EOPM	Electro-optic phase modulator
ESA	Electrical spectrum analyser
FBG	Fiber Bragg grating
FCD	Free carrier dispersion
FIR	Finite impulse response
FoM	Figure of merit

FSR	Free spectral range
FT	Fourier transform
FWHM	Full width at half maximum
FWM	Four wave mixing
HBW	High bandwidth
HD	Harmonic distortion
ICP	Inductively coupled plasma
ICT	Information and communication technology
IHB	Inhomogeneous broadening
IM	Intensity modulation
IMD	Intermodulation distortion
KK	Kramers Kronig
LCoS	Liquid crystal on silicon
MDR	Micro-disk resonator
MEMS	Micro-electro-mechanical system
MRR	Micro-ring resonator
MQW	Multiple quantum well
MWP	Microwave photonics
MWPF	Microwave photonic filter
MZI	Mach-Zehnder interferometer
MZM	Mach-Zehnder modulator
NEMS	Nano-electro-mechanical system
NF	Noise figure
NEMS	Nano-electro-mechanical system
OEO	Opto-electronic oscillator
ONF	Optical notch filter
OOK	On-off-keying
OSSB	Optical single sideband
PAA	Phased array antenna

PD	Photo-detector
PhC	Photonic crystal
PS	Phase shift
PSD	Power spectral density
QD	Quantum dot
QW	Quantum well
RC	Resistor-capacitor
RF	Radio-frequency
RIN	Relative intensity noise
SBS	Stimulated Brillouin scattering
SCISSOR	Side-coupled integrated spaced sequence of resonators
SCT	Separate carrier tuning
SFDR	Spurious-free dynamic range
SFL	Slow and fast light
SLL	Side lobe level
SNR	Signal-to-noise ratio
SOA	Semiconductor optical amplifier
SOI	Silicon-on-insulator
SRS	Stimulated Raman scattering
SSMBE	Solid source molecular beam epitaxy
TTD	True time delay
VNA	Vectorial network analyser
VOA	Variable optical attenuator
WGM	Whispering gallery modes

Contents

List of Figures

Index of tables

Chapter 1
Introduction

1.1 Context

In the last decades, the telecommunication industry roadmap has continuously experienced deep changes in response to the more and more demanding market requirements in the context of new services and higher operating bit rates. Motivated by a dense radio-electric spectrum, these new wideband services and applications have been placed at higher frequencies, mainly at the microwave and millimeter wave spectral bands. Therefore, new technologies and devices capable of generating, controlling and processing microwave and millimeter signals have been intensively developed in the past years. However, electronic devices are becoming a bottleneck in data networks, drawback which can be nowadays overcome by exploiting the huge bandwidth provided by all-optical solutions. Together with the huge bandwidth, optical technologies bring a series of inherent advantages in terms of reconfigurability, tunability, low loss, electromagnetic immunity (EMI), low weight and absence of impedance-matching problems that cannot be overlooked. For these reasons, the actual state-of-the-art tends towards the implementation of all-optical solutions in the next generation data networks. As a consequence, the generation, processing and transport functionalities of radio-frequency (RF), microwave and millimeter-wave signals directly in the optical domain must be accomplished. This discipline, which acts as the link between the optical and electrical engineering, is known within the scientific community as *Microwave Photonics* (MWP) [1–3].

In this scenario, *Slow and Fast Light* (SFL) effects, which were originally conceived for buffering high-speed digital optical signals [4], now look set to play an important role in providing photonic-assisted microwave and millimeter signal processing tasks [5, 6]. SFL refers to the possibility of controlling the group velocity of an optical signal, which can be achieved by modifying the medium dispersion profile or by properly designing the guiding structure [7]. In MWP, SFL translates into a continuous tuning of the phase-shift or time delay of the RF signal modulating the optical carrier with low loss, negligible distortion and incomparably larger bandwidth than those provided by equivalent electronic devices [6]. These properties have led to

breakthrough progress in the implementation of more complex RF signal processors with unprecedented performance [5, 6]. In addition, several SFL technological platforms are suitable for the incorporation into an *application specific photonic integrated circuit* (ASPIC). In this way, additional value added in the context of miniaturization, thermal and mechanical stabilization, low cost, complexity and reduced power consumption becomes a reality.

1.2 Slow and Fast Light (SFL): Basics and technological platforms

SFL effects enable the control of the speed of light propagating through a particular dispersive material system. The mechanisms mediating SFL propagation rely on modifying the dispersion profile of the medium or on properly designing the guiding structure [8].

For the past two decades, the optical physics community has been fascinated by the SFL phenomena [7]. These names refer to the situations in which the group velocity of light, v_g, is very different from the speed of light in the vacuum c. For a wave-packet travelling in a medium or waveguide, SFL entails the modification of the v_g through the control of the group index n_g, since

$$v_g = \frac{c}{n_g} = \frac{c}{n + \omega \frac{dn}{d\omega}}, \tag{1.1}$$

where n and ω correspond to the refractive index and the angular frequency respectively. In particular, the n_g can be expressed as the sum of two contributions referring to the constant and the dispersive terms of the n_g. When the dispersion is normal, this means $dn/d\omega > 0$, then $v_g < c/n$ and slow-light propagation is achieved. In contrast, when $dn/d\omega < 0$, it is referred as anomalous dispersion resulting in fast-light propagation since $v_g > c/n$. Hence, SFL entails the engineering of media dispersion in combination with low distortion and low optical absorption [6].

The physical understanding of the SFL effects occurring in a certain media is provided by the Kramers-Kronig (KK) relations [9]. KK supports the theory linking the real, n, and imaginary, n', parts of the refractive index by means of the Hilbert transforms. In particular, any gain or loss resonance gives rise to a large and rapid variation of the n in the vicinity of the resonance. In such a way, this variation of the n at the end results in a n_g modification according to Eq. 1.1. This relations are illustrated in Fig. 1.1. Slow light occurs on either side of the resonance where n_g is large, while fast light takes place in the resonance itself where n_g is decreased. The narrower the resonance is, the larger the v_g change. For the purpose of modifying n_g, two main approaches can be followed depending on whether the changes are due to the material or the structural dispersion.

In the first type, modifications of the *material dispersion* are achieved by means of an artificial manipulation of the absorption or amplification in the medium. This is often accomplished by exploiting other optical effects and phenomena, such as electromagnetically induced transparency (EIT), coherent population oscillations (CPO) in semiconductor optical amplifiers (SOAs) or several nonlinear effects in optical fibers

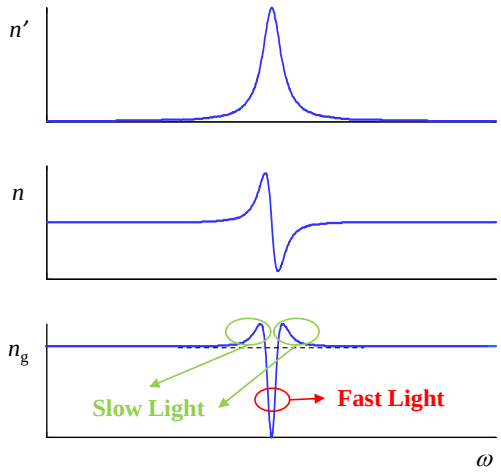

Figure 1.1: n', n and n_g provided by a narrow-band absorptive resonance in a two-level system according to the KK relations.

like stimulated Raman (SRS) and Brillouin (SBS) scattering. The main advantage relies on the tunability of the group velocity through a control parameter, for instance, the electrical current or the optical power. In contrast, the main limitation consists of a typical delay-bandwidth product slightly greater than the unity, resulting in delays of the order of the pulse-width [6]. One of the pioneering experiments showing material dispersion was based on the EIT phenomenon in atomic gasses [10]. In particular, the light was slowed down to the human scale of 17 m/s in ultracold atoms clouds enabling transparency in the material while allowing it to retain strong linear and nonlinear optical properties. However, the extreme environmental conditions (cryogenic temperatures) required to induce the effect, as well as the narrow bandwidth limited the applicability. To overcome these drawbacks, EIT was first demonstrated in 2003 by deploying a semiconductor quantum-dot device (QD-SOA) operating at room temperature [11]. Although it was presented as a very promising solution provided by its unique structural features enabling EIT maximization, the complexity of embedding the QDs in the proper positions in the semiconductor waveguide is still an issue [12]. Meanwhile, a second physical phenomenon enabling SFL propagation in semiconductor waveguides based on the so-called CPO was demonstrated [13]. CPO is less efficient in terms of delay compared with the EIT phenomenon, nevertheless better reliability is achieved since SOAs with standard properties can be readily used exhibiting good performance [14]. Although CPO results in a remarkable reduction of the group velocity, it seems still far from acceptable for real application systems since it operates at a very well-defined wavelength and the achievable time delay in this system is very limited to around 10% of the signal duration [15,16]. Consequently, the semiconductor waveguide enables group velocity control by means of both optical and electrical tuning mechanisms in a compact device. On the other hand, the ubiquitous role of optical fibers in modern data networks has motivated the development of SFL effects directly in this close-to-perfect transmission line [17]. In particular, the exploitation of nonlinear effects based on SBS [18] and SRS [19,20] have paved the way

towards the implementation of distributed optically controlled delay lines. Features such as the possibility of operation at room temperature and at telecommunication wavelengths, as well as unique spectral tailoring capability and high potential for large signal delay-bandwidths arise this technology as a very promising solution. However, the main drawback consists of the integration difficulty.

In the second type, the *structural dispersion* is modified by a proper design of the structural properties of the optical waveguides. This class of SFL devices include coupled cavities and photonic crystal (PhC) waveguides. Two are the key features which make these devices extremely attractive from the application point of view [6]. The first one is related to the fact that the energy velocity coincides with the group velocity, resulting in an enhancement of the nonlinear effects [21]. The second relies on the possibility of realizing these devices by using photonic integrated circuits, thus having the potential for small footprint, low consumption and large parallelization. Typically, the coupled cavities are implemented by cascading several ring-type resonators. There exists in two basic designs: coupled resonator optical waveguides (CROWs) and side-coupled integrated spaced sequence of resonators (SCISSORs) [22]. However, the principle of operation is the same and it relies on exploiting the dispersive behavior in the vicinity of the resonances mediated by the resonant-type nature of the cavities. SCISSOR-based structures reach longer delays, primarily because the inevitable spread of resonator parameters in fabricated CROW devices causes a localization and a significant reduction in performance [22]. Concerning the PhC waveguides, the group velocity is controlled by exploiting the dispersive nature of the spectral region in the vicinity of the photonic band-gap [23]. Slowing down group velocity by a factor of more than 100 over a wide-bandwidth can be accomplished [24]. Unlike slow light schemes mediated material dispersion, the PhC offers wavelength flexibility and it can be integrated on different materials, including those based on III-V enabling low loss or even amplification.

1.3 How can Microwave Photonics benefit from SFL effects

Nonlinear optical methods mediated SFL techniques have exercised unprecedented control over the propagation velocity of light pulses through different material systems [7, 8]. Soon after the demonstration of slow, fast and even stored light effects, attention was turned toward the development of useful applications, including controllable optical delay lines and optical buffers [4].

However, the potential of SFL is immense and opens the door to a host of new and exciting opportunities beyond delay lines and buffers [25]. Light travelling at a very low speed is anticipated to have a far-reaching impact on radar systems, radio-frequency signal processing and quantum information science. In fact, impressive advances within the MWP field has been accomplished in recent years, particularly in the implementation of tunable time-delay/phase-shift devices [6, 26].

In the previous section, SFL propagation of light pulses has been described. In particular, a pulse of light is a wave-packet that is composed of an infinite number of monochromatic component waves. When the pulse propagates through a material system, each monochromatic component wave travels at a different speed because

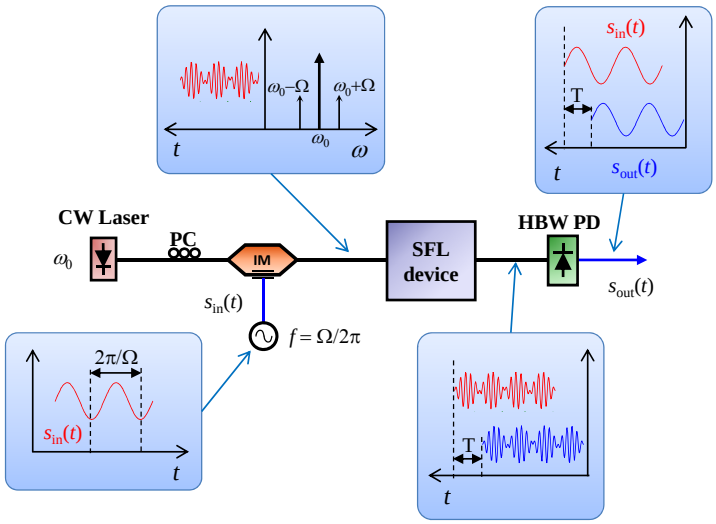

Figure 1.2: MWP link including a SFL device enabling RF signal processing.

of the frequency dependence of n, resulting in a time shift relative to the vacuum propagation. For short propagation distances, pulse distortion can be neglected and the motion of the pulse can be readily described by Eq. 1.1. In the context of MWP, the implications of SFL propagation can be simplified to the study of monochromatic signals without loss of generality. In Fig. 1.2, the basic architecture of a MWP link based on SFL effects is illustrated. A continuous-wave (CW) optical source is intensity modulated by a microwave signal oscillating at angular frequency Ω. The SFL device processes the modulated carrier by changing the group velocity of the light propagating through the medium. After photodetection, this tunable time delay or advance is translated into a phase delay or advance change of the monochromatic signal. In this context, the phase velocity v_p describes the speed at which the wavefronts move through the material and is given by $v_p = c/n$. Therefore, a n change results in phase velocity modification, which translates into a phase shift of the monochromatic signal as shown in Fig. 1.3(a). From the RF signal processing point of view, the implementation of broadband and tunable phase shifting and true time delaying lines are key points. On one hand, flat phase shifts over a broadband RF spectral range are highly desired. In addition, fully continuously tunable phase shifters (PS) spanning from 0 to 2π radians are particularly important within the context of MWP. On the other hand, the functionality of true-time delay (TTD) lines involves the implementation of linear phase feature with the frequency. In particular, the phase slope determines the imprinted time delay according to the relation $T = d\phi/d\Omega$. Therefore, in order to implement tunable time delay lines, the phase slope needs to be controllable. These concepts are illustrated in Fig. 1.3(b). A phase shift $\Delta\phi$ of a monochromatic signal with angular frequency Ω translates into a time delay ΔT following the relation $\Delta T = \Delta\phi/\Omega$.

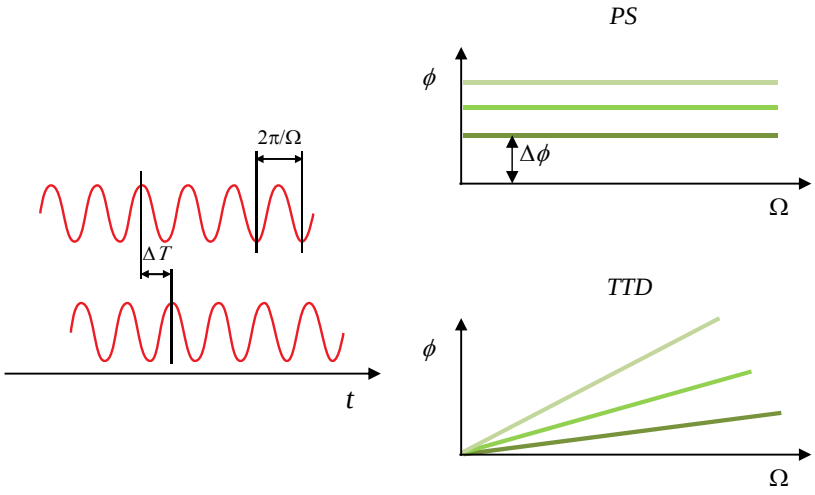

Figure 1.3: (a) Monochromatic wave and a delayed replica. (b) Concepts of tunable and broadband PS and TTD functionalities.

The refractive index in a certain medium is normally complex, as already mentioned. The imaginary part, n', is associated with the medium loss or gain, whereas the real part, n, is directly related to the propagation properties. In this context, tunable gain/loss resonances can be exploited for the implementation of both PS and TTD functionalities. For simplicity purposes, an optical single sideband (OSSB) modulation scheme is considered without loss of generality. Depending on the spectral location of both the optical carrier and the modulation sideband with respect to the resonance, PS or TTD functionalities are accomplished, as shown in Fig. 1.4. On one hand, when the optical carrier falls inside the resonance but stays outside the modulation sideband, phase shifting tasks can be developed. This fact is illustrated in Fig. 1.4(a). After beating at the receiver, the detected signal experiences a phase shift that is determined by the phase difference between the optical carrier and the subcarrier. By tuning the spectral position of the optical carrier within the resonance, the phase imprinted on it changes accordingly, resulting in a controllable phase shift of the RF signal. On the other hand, implementing a true time delay line requires both the carrier and sideband to be located in the linear region of the phase shift, this means, inside the resonance (see Fig. 1.4(b)). In such a way, carrier and subcarrier experience linear phase change with the frequency.

These key functionalities are used in the implementation of more complex photonic-assisted RF signal processors, such as tunable filters (MWPF) and optically-fed reconfigurable phased array antenna (PAA) systems.

In particular, finite impulse response (FIR) filters [27] relies on combining a finite set of delayed and weighted replicas or taps of the input signal, formally named taps or samples at the output. The most powerful and versatile approach for the implementation of MWPFs is that based on incoherent discrete signal processing, which is shown in Fig. 1.5. The input RF signal, $s_{in}(t)$, is conveyed by the optical

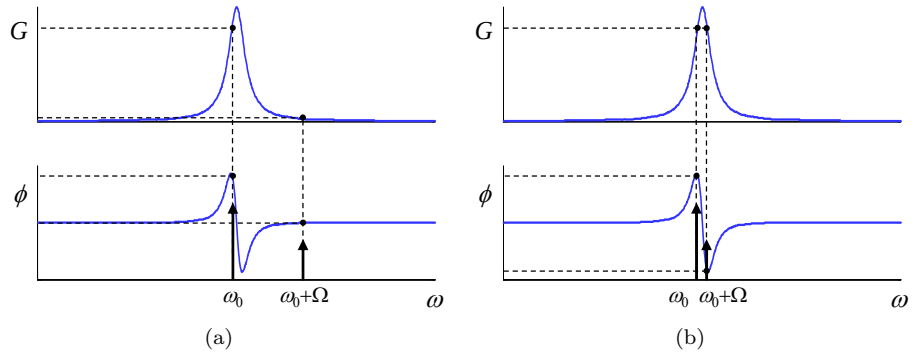

Figure 1.4: Implementation of tunable (a) phase shift and (b) true time delay functionalities in a resonant medium.

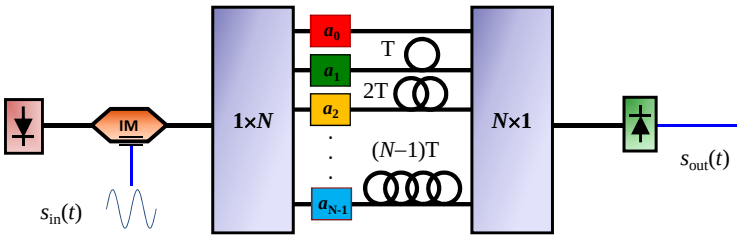

Figure 1.5: Schematic of a FIR MWP filter.

carrier and the composite signal is first split into N samples by using a $1 \times N$ optical coupler. Each sample is then independently weighted, phase-shifted and delayed. The time spacing between adjacent samples, T, is inversely proportional to the free spectral range (FSR) of the filter response. Then, all the samples are combined again prior the detection. This way at the receiver output the RF signal, $s_{out}(t)$, is composed by the interference of all the N weighted, delayed and phase-shifted samples. Consequently, the electrical transfer function can be expressed as

$$H(f) = \frac{s_{out}(f)}{s_{in}(f)} = \sum_{r=0}^{N-1} |a_r| e^{jr\theta} e^{j2\pi frT}, \tag{1.2}$$

where a_r denotes for the filter complex coefficients. Dynamic control of T is basically required for the development of reconfigurable MWPFs, provided by FSR tunability. Nevertheless, resonance tunability while keeping the FSR and spectral shape of the filter response unaltered can be readily accomplished by controlling the basic phase shift, θ. These filters are usually operated in incoherent regime, in which the coherence time of the optical source must be much shorter than T, in order to avoid environmental-related problems.

In the case of optically-fed PAA systems, the N weighted, phase-shifted and delayed samples are directly detected by N receivers prior feeding the N radiating

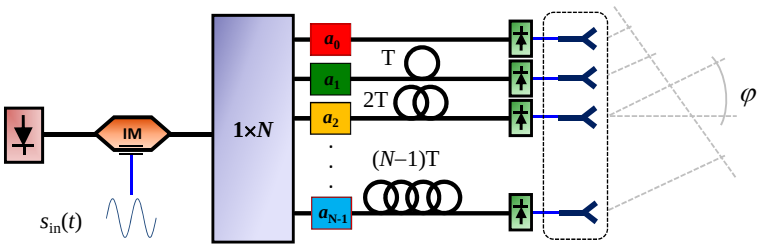

Figure 1.6: Schematic of an optically-fed PAA system.

elements, as illustrated in Fig. 1.6. The normalized angular far-field pattern of the radiated electric field, or antenna diagram $F(\varphi)$, is given by the Fourier transform of the output electric field [28],

$$F(\varphi) = \frac{1}{N}\sum_{r=0}^{N-1} a_r e^{-j2\pi r f\left(T-\frac{d}{c}\sin\varphi\right)}, \tag{1.3}$$

where φ is the far field angular coordinate and d is the spacing between adjacent radiating elements. The complex coefficients a_r are in this case properly adjusted for side-lobe reduction in the antenna far-field pattern. From Eq. 1.3, the direction φ_0 of maximum radiated energy can be adjusted by tuning the incremental time delay T according to

$$T = \frac{d}{c}\sin\varphi_0. \tag{1.4}$$

It is important to remark that the use of MWP PSs to perform the PAA system tunability inevitably induces beam squinting effects, where the main lobe of the radiation pattern slightly drifts away from the desired angle with changes in the operating frequency. This undesired effect limits the assemble of PAA supporting broadband services. In response, TTDs can perform tunability and, at the same time, compensate for this beam squint effect [28].

1.4 Objectives and structure

1.4.1 Objectives

This Ph.D. thesis is enshrined in the 7^{th} European Union Framework Programme (EU FP 7) through the GOSPEL (GOverning the SPEed of Light) project. In particular, the GOSPEL project aims at developing new, highly effective technologies for enabling slow and fast light propagation as a tunable feature in photonic devices. In fact, controlling the speed of light offers a solution to a necessary, and often missing, functionality in broadband information and communication technology (ICT) systems: a time delay/phase-shift line. The proposed research have addressed several SFL device

platforms, such as linear and nonlinear semiconductor PhC waveguides with position controlled embedded QDs, active semiconductor waveguides based on QDs, advanced engineered optical fibers and resonant-type devices based on silicon-on-insulator (SOI) and III-V materials. These technologies have been properly harnessed in microwave and millimeter wave applications. In particular, the implementation of TTD antenna feed systems for radars, complex MWPFs and high spectral purity opto-electronic oscillators (OEO) is of strategic importance and have focussed major efforts.

In this context, this Ph.D. thesis have pursued the accomplishment of several objectives. The main goal has focussed on the design and implementation of novel approaches with the aim of developing photonic-assisted RF signal processing tasks by exploiting SFL effects in different media. For this purpose, different technology platforms such as semiconductor waveguides, SOI and III-V compounds based resonant-type structures have been used. The performance of the approaches in the context of several figures of merit have been evaluated in order to identify the proper technology when implementing a certain functionality.

The achievement of this general goal involves the attainment of more specific goals, which are following described in detail:

1. To understand the physical processes governing SFL propagation on the different technology platforms dealt with this work and how to exploit SFL effects in the design and implementation of photonic-assisted phase shifting and true time delaying line functionalities in the microwave and millimetre spectral bands.

2. To propose novel SFL based approaches implemented by using the different technological platforms dealt with this thesis.

3. To describe the behavior of the proposed approaches in terms of delay/phase-shift as a function of the delay/phase-shift tunable mechanism via theoretical analysis. Results for the power penalty derived from the delay/phase-shift tunability must be also modelled. The theoretical modelling must be properly validated through experimental results.

4. To integrate the proposed SFL-based approaches as a key elements in the implementation of more complex signal processing tasks, such as, tunable and reconfigurable complex-valued multi-tap MWPFs, multi-channel TTD tunable lines operating at high aggregate bit rates or high-bandwidth phase modulators.

5. To evaluate the performance of the developed signal processors in the context of several figures of merit, such as noise degradation, loss, power consumption, size or nonlinear effects. A comparison attending to the metric results must be done in order to identify the use of the most proper technology depending on the final processing task to be developed.

To partially fulfill these objectives, a short-term stay of 3 months has been carried out at *imec* (Belgium). *imec* is a worldwide leading institution performing high-impact research in nano-electronics and nano-technology applied in areas such as healthcare, smart electronics, sustainable energy and safer communications.

1.4.2 Structure of the thesis

In order to pursue the objectives presented in the previous section, the content of this dissertation is structured in the following chapters, each one dealing with a distinct technology platform:

Chapter 2 focuses on the noise performance evaluation of SOA-based MWP phase shifting stages. The evaluation is accomplished through theoretical and experimental results. The theoretical results are obtained by using a novel frequency-based numerical model which has been developed. Besides, a customized MWP phase shifting stage is presented, which enhances the performance in terms of noise degradation while keeping unaltered the functionality as a phase shifter. Following, the numerical model is extended to encompass the noise performance of cascaded phase shifting stages, fact which is essential for obtaining fully tunable 2π phase-shifts. Finally, the experimental realization of a tunable MWPF enabled by cascaded SFL SOA-based phase shifting stages is demonstrated.

Chapter 3 addresses results concerning the implementation of photonic-assisted RF signal processors by exploiting SFL effects in SOI micro-ring resonators (MRRs). In particular, two different approaches implementing RF signal processing tasks, such as a multi-tap complex transversal filter and a multi-channel true time delaying line are demonstrated, which involve the use of SOI MRRs. In this context, the SOI MRRs design and fabrication processes are described in detail. A novel concept enabling bandwidth enlargement on certain MWP processors based on the so-called separate carrier tuning (SCT) technique is also introduced.

Chapter 4 deals with the implementation of photonic-assisted RF and data signal processors by exploiting SFL effects, but this time using III-V-on-Si micro-disk resonators (MDRs). Applications such as a MWP phase shifter, a complex-valued notch MWPF and a phase modulator are demonstrated when using III-V/SOI MDRs. A very comprehensive semi-analytical model for characterizing the III-V-on-Si MDR behavior from the MWP point of view is presented. The design, technology and fabrication of the above-mentioned MDR are detailed in-depth.

Chapter 5 summarizes the main conclusions derived from this thesis and list the most significant challenges and open research lines to be taken up in the near future. Moreover, a performance comparison of the MWPF developed in this work and others recently reported in the literature is presented.

Chapter 2

SFL effects in SOA waveguides

2.1 Introduction

Motivated by the difficulty to apply the pioneering experiments showing drastically light speed reduction in an ultracold atomic gas [10], the *semiconductor waveguide* was first proposed in 2003 as a very promising technological platform capable of inducing SFL effects at room temperatures [29]. The principle of operation consisted of the so-called EIT effect. EIT relies on of maintaining quantum mechanical coherence between a few discrete states that are coupled by the probe and an additional control signal, and therefore very susceptible to dephasing effects [12]. In this context, QD-based semiconductor materials were presented as excellent candidates due to their quantized energy levels, relatively low dephasing rates and possibility for monolithic integration [11]. However, the current fabrication technology of self-assembled QDs leads to a large degree of inhomogeneous broadening (IHB), mainly caused by size fluctuations of the QDs [12]. The broadening causes the probe and coupling laser fields to experience different dephasing depending on the individual QD size. As a result, the overall EIT features are smeared out.

Meanwhile, a second physical mechanism for light speed control based on material dispersion was also first demonstrated using semiconductor waveguides in 2005 [30], which is named as CPO. CPO may be viewed as a wave-mixing interaction in which the effective group velocity of a probe field is affected by a strong pump field. This fact results in a dispersion profile determined by the population lifetime rather than the dephasing time, as occurs with the EIT effect. This leads to significantly relaxed conditions under which light slow-down may be observed, because maintaining the coherence between the different levels is unnecessary and thus working in media having a continuum of states is feasible [11]. Therefore, semiconductor materials commonly employed for optoelectronic devices such as semiconductor lasers and SOAs represent ideal candidates for CPO-based light speed control. In particular, SFL propagation in SOAs have led to applications within optical communications [4, 8, 16, 29] and in recent years, more intensively within the MWP field [15, 31–33]. In particular,

impressive development in the implementation of tunable and broadband MWP phase shifters [34, 35] and true time delay lines [36, 37] has been carried out.

In this chapter, a noise performance characterization of a SFL cascaded SOA-based MWP fully tunable phase shifter already reported in the literature [35], is accomplished. This cascaded configuration is the most used solution for implementing continuously tunable 2π phase shifts based on semiconductor waveguides. Firstly, a comprehensive numerical model aiming at predicting the RIN spectral density at the phase shifter output of SOA-based MWP phase shifters will be presented. From the noise characteristics, a novel customized scheme based on band-pass instead of notch filtering will be proposed. Additionally, some recommendations for the purpose of enhancing the noise performance in such a structure will be detailed. Finally, the phase shifter will be used as a key element in a notch-type filtering scheme enabling the implementation of complex-valued coefficients. This fact results in tunable filtering responses.

In the context of this thesis, the exploitation of SFL propagation in integrated devices for signal processing have been carried out. However, the fabrication of the integrated version of the solution reported in [35] has not been possible on time. Therefore, all the results presented in this chapter have been obtained by using the bulk devices, that is, commercially available SOAs and tailored FBGs operated in transmission.

2.2 Basics of SOA-based SFL elements. Coherent population oscillations

CPO-based SFL effects in semiconductor waveguides rely on coherent oscillations of the total carrier density in the waveguide region that displays material gain or absorption. Considering the SOA as a two-level system, as illustrated in Fig. 2.1(a), when applying a signal that is intensity modulated in time, e.g. by the beating of two CW signals, a strong pump and a weaker probe, the rate of stimulated emission is also modulated in time at the frequency difference between these waves. Hence, this implies a modulation of the excited carrier density of the structure, and since the gain of the structure and the refractive index depend on this carrier density, these parameters are modulated as well. The gain and modulation index correspond to temporal gratings that scatter the strong pump signal to sidebands displaced from the pump carrier frequency by the modulation frequency. One component is scattered to the conjugate frequency and leads to the build-up of a so-called conjugate signal as is well known from wave mixing in nonlinear optics [38]. Another component is scattered to the original probe frequency and leads to a change of both the intensity and phase of the probe field, depending on the phase relationship between the original probe field and the scattered component (see Fig. 2.1(b)). This phenomenon is referred to as the Bogatov effect [39]. From the point of view of light speed control, the desired effect of the wave mixing is to achieve a large and controllable dispersion of the refractive index. It must be noted that CPO-induced dispersion can be controlled either through the SOA injection current or the input optical power.

Nevertheless, previous research [4, 16, 31] has confirmed that the use of CPO in standard SOAs have a limited time delay bandwidth product, which means small

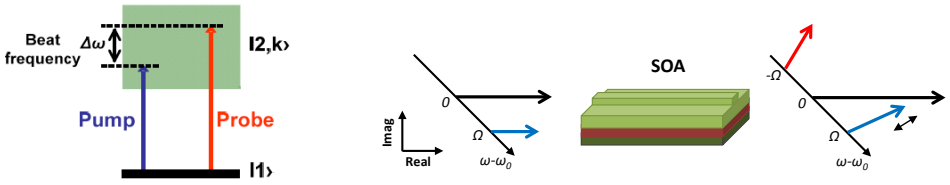

(a) (b)

Figure 2.1: (a) Level diagram for CPO effects. (b) Wave mixing between a pump and a probe signal in the SOA device, leading to the modification of the amplitude and phase of the probe and generation of a conjugate signal.

phase shifts. This is due to the detection of both sidebands. The refractive index dynamics cancels out and, hence, the phase change is governed solely by the gain dynamics. It has been suggested the use of a single sideband input signal in order to exploit the contribution from the refractive index, which is shown to give a significant contribution to the group index change [40]. However, the increase of the conjugate signal upon propagation effectively counteract this effect. Instead, refs. [34] and [41] have demonstrated that the effects of the refractive index mediated wave mixing can be exploited to increase the degree of the light speed control by the use of a novel scheme of optical filtering prior to detection. Figure 2.2(a) depicts the basic scheme. After propagation in the waveguide, the red-shifted sideband is blocked by an optical notch filter, which can be accomplished by a fiber Bragg grating. From now on, the element composed by the SOA followed by the filter will be referred to as phase shifting stage (PSS). Figure 2.2(b) presents the simulated results for the RF phase shifts when the input optical power is increased from -20 to 0 dBm. For the conventional case without optical filtering, $\sim 20^{\circ}$ phase advance at 15 GHz is achieved, as the green curve shows in the figure. For the case of blocking the blue-shifted sideband by optical filtering before the detection, as shown by the red curve, the RF phase shift is very close to the conventional case. Yet, when the red-shifted sideband is blocked, 150° phase delay can be continuously obtained, as the blue curve shows in the figure. Similar results can be obtained by varying the injection current instead of the input optical power to the SOA.

In order to achieve the 360° phase shift required for many applications in MWP, the possibility of cascading several PSSs has been investigated in [35]. It is important to mention that a further increase of the phase shift, e.g. by increasing the device length, is not possible due to saturation effects [35]. The basic configuration of three cascaded stages is illustrated in Fig. 2.3. After filtering the red sideband at the output of the first SOA, the spectrum differs from that at the input to the SOA and the serial addition of a second stage cannot, thus, immediately be expected to increase the phase shift [32]. Instead, the blocked sideband needs to be regenerated. This functionality can be readily implemented using regeration stages (RS) in-between individual PSSs. RSs can be readily implemented by exploiting the conjugate signal generation mediated by the four-wave-mixing (FWM) phenomenon in a SOA. In such a way, the absolute phase shift can be expected to scale with the number of stages [35].

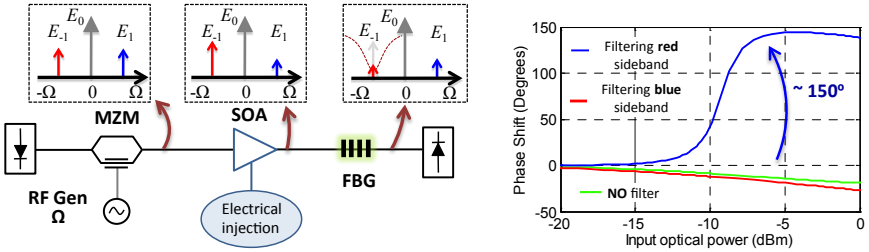

(a) (b)

Figure 2.2: (a) Basic scheme to enhance light slow-down by employing optical filtering to remove the red-shifted sideband prior to detection. (b) Calculated RF phase shifts at 15 GHz as a function of the SOA input optical power for a double sideband signal and a single sideband signal with blue and red sideband prior to detection.

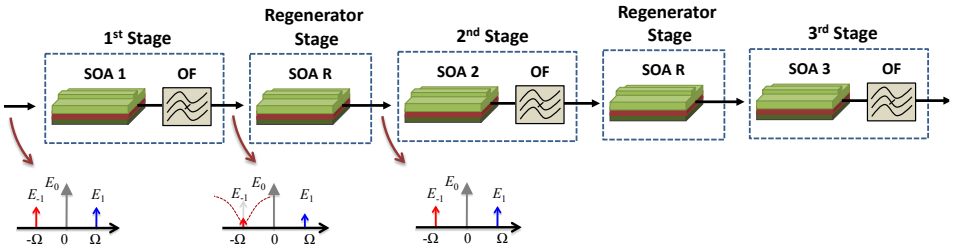

Figure 2.3: Schematic of the configuration based on three cascaded PSSs with the corresponding RSs.

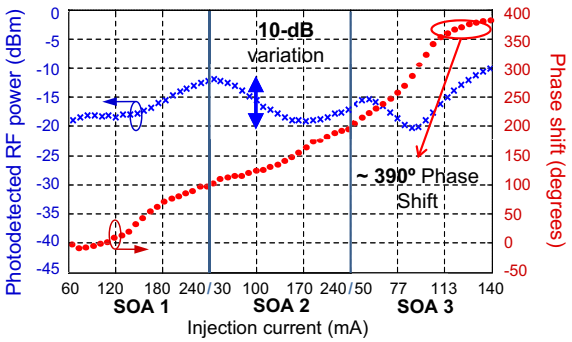

Figure 2.4: Measured RF phase shift and power variation at 15 GHz as a function of the injection currents of SOA 1, SOA 2 and SOA 3.

Figure 2.4 illustrates the measured photodetected RF power and phase shift for the output microwave signal as a function of the injection currents of SOA 1, SOA 2, and SOA 3 respectively. The injection currents for both RSs were fixed to 150 mA. Besides, the optical input power into the first PSS was adjusted to 10 dBm. The reference phase was taken for the injection currents of 60 mA, 30 mA and 50 mA, respectively. At the system output, $\sim 100^{\circ}$, $\sim 105^{\circ}$, and $\sim 190^{\circ}$ phase delays were obtained by progressively increasing the injection current of the three SOAs. In this case, a total 395° phase shift at 15 GHz was reached. The RF input and output signals were, respectively, generated and acquired by using a high-bandwidth vectorial network analyser (VNA). Since nonlinear phase shifts and large amplitude changes when sweeping the injection currents are unacceptable for most MWP applications, these characteristics together with the frequency response, can be optimized by accurately choosing different current combinations. Actually, by properly controlling all the three currents, less than 10 dB of RF power variation is possible. In contrast, it is well known that signal propagation in active semiconductor waveguides leads to the addition of amplified spontaneous emission (ASE) noise, thus deteriorating the signal-to-noise (SNR) ratio. In addition, it has been demonstrated in [42] that the filtering of the signal after the SOA, while increasing the phase shift, further degrades the signal-to-noise ratio, predominantly due to the decrease of the RF amplitude. Therefore, there exists a trade-off between the maximum achievable phase shift and SNR degradation.

This configuration allows for monolithically integration on InP technology platform by realizing the optical filters by, e.g. micro-ring structures, surface gratings or Bragg filters. An important issue in such a design consists of avoiding feedback effects from the integrated filters, which could lead to undesirable lasing effects. Figure 2.5 shows a schematic of a possible implementation of such a monolithically integrated MWP cascaded SOA based phase shifter.

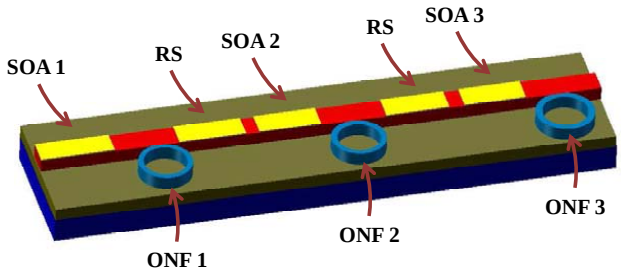

Figure 2.5: Sketch of a possible implementation of a monolithically integrated MWP phase shifter based on cascaded PSS [35].

2.3 Performance evaluation of MWP links based on SOAs. Figures of merit

After demonstrating the proper functionality of MWP phase shifters based on SOAs, its assembly in real systems lastly depends on the its performance. To this purpose,

a set of relevant figures of merit (FoM) must be evaluated from the microwave link point of view [43]. In particular, three metrics are of a great importance in MWP links involving active nature devices, as it is the case of SOA-based phase shifting elements: the RF net gain, the added noise and the signal distortion [44, 45].

The *RF net gain* (G) is defined as the ratio of the RF power delivered at the detector output, P_{out}, to the available RF power at the modulator input, P_{in}. Therefore, the gain can be expressed in linear units as:

$$G = \frac{P_{out}}{P_{in}}. \tag{2.1}$$

Net gain values greater than zero and featured by flat behavior as a function of the phase tuning mechanism, i.e. the optical power or the injection currents, are highly desired. However, in SOA-based phase shifting elements, average negative gain is usually obtained due to strong gain saturation. Besides, a gain variation with the phase tuning mechanism is unavoidable provided by the CPO phenomenon [45]

The *noise figure* (NF) is the most frequently used indicator for evaluating the degradation of the RF signal in MWP links caused by the different system noise sources. The NF is defined as the signal-to-noise at the input, SNR_{in}, divided by the signal-to-noise at the output, SNR_{out}.

$$NF = \frac{SNR_{in}}{SNR_{out}}. \tag{2.2}$$

Therefore, NF values as low as possible are desired. In SOA-based MWP phase shifters, several noise sources contribute to the total output noise level. In particular, the relative intensity noise (RIN) of the laser source, the phase noise of the RF synthesizer, the ASE generated by the SOAs and thermal and shot noises added by the detector [42, 46].

Due to the nonlinear behavior of phase shifting operating conditions of several devices comprising SOA-based phase shifting elements, distorted RF output signals are unfortunately obtained. In particular, the modulator, the RF synthesizer, the SOAs and the detector contribute to the degree of *distortion*. In this context, the spurious-free dynamic range (SFDR) represents the most commonly used metric. Two-tone SFDR is defined as the SNR_{out} when the integrated noise level within 1-Hz bandwidth equals to the power of a certain order intermodulation product. Depending on the reference signal, SFDR_2 and SFDR_3 refer to the 2^{nd} and 3^{rd} order distortion respectively [44]. Therefore, the assessment of SFDR_2 and SFDR_3 involves the characterization of the the harmonic (HD) and intermodulation distortion (IMD) respectively [47–49]. The nonlinear distortion of 3^{rd} order is found to be the most harmful due to the nearby spectral position with the fundamental frequencies, even though the 2^{nd} order distortion is lower [45].

2.4 Noise characterization

In the previous section, the most relevant FoM of SOA-based SFL elements have been detailed in-depth. Among them, the added noise is critical in this sort of structures,

specially in cascaded configurations. Hereafter, issues related to the NF assessment are dealt with. As derived from Eq. 2.2, the SNR at both the input and output must be obtained. For this purpose, the RF power and the integrated noise are required at both phase shifter input and output. In this section, both numerical and experimental investigations concerning the noise spectrum characterization are presented.

2.4.1 Context

The use of optical amplification is fundamentally accompanied by additive noise due to the spontaneous emission process. For semiconductor waveguides, the noise addition is well understood and widely documented.

On one hand, the added noise is additive when operating the SOA in the linear regime [50]. It is white and with a Gaussian distribution having a spectral density which is proportional to $G - 1$, G being the power gain. On the other hand, the noise treatment becomes more complex in the nonlinear regime. The saturating signal which propagates along the amplifier causes an increase in the inversion factor, thereby increasing the spectral density of the broadband noise. More important, the saturating signal interacts with the broad band noise in a four-wave-mixing-like (FWM) process, which results in a spectral modification of the spectral density [51] and also affects the statistical distribution [52].

In SOAs acting as slow light elements, the situation is even more complex. The SOA exploits FWM and is naturally operating in the nonlinear regime. However, reasonably large phase shifts are only achievable when part of the output spectrum is removed by filtering prior to detection [41]; for sinusoidal microwave signals, this means filtering out the red shifted modulation sideband. Removing part of the signal spectrum results in a vast reduction of the SNR of the delayed microwave signal [42] and hence affects the performance of MWP links which incorporate such slow light elements.

In this context, a new model which accounts for the output filtering must be accurately developed and accurately corroborated by measurements in order to quantify the noise accompanying a slow light SOA-based MWP phase shifter.

2.4.2 Modelling

A comprehensive numerical model for the purpose of calculating the electrical relative-intensity-noise (RIN) spectral density at the output of SOA-based MWP phase shifters is presented. In absence of modulation, a semi-classical description already published in the literature can be used to evaluate the noise properties at the SOA output [53]. In particular, the model considers that the noise effect at the SOA output can be treated as a small perturbation, which is superimposed on the output average optical power. Therefore, the total optical power at the SOA output can be expressed as

$$P\left(z=L,t\right)=\overline{P}\left(z=L\right)+\delta P\left(z=L,t\right), \tag{2.3}$$

where $\overline{P}$ and δP denote the average output optical power and the fluctuating power due to noise, respectively. z and t are the longitudinal and temporal coordinates respectively, and L is the active cavity length.

Building on this, the RIN at the SOA output can be defined as

$$RIN\left(\omega\right)=\frac{PSD\left\{\delta P\right\}}{\overline{P}^{2}}=\frac{FT\left\{R_{\delta P,\delta P}\right\}}{\overline{P}^{2}}, \tag{2.4}$$

with ω, PSD, FT and R being the optical angular frequency, the power spectral density, the Fourier transform and the cross correlation function, respectively. Eq. 2.4 can be defined in terms of electrical field amplitude by taking into account that $\delta P=\delta\rho^{2}$ and $\overline{P}=\rho^{2}$, being $\delta\rho$ and ρ the amplitude for both the fluctuating and the average terms respectively. Therefore, the Fourier transform of the fluctuating term autocorrelation is

$$FT\left\{R_{\delta\rho^{2},\delta\rho^{2}}\right\}=\int_{\tau=-\infty}^{\tau=+\infty}\left\langle\delta\rho^{2}\left(t\right)\delta\rho^{2}\left(t+\tau\right)\right\rangle e^{-j\omega\tau}d\tau. \tag{2.5}$$

Since $\rho\gg\delta\rho$, the approximation $\delta\rho^{2}\simeq2\rho\delta\rho$ can be readily used. Consequently, Eq. 2.5 can be rewritten as

$$\begin{aligned}FT\left\{R_{\delta\rho^{2},\delta\rho^{2}}\right\}&=\int_{\tau=-\infty}^{\tau=+\infty}\left\langle2\rho\left(t\right)\delta\rho\left(t\right)\cdot2\rho\left(t+\tau\right)\delta\rho\left(t+\tau\right)\right\rangle e^{-j\omega\tau}d\tau=\\4\rho^{2}&\int_{\tau=-\infty}^{\tau=+\infty}\left\langle\delta\rho\left(t\right)\delta\rho\left(t+\tau\right)\right\rangle e^{-j\omega\tau}d\tau.\end{aligned} \tag{2.6}$$

Hence, the double-sided RIN spectrum is given in terms of the electrical field amplitude by

$$RIN\left(\omega\right)=\frac{4\cdot FT\left\{R_{\delta\rho,\delta\rho}\right\}}{\rho^{2}}. \tag{2.7}$$

Likewise [53], Eq. 2.7 can be properly developed and expressed as the sum of four contributions as

$$RIN\left(\omega\right)=R_{0}\left(\omega\right)+R_{sp}\left(\omega\right)+R_{g}\left(\omega\right)+R_{g,sp}\left(\omega\right). \tag{2.8}$$

The four terms appearing on the right-hand side of Eq. 2.8 describe the noise contributions of the injected signal (coming from the laser source), the spontaneous emission, the carrier noise and the carrier-spontaneous beat-note, respectively. These four terms are defined in terms of the semiconductor waveguide features as

$$R_{0}\left(\omega\right)=\left|H\left(0\right)\right|^{2}RIN\left(\omega,z=0\right), \tag{2.9}$$

$$R_{sp}\left(\omega\right)=\frac{\hbar\omega_{0}}{P_{sat}}\int_{z=0}^{z=L}\left|H\left(z\right)\right|^{2}\frac{2n_{sp}g}{\rho^{2}}dz, \tag{2.10}$$

$$R_g(\omega) = \frac{\hbar\omega_0}{P_{sat}} \int_{z=0}^{z=L} |H(z)|^2 \frac{\xi g_0 + g + aN_t(1+\xi) + g\rho^2(2n_{sp}-1)}{(1+\rho^2)^2 + (\omega\tau)^2} dz, \tag{2.11}$$

$$R_{g,sp}(\omega) = -2\frac{\hbar\omega_0}{P_{sat}} \int_{z=0}^{z=L} |H(z)|^2 \frac{2\left(1+\rho^2\right) n_{sp} g}{(1+\rho^2)^2 + (\omega\tau)^2} dz. \tag{2.12}$$

The parameters $\hbar$, ω_0, P_{sat}, g, a, N_t and τ are the normalized Plank's constant, the center angular frequency, the saturation power, the average power gain, the differential gain coefficient, the carrier density at transparency and the carrier lifetime respectively. ξ is a parameter describing the noise of the current source feeding the SOA. By assuming that the current source exhibits shot noise behavior then ξ=1. On the other hand, the inversion parameter, n_{sp}, and the small-signal gain, g_0, are z-dependent and are defined as

$$n_{sp} = \frac{g + aN_t}{g}, \tag{2.13}$$

$$g_0 = a(N - N_t). \tag{2.14}$$

The term $H(z)$ refers to the complex SOA transfer function. By considering that the ratio between the internal loss and the small signal gain coefficients $\gamma/g_0 \ll 1$, then the complex transfer function is simplified as

$$H(z) = \frac{1 + \rho^2(z) + j\omega\tau}{1 + \rho^2(L) + j\omega\tau}. \tag{2.15}$$

As already mentioned, the total microwave phase shift at the SOA output can be enhanced by filtering out the lower frequency modulation sideband prior to photodetection. Therefore, this filtering process must be carefully taken into account when calculating the output noise spectrum.

By considering an optical filter featured by a frequency transfer function $Q(\omega)$, at its output the total RIN spectral density becomes

$$RIN^f(\omega) = RIN(\omega)\,|Q(\omega)|^2, \tag{2.16}$$

where the index f indicates *filtered* and $RIN(\omega)$ is that calculated from Eq. 2.8. It is important to remark that Eq. 2.16 can support all kinds of linear filtering schemes by properly setting the corresponding transfer function $Q(\omega)$. In particular, $|Q(\omega)|^2 = 1$ when no filtering is performed.

At this point, the RIN spectral density at the output of a single PSS can be properly obtained by using Eq. 2.16. However, in order to obtain fully tunability, the cascade of PSSs is required. Moreover, RSs in-between individual PSSs elements becomes necessary in order to restore the modulation sideband suppressed

by previous filtering. As already mentioned, RSs can be conveniently implemented by stand-alone SOAs exploiting FWM for sideband regeneration purposes. Since the regeneration SOAs also generate noise, these elements must be accurately included in the modelling. Provided by the modular nature of the theoretical description, results concerning cascaded structures can be easily derived by considering that the $RIN^f(\omega)$ corresponds to the input $RIN(\omega, z=0)$ in Eq. 2.9 in the next stage and so on.

At the output of the last PSS, light resulting from the combination of signal and noise is collected. The photodetected RIN power as a function of the electrical frequency is defined by

$$\sigma_{RIN}^2(\Omega) = (\Re P_{ph})^2 r_I^2(\Omega), \tag{2.17}$$

with $\Re$ and P_{ph} being the detector responsivity and the input optical power to the detector, respectively. Because of previous filtering, $r_I^2(\Omega)$ is characterized by an asymmetric spectrum. It must be noticed that r_I is a measure of the noise level of the incident optical signal, directly related to the inverse of the SNR at the input of the detector.

$$r_I^2(\Omega) = \int_{\omega_0-\Omega-\frac{\Delta}{2}}^{\omega_0-\Omega+\frac{\Delta}{2}} RIN^f(\omega)\, d\omega + \int_{\omega_0+\Omega-\frac{\Delta}{2}}^{\omega_0+\Omega+\frac{\Delta}{2}} RIN^f(\omega)\, d\omega, \tag{2.18}$$

where Ω accounts for the electrical angular frequency, which spans from DC to the -3 dB bandwidth of the detector. On the other hand, $\Delta \to 0$ is the resolution bandwidth. Besides the RIN noise, the detector adds both thermal and shot noises. Hence, the total noise power at the SOA-based MWP phase shifter output, σ_t^2, is given by the combination of all the three noise sources as

$$\sigma_t^2 = \sigma_{RIN}^2 + \sigma_{thermal}^2 + \sigma_{shot}^2. \tag{2.19}$$

Finally, the output SNR is calculated as

$$SNR_{out} = \frac{C_{out}(\Omega_0)}{\int_{\Omega_0-\frac{BW}{2}}^{\Omega_0+\frac{BW}{2}} \sigma_t^2(\Omega)\, d\Omega}, \tag{2.20}$$

being C_{out}, σ_t^2, BW and Ω_0 the electrical output peak power, the total power density expressed in terms of 1/Hz, the noise bandwidth (usually determined by the channel information bandwidth) and the RF tone angular frequency, respectively. Therefore, the SNR_{out} is application-dependent. The parameter C_{out} can be properly calculated by using numerical models already published [34, 41].

Other numerical models have been reported so far in the literature in order to characterize the noise properties of SFL SOA-based MWP links [46, 54]. However, the presented model performs the calculations in the frequency domain instead of the time domain. This fact is found to provide faster computation times, which is specially

important when studying cascaded PSSs structures. Moreover, problems related to coherent sampling are also avoided. Furthermore, calculations considering several PSSs connected in cascade can be easily accomplished owing to the high scalability mediated by the modular nature of the model.

2.4.3 Numerical and experimental results. The role of optical filtering

In this section, numerical calculations of the RIN power spectral density at the output of SOA-based MWP phase shifters have been realized. The numerical results have been properly corroborated by measurements, showing good agreement. Firstly, a phase shifter comprising a single PSS has been considered. In Fig. 2.6, the basic set-up showing the configurations which have been investigated is sketched. The goal of the study is to discern the filtering scenario which leads to optimum noise performance of the phase shifting microwave link.

The set-up basically consists of a distributed feedback (DFB) laser, which can (D) or cannot (S) be modulated by means of a Mach-Zehnder modulator (MZM) in order to determine the system performance under static and dynamic behaviour respectively. The DFB laser generates an output RIN level of -160 dB/Hz. A variable optical attenuator (VOA) at the Erbium doped fiber amplifier (EDFA) input was used to adjust the proper optical power at the SOA input. Both the input and the output of the EDFA and the SOA were appropriately isolated. At the SOA output, three kinds of optical filtering schemes were employed: (a) no filtering, (b) notch filtering, and (c), band-pass filtering. In order to avoid any effect of the photodetector (PD) on the noise measurements due to thermal and shot noises, a variable attenuator was inserted to maintain a fixed power level at the PD input. Finally, the electrical spectrum was measured using an electrical spectrum analyser (ESA).

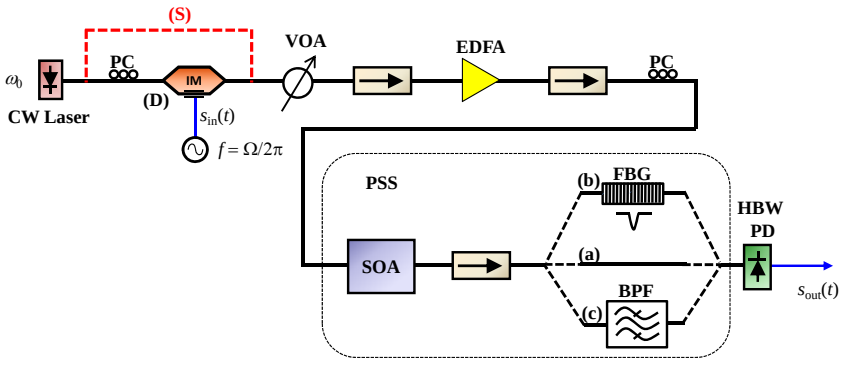

Figure 2.6: Experimental setup.

The optical notch filter (ONF) was implemented by means of a fiber Bragg grating (FBG) operating in transmission, whose normalized amplitude and phase transfer functions are shown in Fig. 2.7(a). The grating provides attenuation greater than 32 dB at the frequency where the notch is centered and has a -3 dB bandwidth of approximately 9 GHz. Besides, the FBG is featured by dispersive behavior in the

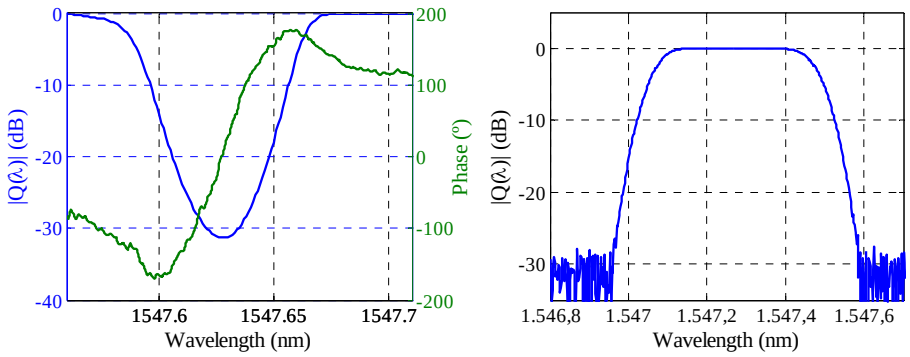

(a) (b)

Figure 2.7: (a) Measured normalized amplitude and phase transfer function of the FBG. (b) Measured normalized amplitude transfer function of the BPF.

vicinity of the both edges of the amplitude transfer function, since non-linear phase shift characteristic is obtained. Figure 2.7(b) shows the normalized amplitude transfer function of the band-pass filter (BPF). The filter is characterized by zero dispersion, maximum attenuation up to 30 dB, and a -3 dB bandwidth around 53 GHz.

2.4.3.1 Static behavior

Firstly, numerical and experimental results for the static characteristics of the SFL SOA-based MWP phase shifter are presented; i.e. for the case without an applied microwave signal (see Fig. 2.6, configuration marked as (S)). The system parameters have been set in order to induce a phase shift of approximately 150° on a RF tone placed at 15 GHz. The parameters have been chosen in accordance with previous experiments [34, 41]. In particular, the input optical power at the PSS input was adjusted to 8 dBm and the injection current into the SOA was swept from 150 to 350 mA to reach the above-mentioned phase shift. The worst scenario in terms of noise at the output of the phase shifting element occurs when the SOA displays the maximum gain, caused by the maximum injection current. Therefore, all the measurements and calculations have been performed by using a current of 350 mA, for the purpose of obtaining the noise ceiling. Other relevant system parameters used in the numerical calculations can be found in Tab. 2.1.

The calculated RIN spectra at the SOA output when injecting 350 mA are shown in Fig. 2.8. The noise spectra for all the 4 contributions accounting for the total output noise, according to the numerical model derived in the previous section, are displayed. The dominant noise contribution is that of spontaneous emission, R_{sp}, which is often referred to as the signal-spontaneous beat noise. At high frequencies, this is $\omega\tau \gg 1$, this contribution has a constant value which is consistent with the wideband nature of the spontaneous emission process. However, a dip indicating significant narrowband noise suppression occurs at low frequencies. This effect results from gain saturation, whose effect is limited to frequencies in which the gain responds to intensity fluctuations. The dip bandwidth increases with both the input optical

Symbol	Definition	Value
L	Active region length	1 mm
A_c	Active cross section	0.25 μm^2
α	Linewidth enhancement factor	6
Γ	Confinement factor	0.23
γ	Unsaturable loss	4000 m^{-1}
τ	Carrier lifetime	210 ps
a	Differential gain	$1.1{\cdot}10^{-20}$ m^2
N_t	Carrier density at transparency	$1{\cdot}10^{-24}$ m^{-3}
P_{sat}	Saturation output power	5 dBm
ξ	Current source noise	1
$\Re$	Detector responsivity	0.5

Table 2.1: Main parameters used for numerical calculations.

power and the injection current, yielding to faster recombination process. The terms R_g and $R_{g,sp}$, which involve the carrier noise, are relatively small and their contribution are also limited to frequencies at which carriers can exhibit fluctuations [53].

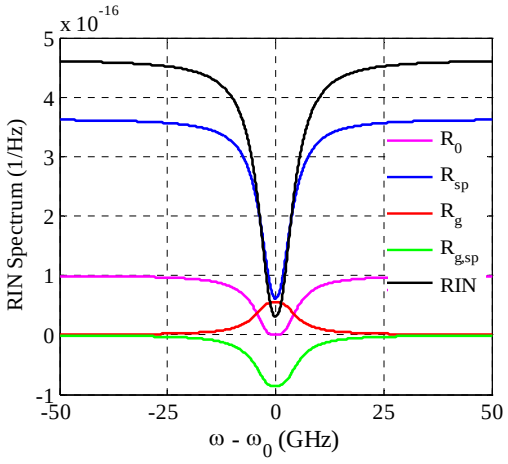

Figure 2.8: RIN spectrum at the SOA output and its four components.

Figure 2.9 displays the RIN spectra after filtering and prior to detection. The measured filter transfer functions shown in Fig. 2.7 have been respectively used for the calculations. On one hand, the minimum of the FBG response has been adjusted to be detuned by 15 GHz from the laser emission wavelength towards lower frequencies. In this way, the red-shifted sideband has been suppressed by more than 30 dB. The RIN spectrum is thus tailored by the FBG spectral shape. Out of the grating rejection band, the RIN level is also lowered because of the excess insertion loss, which is around 4.5 dB. On the other hand, both the optical carrier and the blue-shifted modulation sideband have been placed within the bandpass resonance of the BPF, while the red-shifted sideband experiences an attenuation greater than 30 dB. In this case, all the

RIN spectrum is filtered out except that part fitting the filter resonance. The RIN level at the BPF is also lowered due to the device insertion loss. For the case in which no filter has been used, the RIN spectrum prior detection corresponds to that shown in Fig. 2.8. It is important to remark that large phase shift is not reached without filtering the red-shifted sideband before the detection [34, 41].

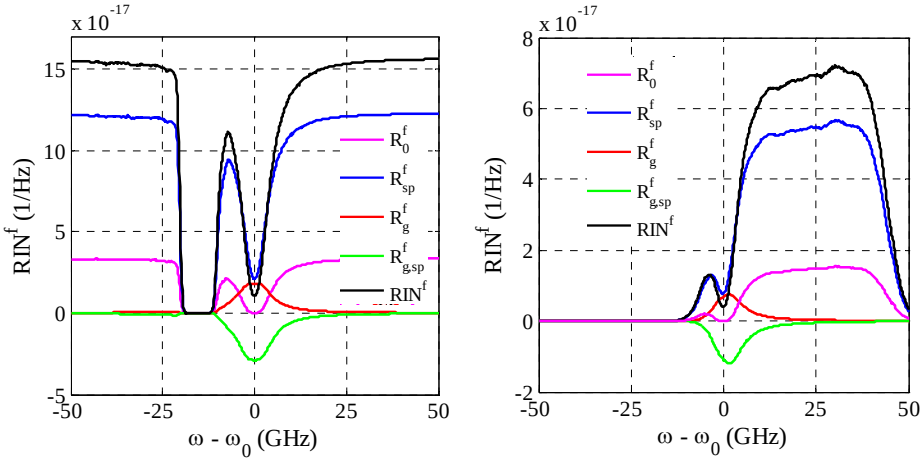

Figure 2.9: Calculated RIN^f spectrum and its four components after filtering by means of (a) an FBG and (b) a BPF.

Figure 2.10 shows the RIN power spectral density at the output of the phase shifting element when considering the three different filtering scenarios. The numerical results are validated by measurements, which are also depicted. For avoiding the dependence of the thermal and shot noises with the input power into the detector, a VOA is used to fix the input power at 0 dBm in all cases (see Fig. 2.3).

Considering the case where no filtering is performed, one observes that at high frequencies the noise level is nearly flat. However, at low frequencies, a dip in power appears and the spectrum displays a spectral hole, showing the typical high-pass noise filtering behavior of the SOA [53]. The numerical and experimental results are seen to agree very well.

Next, the influence of an ONF implemented by means of a FBG is considered. The spectral detuning between the optical carrier and the notch position of the FBG is adjusted to 15 GHz, as clearly seen in the spectrum. A RIN enhancement is observed around 10 and 20 GHz. This effect originates from frequency-to-amplitude modulation (FM-AM) noise conversion mediated by the dispersive characteristic of the FBG [55, 56]. As it has been already demonstrated, the dispersive nature of the output filter plays a crucial role to accurately model the phase feature of SOA-based MWP phase shifters [57]. Different noise contributions dominate in different frequency ranges. In particular, for frequencies lower than 5 GHz the ASE noise dominates, whereas at larger frequencies, the noise contribution originating from the FM-AM-noise conversion becomes the most significant. These frequency ranges obviously

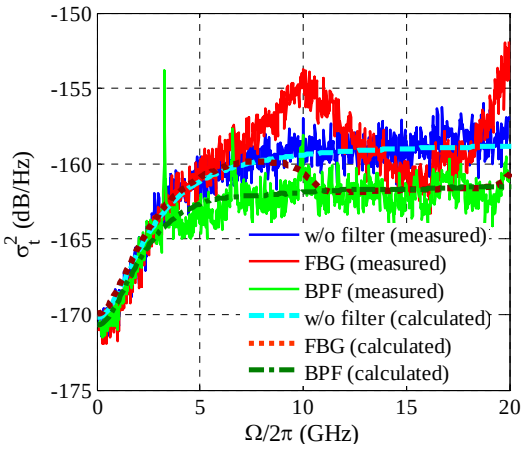

Figure 2.10: Measured and calculated RIN spectral density for the different filtering scenarios.

depends on the spectral detuning between the optical carrier and the FBG notch. There is a disagreement between calculated and experimental data, because the FM-AM-noise conversion phenomenon caused by the FBG is not included in the numerical model. The dispersion due to the FBG is zero at the notch central frequency, so the numerical model yields a reliable result at 15 GHz in this case.

Regarding the case in which the BPF is used, the RIN level is lowered because of noise filtering. When no filter or the FBG have been deployed, the noise spectrum has been integrated over the PD bandwidth (around 50 GHz). Therefore, the equivalent optical integration bandwidth spans along 100 GHz around the center angular frequency, ω_0. However, if the BPF is inserted prior to the detector, the equivalent bandwidth is limited to that imposed by the filter, which is approximately 53 GHz, since out-of-band negligible signal is obtained. That is the reason why, in this case, the RIN level decreases close to 3 dB compared to the no filter case. As a consequence, the RIN level is at last imposed by the frequency of the RF tone, since a filter as narrow as that frequency could be used. Numerical calculations are in perfect agreement with the measures, since the BPF features a non-dispersive behavior.

In order to get a deeper insight into the implications of the FBG dispersion on the RIN performance, studies have been carried out by varying the relative position between the optical carrier and the notch spectral position. Results are shown in Fig. 2.11. In particular, the efficiency of the FM-AM-noise conversion is frequency-dependent according to the phase transfer feature of the dispersive element. Specifically, the maximum conversion efficiency, and thereby the largest RIN enhancement, occurs when the most dispersive spectral region of the FBG characteristic coincides with the carrier frequency. A peak can also be observed at the frequency of 3.5 GHz approximately, which corresponds to the relaxation oscillation frequency of the DFB laser source. It also must be noticed that the larger the frequency detuning Δf, the lower the RIN level at the frequency where the notch is centered, because the conversion efficiency caused by the dispersive feature becomes lower.

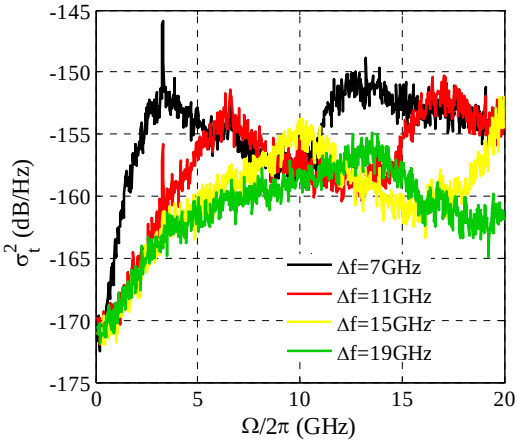

Figure 2.11: Measured RIN spectra with different degrees of FM-AM-noise conversion according to the spectral spacing (Δf) between the optical carrier and the notch position.

2.4.3.2 Dynamic behavior

In this section, the dynamic operating regime, i.e. the microwave signal is accounted (see Fig. 2.6, configuration marked as (D)), is considered.

There is a trade-off between the SNR_{out} and distortion when choosing the optical modulation depth [58], q, in SOA-based MWP phase shifters, as derived from [48]. Small-signal modulation, with q typically below 0.5%, is employed to alleviate the distortion and to yield good enough output SNR.

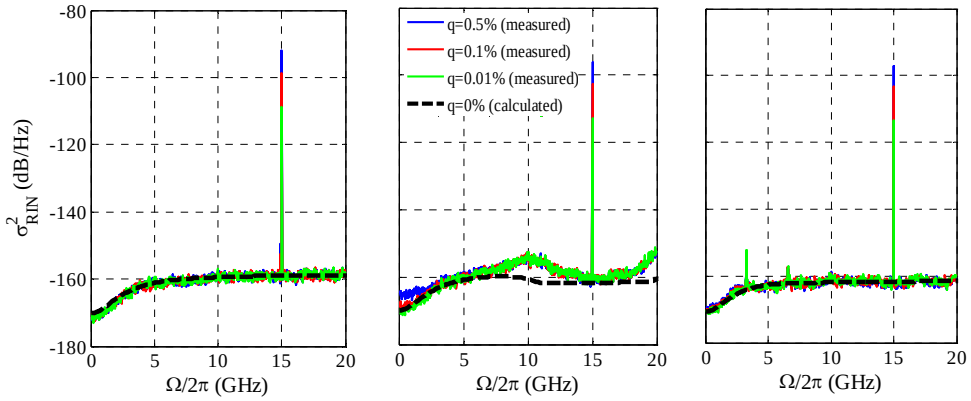

Figure 2.12: RIN spectral density as a function of the q when: (a) no optical filter is considered, (b) using a FBG and (c) using a BPF.

Figure 2.12 shows the numerical and measured RIN spectral density as a function of the filtering scheme and the q. It must be pointed out that whatever the q the noise level around 15 GHz stays roughly constant. This observation justifies the use of a static numerical model to predict the RIN when considering the microwave tone. Perfect agreement between experimental and calculated results is obtained in the scenario without optical filter, as shown in Fig. 2.12(a). On the other hand, when the FBG is used for filtering, numerical and measured results do not agree because of the FM-AM-noise conversion. However, numerical data is roughly consistent with experimental results at 15 GHz because almost zero dispersion is induced at the notch frequency (see Fig. 2.12(b)). The degree of saturation of the SOA has a major impact on the RIN spectrum, in particular at low frequencies, where a RIN enhancement can be seen as a function of q. The dip in power depends on the optical power and the q, because it results from interactions of both the optical carrier and the modulation sidebands with the noise. Consequently, the larger the q, the larger the RIN enhancement. This fact justifies the discrepancies at low frequencies between experimental and numerical results, due to the static nature of the model. Finally, when considering the BPF-based scheme (Fig. 2.12(c)), the agreement between calculated and measured data is very good as a function of both the frequency and the q because of the non-dispersive behavior.

Finally, the SNR has been obtained as a function of q in order to evaluate the noise properties of the MWP link. The SNR has been evaluated for the three different filtering schemes to discern which yields the better noise performance. To grant the results independence to the system bandwidth, the SNR has been obtained in terms of dB/Hz.

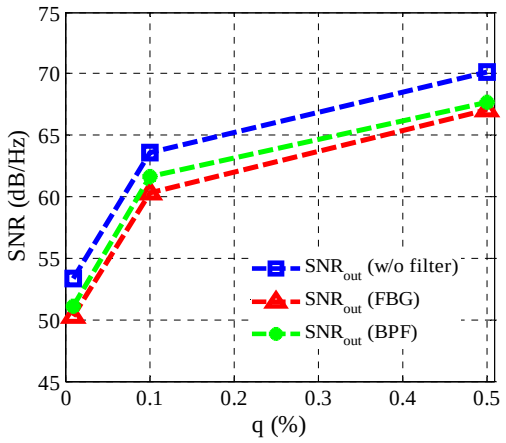

Figure 2.13: SNR_{out} as a function of q and the optical filtering scenario.

Figure 2.13 displays the output SNR of the phase shifting element. It must be pointed out that the larger q, the higher the SNR. The largest SNR_{out} is obtained when no filter is inserted prior to photodetection. In this case, both modulation sidebands are photodetected, giving as a result the maximum RF power. However, the induced phase shift on the microwave signal is lower by an order of magnitude when optical filtering is not applied [34]. When using optical filtering before the photode-

tection, the red-shifted modulation sideband is partially suppressed. Although the RIN is also lowered, the sideband is attenuated to a larger extent and the SNR_{out} is thus diminished. In case of the BPF, a larger amount of noise is rejected compared to the case in which FBG filtering is deployed. Therefore, the SNR performance is improved.

2.4.4 Noise in cascaded configurations

The cascade of PSSs stands for a suitable solution for enhancing the total phase shift of the microwave link. By using a proper configuration based on three PSSs, continuous tunable phase shift of 360° can be achieved [35]. The use of RSs in-between individual PSS elements is necessary in order to restore the modulation sideband suppressed by previous filtering. RSs can conveniently be implemented by stand-alone SOAs, which exploit FWM for sideband regeneration [35]. In Sec. 2.2, a configuration performing controllable 390° phase shift on 15 GHz RF signal has been demonstrated (see Fig. 2.4). For this purpose, the injection currents were progressively swept from 60 mA to 240 mA in the first PSS, from 30 mA to 240 mA in the second PSSs and from 50 mA to 140 mA in the third PSS, while keeping fixed the current injected into the RSs to 150 mA. Moreover, the optical power input to the first PSS was set to be 10 dBm. The optical filters were implemented by means of three narrowband FBGs. However, very similar results could be obtained by using three BPFs. In this section, the evolution of the RIN spectrum at the output of each PSS and RS is accurately determined by means of numerical calculations. Simulations have been carried out by assuming identical physical parameters for all the five SOAs. All the parameters used for numerical calculations have been those already shown in Tab. 2.1. Identical transfer functions for all the FBGs and BPFs (see Fig. 2.7) have been considered as well. Likewise the previous section, the ceiling noise level has been obtained. Therefore, the maxima current levels have been considered, this means, 240 mA for the first and second PSSs and 140 mA for third one.

Figure 2.14 shows the RIN spectra at each SOA and optical filter output when deploying the two different filtering configurations based on FBGs and BPFs respectively. The noise performance deterioration is noticeable when serially adding PSSs. Whatever the optical filtering scheme, the impact of connecting the third PSS is not as important as the fact of adding the second one. This is attributed to the larger gain saturation affecting the SOA located in the third PSS compared to that belonging to the previous PSS. Besides, not only the RIN spectrum is suppressed over the filter rejection band, but also the out-of-band level is lowered due to the filter insertion loss. The bandwidth dip is also closely related to the gain saturation. The broader dips correspond to the RIN spectra at the PSSs output, caused by a large input optical power provided by the previous RS and the laser source in the case of the first PSS.

Finally, the RIN spectra at the MWP link output is displayed in Fig. 2.15 as a function of the filtering scheme. As a conclusion, the RIN level in the vicinity of the RF signal, which in this case is centred at 15 GHz, is improved by more than 4 dB by using the solution based on BPFs instead of FBGs. Therefore, the SNR_{out} and consequently the NF are also improved by the same amount. This result could be even enhanced by properly tailoring the BPFs responses, that is, by limiting the -3 dB bandwidth accordingly to the RF signal frequency. In addition, the NF could be also enhanced by a proper adjustment of each SOA bias point in terms of injection

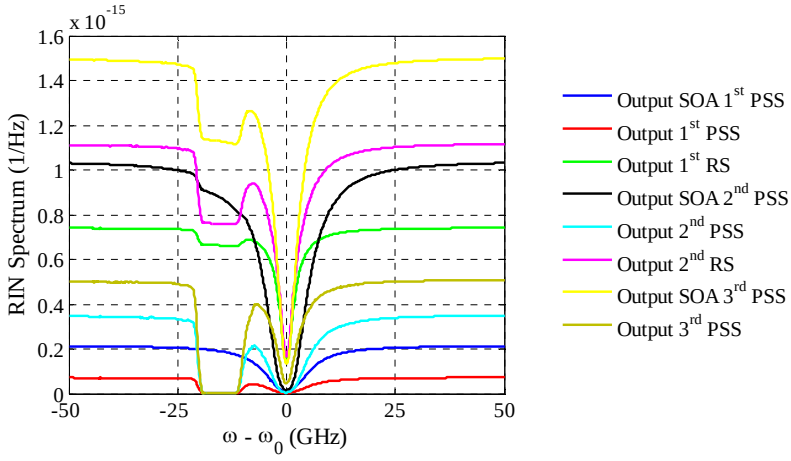

(a)

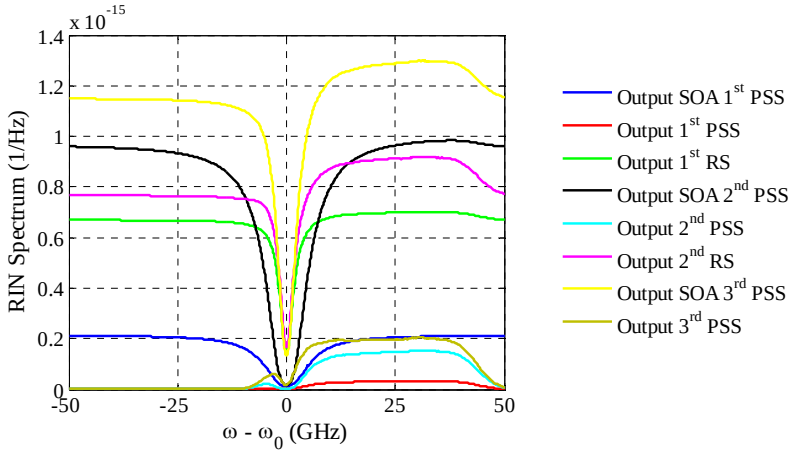

(b)

Figure 2.14: Calculated RIN spectra in different points of the cascaded structure when using three identical (a) FBGs and (b) BPFs.

current and input optical power at each PSS input. It is well-known that the added noise in semiconductor waveguides is proportional to the power gain. By increasing the input optical power and reducing the injection current, the power gain could be lowered without substantially altering the CPO efficiency while operating the SOA in the saturation regime [41]. As a consequence, the SNR_{out} could be improved, thus enhancing the NF.

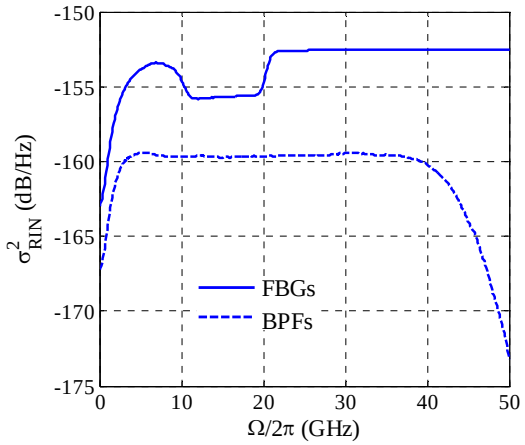

Figure 2.15: Calculated RIN spectral density as a function of the filtering scheme.

2.5 Application: MWP tunable filter

The suitability of using SOA-based cascaded PSS for developing MWP phase shifting functionalities has been demonstrated in [35]. Here, this feature is exploited for the implementation of MWP tunable filtering schemes with complex-valued coefficients. A proof-of-concept approach involving two taps is presented. However, the design can be extended to any arbitrary number of samples. To date, a solution for developing filtering tasks by using as a key element a single PSS has already been proposed [59]. The combination of both SFL effects have been exploited to reach a nearby controllable 2π phase shift by exploiting the phase inversion enabled by the modulator as a function of the bias operating point [59]. Hereafter, the cascaded configuration is deployed instead of using SFL effects in a single PSS.

2.5.1 Principle of operation

The general principle of operation of MWP filters has already been covered in the previous chapter (Sec. 1.3). In this section, these principles are particularized to the implementation of a wideband and tunable photonic-assisted filtering scheme for microwave signals using the cascaded SOA-based phase shifter as a key element. Figure 2.16(a) shows a simplified schematic drawing of a notch-type MWP filter. It basically consists of an interferometric structure which is featured by a time delay imbalance given by T. Moreover, both samples are weighted and phase shifted according to the complex terms a_0 and a_1, where $a_0 = |a_0|\, e^{j\theta_0}$ and $a_1 = |a_1|\, e^{j\theta_1}$.

Figure 2.16(b) displays the typical response for a two-tap complex-valued MWP filter. Roughly speaking, the use of complex-valued samples in FIR filter schemes enable controllable basic phase shift. The capability of changing the basic phase shift results in response tunability without altering the FSR, as shown in Fig. 2.16(b). By increasing the basic phase shift by $\pi/2$ radians, the transfer function is

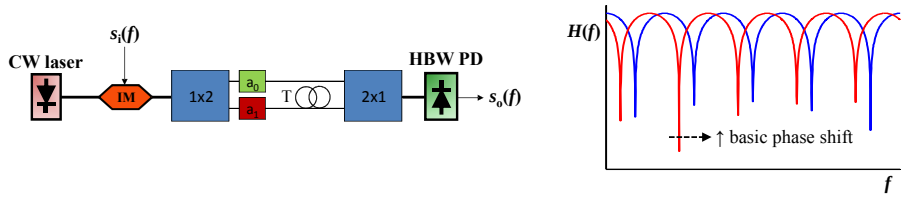

(a) (b)

Figure 2.16: (a) Simplified schematic of a two-tap complex-valued MWP filter. (b) Typical transfer function of a notch-type filter when changing the basic phase shift.

tuned by FSR/4. The electrical transfer function of a notch-type FIR filter can be expressed as [27]:

$$H(f) = \frac{s_o(f)}{s_i(f)} = |a_0| + |a_1| e^{j\theta} e^{-j2\pi fT}. \tag{2.21}$$

In Eq. 2.21, f denotes the RF frequency and T the basic time delay, which is inversely proportional to the FSR. The basic phase shift, θ, is determined by the phase shift difference between both samples, i.e., $\theta = \theta_1 - \theta_0$.

Hence, the cascaded SOA-based MWP phase shifter can be inserted in one arm of the interferometric structure in order to provide controllable basic phase shift. Since phase shifts greater than 2π have been demonstrated using the configuration illustrated in Fig. 2.3, 100 % fractional tuning can be reached, as it is demonstrated in the following section.

2.5.2 Theoretical and experimental results

The experimental setup for the cascaded SOA-based MWP filter is sketched in Fig. 2.17(a). The MWP phase shifter was inserted in the lower arm of the interferometric structure. In this manner, the basic phase shift between both taps can be controlled by properly adjusting the injection currents into the SOAs comprising all the three PSSs. The three optical filters following the SOAs in the each PSS were implemented by means of three narrow-band FBGs with rejection greater than 30 dB. The interferometric structure was characterized by a length imbalance of 0.41 m, which corresponds to a notch-type response with a FSR of roughly 500 MHz. The emission wavelength of the CW laser was fixed to 1552 nm. The VOA in the upper arm provided the microwave power balance between the two samples in order to compensate the power variation caused by tuning the phase shift in the cascaded configuration, thus enhancing the rejection level. At the output of the IM, the double-sided band signal was amplified by means of an EDFA. A 0.8-nm-wide BPF centered at the carrier wavelength was also used for spontaneous noise suppression purposes. The linewidth of the CW laser was around 10 MHz, which results in coherence time of nearly 32 ns. Therefore, to avoid coherency-related problems, a balanced photodetector (BPD) was used since T was around 6.1 ns. The RF input and output signals were, respectively,

generated and acquired by using a high-bandwidth VNA. Prior to the acquirement, the electrical signal was properly amplified (EA). Figure 2.17(b) shows a picture of the assembled experimental setup highlighting the most important devices.

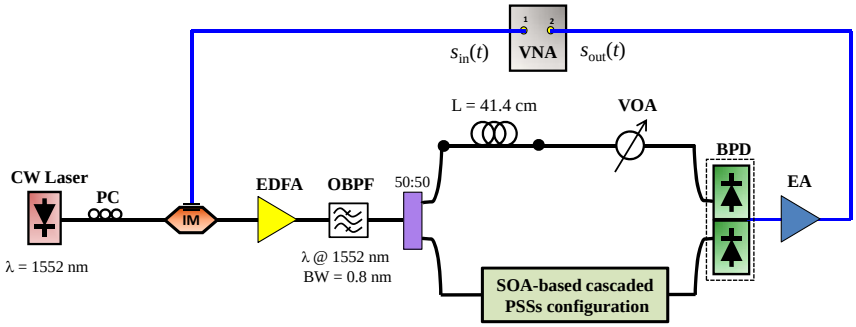

(a)

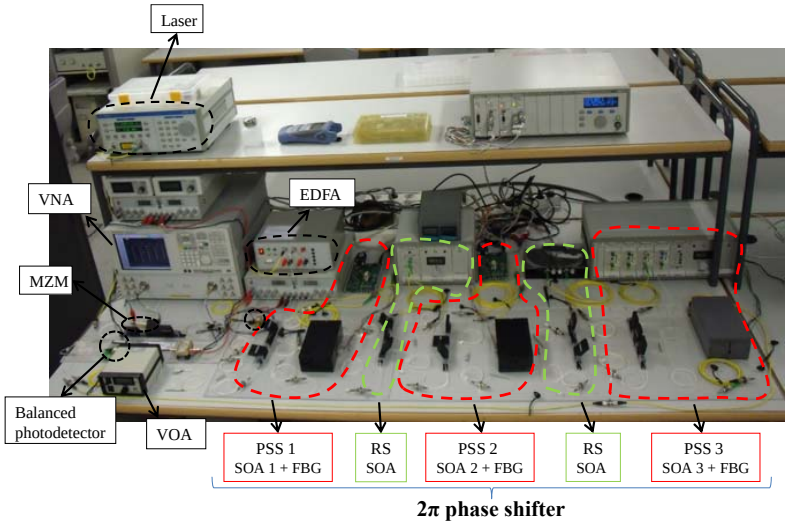

(b)

Figure 2.17: (a) Sketch of the experimental setup for the cascaded SOA-based MWP filter. (b) Picture of the assembled setup showing the main devices.

The filter has been implemented at the operating frequency of 20 GHz over 2 GHz bandwidth, this is, from 19 GHz to 21 GHz. The amplitude variation and phase shift of the 20 GHz RF signal is roughly the same that for 15 GHz, which has been shown in Fig. 2.4. In order to perform distortion-free filter responses, flat phase shift features must be achieved within the usable bandwidth as a function of the different combinations of injection currents into the PSSs. This fact is illustrated in Fig. 2.18. The phase shifts experience constant behavior with the frequency when tuning from 0° to 360°.

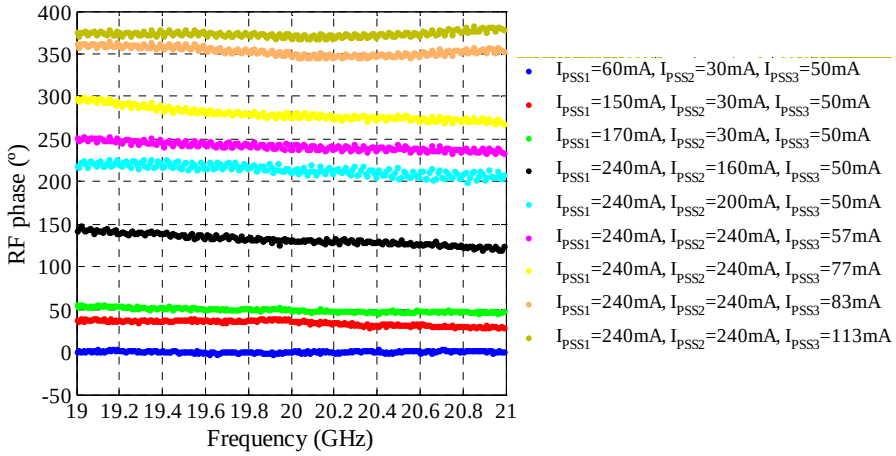

Figure 2.18: Measured phase response of the cascaded SOA-based MWP phase shifter within the usable filter bandwidth.

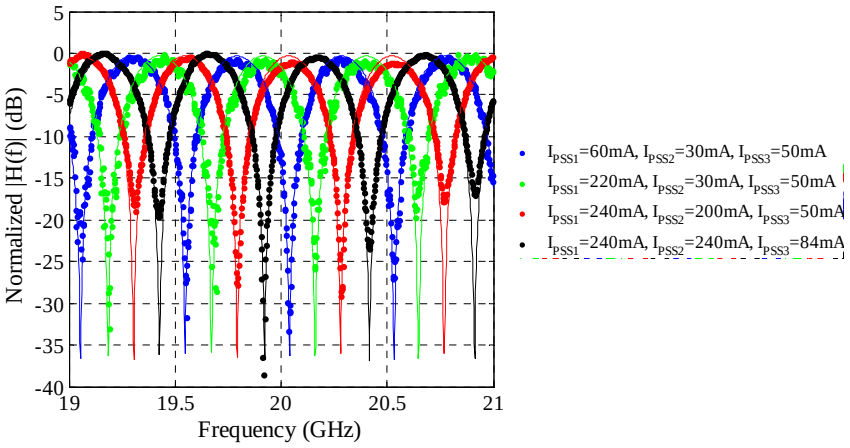

Figure 2.19: (a) Measured (markers) and theoretical (solid curves) normalized amplitude transfer function of the MWP tunable filter for different combinations of the injection currents into the three PSSs.

Figure 2.19 shows the measured (markers) and calculated (solid curves) transfer functions with the injection current. Both experimental and theoretical results show good agreement. Misalignments are due to nonperfectly flat phase responses, in combination with slightly power imbalance between both arms as a function of the frequency and the added noise. As expected, 100% tuning range over the FSR has been accomplished when sweeping the phase shift of the SOA-based configuration from 0° to 360°. Each time that the injection currents are changed for the purpose of tuning the notch positions, the VOA must be adjusted in order to balance the power

in the two arms comprising the interferometric structure prior detection. Rejection levels greater than 20 dB have been reached within the entire spectral range. The reference response (blue trace) has been obtained when injecting 60 mA, 30 mA and 50 mA into the first, second and third PSS respectively. The spectral shape of the filter response remains unaltered since there is no need to change the T in order to tune the transfer function. Stable filter responses have been obtained mediated the use of the BPD thus guaranteeing incoherent regime.

2.6 Summary and conclusions

In this chapter, a noise performance characterization of SFL cascaded SOA-based MWP phase shifters has been accomplished. The noise characteristics, together with other indicators such as the nonlinear distortion and the RF net gain, form a relevant set of FoM aiming at obtaining objective data regarding the signal processor performance. Furthermore, the MWP phase shifter has been used as a key element in the implementation of a tunable photonic-assisted RF filter.

Firstly, a theoretical model to predict the RIN spectral density at the output of SOA-based MWP phase shifters has been described. The model has shown very good agreement with experiments, demonstrating its applicability to assess the RIN level even in presence of the microwave signal. Calculated data have been perfectly consistent with experimental results when non-dispersive optical filters have been used. Moreover, a suitable solution in order to alleviate the noise enhancement induced by FM-AM-noise conversion in dispersive optical filters has been proposed and demonstrated. The ASE-signal beat-note has been identified as the dominant contribution at the output. RIN spectral density levels up to -150 dB/Hz have been obtained at the phase shifter output. From the SNR results, the BPF-based scheme has yielded the optimum noise performance when considering a single PSS. The results can be extended to multi-PSS-based structures. Suppression of the noise level by more than 4 dB has been reached in approaches based on band-pass optical filtering regarding FBG-based schemes, when three PSSs have been cascaded. This result could be further improved by proper BPF response tailoring.

Secondly, the implementation of a MWP tunable filter involving the cascaded SOA-based phase shifter has been carried out. As a proof-of-concept, a notch-type filter centred at 20 GHz has been demonstrated over a 2 GHz bandwidth. A fully continuously tunable filter response of 100% of the a FSR, which has been 500 MHz, has been reached. Rejection levels greater than 20 dB have been obtained.

The objectives of this chapter have been fulfilled and recognized by the community in the following international publications:

1. **J. Lloret**, F. Ramos, J. Sancho, I. Gasulla, S. Sales and J. Capmany, "Noise spectrum characterization of slow light SOA-based microwave photonic phase shifters", IEEE Photonics Technology Letters, vol. 22, no. 13, pp. 1005-1007, 2010.

2. **J. Lloret**, F. Ramos, J. Sancho, I. Gasulla, S. Sales and J. Capmany, "On the noise performance of slow light SOA-based microwave photonic phase shifters",

in IEEE Topical Meeting Microwave Photonics (MWP), Montreal (Canada), paper TH4-28, 2010.

3. I. Gasulla, J. Sancho, **J. Lloret**, S. Sales and J. Capmany, "Figures of merit for microwave photonic phase shifters based on coherent population oscillation slow and fast light effects", in 12th International Conference on Transparent Optical Networks (ICTON), Munich (Germany), invited paper We.B3.2, 2010.

4. **J. Lloret**, F. Ramos, W. Xue, J. Sancho, I. Gasulla, S. Sales, J. Mørk and J. Capmany, "The influence of optical filtering on the noise performance of microwave photonic phase shifters based on SOAs", IEEE Journal of Lightwave Technology, vol. 29, no. 12, pp. 1746-1752, 2011.

5. **J. Lloret**, J. Sancho, I. Gasulla, F. Ramos, S. Sales, and J. Capmany, "Noise figure of slow light cascaded SOA based microwave photonic phase shifters", in Slow and Fast Light conference (SL), Toronto (Canada), paper SLWB5, 2011. *Awarded with a registration waiver granted by the Canadian Air Force Office of Scientific Research (AFOSR).*

6. **J. Lloret**, J. Sancho, I. Gasulla, S. Sales, and J. Capmany, "Performance metrics evaluation of cascaded SOA based slow light microwave photonic phase shifters", in IEEE Topical Meeting Microwave Photonics (MWP), Singapore (Singapore), paper 2175, 2011.

7. J. Sancho, **J. Lloret**, I. Gasulla, S. Sales and J. Capmany, "Figures of merit for microwave photonic phase shifters based on semiconductor optical amplifiers", Optics Express, vol. 20, no. 10, pp. 10519-10525, 2012.

Chapter 3

SFL effects in SOI micro-ring resonators

3.1 Introduction

Silicon Photonics has emerged as the most preferable technology platform for developing several integrated based functionalities in the last decades [60]. From the pioneering works showing the viability of silicon crystals efficiently operating at 1.3 and 1.6 μm published by Soref in the late 1980s and early 1990s [61–63], impressive advances have been accomplished. The huge growth of *Silicon Photonics* has been mainly mediated by a combination of cost and technological reasons [64].

On one hand, the cost issues are related to the absolute cost of silicon and SOI wafers as compared to other materials such as the III-V compounds or the lithium niobate. Moreover, silicon is a well-understood and robust material whose fabrication processes have been intensively developed by the electronics industry to a level that is more than sufficient for most integrated optical applications. Consequently, silicon-based technology can benefit from economics of scale for mass-market applications, resulting in low-cost and CMOS-compatible solutions [64, 65].

On the other hand, the technological reasons rely on the high index contrast, the transparency at telecommunication wavelengths and the possibility of refractive index modulation via several techniques. The high index contrast between Si ($n = 3.45$) and SiO_2 ($n = 1.45$) offers a strong optical confinement, which makes possible to scale photonic circuits to the hundreds of nanometer level. Moreover, silicon is suitable for low-loss waveguiding at the fiber-optical communications wavelengths, being transparent for $\lambda > 1.2$ μm. Other important issue is associated with the possibility of optical phase and amplitude modulation by means of refractive index modification, which can be assisted by different techniques based on thermo-optic effects and free carrier dispersion (FCD). Although these refractive index modulation techniques are not as fast as field-effect mechanisms available in other technologies, such as the Pockels effect in lithium niobate, is sufficient for many communications and sensor applications. Moreover, silicon has other excellent properties including high thermal

conductivity ($\sim$ 10 $\times$ higher than GaAs) and high optical damage threshold ($\sim$ 10 $\times$ higher than GaAs). Kerr effect is 100 times larger, whereas Raman effect is 1000 times stronger than those in silica fiber [64, 65]. In contrast, both Kerr and Raman effects are inevitably accompanied by a strong two-photon absorption. Consequently, this fact hampers the efficient exploitation of silicon for nonlinear optics.

These properties have led to the efficient and cost-effective implementation of several optical devices based on SOI with application to computing, communications and sensing [65]. In particular, guiding [66], modulating [67], emitting [68] and detecting [69] light functionalities have been intensively developed in recent years. Photonic-wire loss $<$ 1 dB/cm with cross-sectional area of about 0.1 μm^2 have been already fabricated using electron-beam lithography and dry-etching [70]. Electro-optical modulators operating at several tens of Gbps based on carrier depletion in Mach-Zehnder interferometers (MZI) [71] and MRRs [72] have been also demonstrated so far. Despite the indirect band gap nature of silicon, different physical mechanisms and techniques have been exploited to implement laser emission and amplification [65], receiving a particular attention those based on Raman scattering [73–76]. Likewise light emission, detection is difficult in silicon due to the low absorption at telecommunication wavelengths. Wafer bonding of different III-V group materials on top of patterned SOI circuits have been presented as a suitable solution [69, 77].

Moreover, next generation optical networks tends towards all-optical solutions. To this purpose, the development of RF and data signal processors in the optical domain represents a key point to be accomplished. Among all the functionalities to be developed, the implementation of filtering tasks free from bandwidth constraints [27] and optically fed phase array antenna systems [78] are of great interest. To this end, the efficient design of broadband tunable microwave phase shifters and tunable true time delay lines are critical issues [79, 80]. In this context, SFL techniques implemented on different integrated platforms have been recently demonstrated as suitable solutions [5].

In this chapter, monolithically integrated SOI MRRs are used as key elements in the implementation of RF photonic signal processing. Firstly, the device structure and the fabrication flow will be described. Then, a novel tunable and reconfigurable MWP filter will be demonstrated exploiting SFL effects in a single SOI MRR. The performance will be evaluated through theoretical and experimental results. The selectivity and rejection ratio will be studied by considering different windowed-type taps. Next, SOI-based MRRs will be exploited for the implementation of broadband multi-channel TTD lines provided by the resonant nature of the MRR in combination with using an extended SCT technique. An approach will be presented based on an array of cascaded MRRs. Finally, the main conclusions will be derived.

3.2 Device structure and fabrication

The schematic drawing of the device structure is sketched in Fig. 3.1(a). It basically consists of a SOI MRR in-plane coupled to a nanophotonic waveguide. On top, a micro-heater is bonded aiming at enabling group index modulation by means of the thermo-optic effect [81]. The tunable MRR was fabricated using an SOI wafer with a top silicon thickness of 250 nm and 3 μm buried silicon dioxide. Diluted

(1:1 in anisole) electron-beam resist was spin-coated on the wafer to create a ∼ 110-nm-thick masking layer. The micro-ring structure was defined by using electron-beam lithography. The patterns were subsequently transferred to the top silicon layer with inductively coupled plasma reactive ion etching. Then, a 550-nm-thick benzocyclobuten (BCB) top cladding was spin-coated hard-cured. Following, a 400-nm-thick resist and electro-beam lithography were employed to define the micro-heater pattern. Finally, evaporation and lift-off techniques were used to grow the 100-nm-thick titanium heaters together with the contact pads [82, 83].

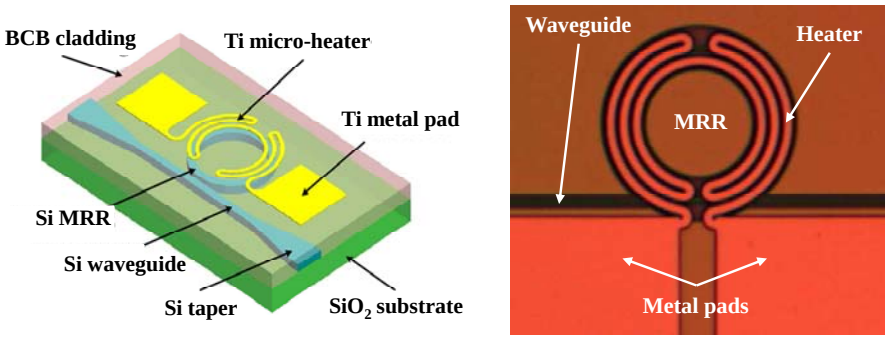

(a) (b)

Figure 3.1: (a) Schematic drawing of the MRR structure [83]. (b) Footprint picture of the fabricated device [83].

A footprint picture of the fabricated device is displayed in Fig. 3.1(b), showing the MRR, the waveguide and the micro-heater with the metal pads. A MRR featuring a radius of 250 μm with a waveguide width and height of 500 nm and 200 nm respectively is used. On the MRR, the heater width is 1 μm. The power coupling factor is mainly determined by ring-to-waveguide gap, which is 200 nm. Tapered input and output ports expanding from 500 nm to 4 μm are implemented in order to optimize the fiber-to-chip coupling. The total insertion loss of the device is ∼ 15 dB [82, 83].

3.3 Basic properties of SOI MRRs

A MRR consists of a waveguide bent onto itself in a circular shape, which is side-coupled to a straight waveguide. Light travelling through the straight waveguide whose wavelength is a submultiple of the optical path length L is coupled into the ring resulting in a standing wave pattern. This wavelength is therefore on-resonance with the ring cavity and it is defined as $\lambda_{res,m} = (L/m)\, n_{eff}$, where m and n_{eff} are an integer and the effective index respectively. On the other hand, wavelengths departing from the resonance ones, simply travel along the straight waveguide from input to output without being coupled into the cavity. Consequently, a MRR is characterized by a wavelength-selective response, where the intensity transmission factor H is defined as [84]

$$H = \frac{a^2 - 2ka\cos(\Phi) + k^2}{1 - 2ka\cos(\Phi) + k^2a^2}, \tag{3.1}$$

where k and t correspond to the coupling and transmission factors respectively, which satisfy the relation $k^2 + t^2 = 1$. The term a refers to the amplitude transmission coefficient for a round-trip along the ring. The term Φ corresponds to the round-trip phase shift and it is defined as $\Phi = 2\pi n_{eff} L/\lambda$. Note that the transmission at resonance, i.e., null cosine argument, drops to zero when $k = a$. In this case, the internal and the coupling losses are equal, being the MRR critically coupled. A very sharp 2π phase change takes place at each resonance wavelength. For $k > a$, the MRR is said to be under-coupled. Near each resonance, the phase undergoes a rapid variation with respect to the round-trip phase-shift. Finally, for $k < a$ the MRR is said to be over-coupled, leading to a phase response experiencing a monotonically 2π phase change whose slope is directly related to the notch depth. This concept is illustrated in Fig. 3.2.

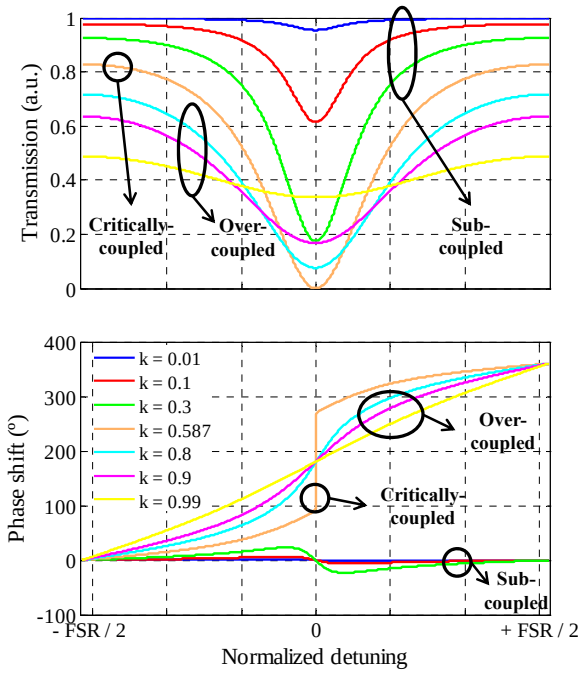

Figure 3.2: Transmission and phase shift centred at one resonance of the MRR under different coupling regimes.

The phase of the transmitted light is defined as [84]

$$\phi = \pi + \Phi + \arctan\left(\frac{k\sin(\Phi)}{a - k\cos(\Phi)}\right) + \arctan\left(\frac{ka\sin(\Phi)}{1 - ka\cos(\Phi)}\right). \tag{3.2}$$

For developing signal processing tasks, the over-coupled regime is specially interesting since lower power penalty compared with the critically coupled case is reached and still 2π phase-shifts. In the vicinity of the resonance wavelengths, a dispersive feature mediated by the notch nature of the MRR occurs. The potentially controllable dispersive profile enables the implementation of SFL effects. Therefore, the light propagation can be governed by acting on the inherent dispersive behaviour of MRRs. In particular, the k and the n_{eff} can be modified for the purpose of controlling the dispersive profile, as also shown in Fig. 3.2. On one hand, a n_{eff} change enables resonance wavelength tunability. On the other hand, the dispersive profile can be modified by proper k adjustment.

3.4 Applications

In this section, SOI-based MRRs have been used in the implementation of several applications. In particular, the MRR has been exploited when developing RF signal processing tasks. Firstly, a reconfigurable and tunable MWPF using a single SOI MRR as key element is demonstrated. Following, a new technique suitable for overcoming the inherent bandwidth limitation in slow-light resonant-type elements is introduced, which is named as extended SCT. Finally, a novel approach based on an array of cascaded MRRs in combination with using OSSB modulation and the extended SCT technique are proposed aiming at implementing multi-channel TTD lines.

3.4.1 Reconfigurable and tunable MWP filter

3.4.1.1 Principle of operation

The general principle of operation of MWP filters has already been covered in Sec. 1.3. In this section, these basics are particularized to the implementation of a reconfigurable and tunable photonic-assisted filtering scheme for microwave signals using a single MRR as the key element.

A simplified scheme showing the main functional blocks of the reconfigurable and tunable MWP FIR filter is sketched in Fig. 3.3. A laser array made of N laser sources is employed. The electrical input signal, $s_i(t)$, is transferred onto all the N optical carriers generated by the laser array by means of an IM operated in the dual-drive configuration, giving as a result OSSB modulation. The optical signal at the output of the IM is then launched in a wavelength-selective delaying element. This element provides the corresponding basic delay between adjacent samples to synthesize the desired FSR of the filter response. In this particular case, tunability is accomplished by modifying the basic phase shift. This fact enables filter tunability without altering the FSR, as already discussed in Sec. 1.3. For this purpose, a controllable phase shifting element is connected to the delay element output. This element, which is implemented by a single SOI MRR, allows for inducing the corresponding basic phase shift between adjacent samples. Finally, the light at the output of the phase shifter is collected by a photo-detector resulting in the filtered RF signal, $s_o(t)$.

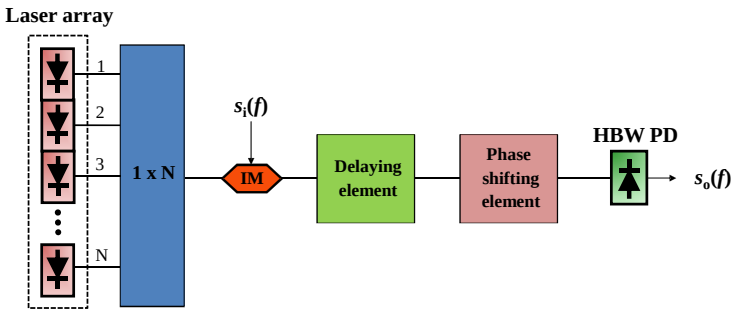

Figure 3.3: Simplified scheme of the reconfigurable and tunable MWP filter.

The electrical transfer function of the FIR filter can be expressed as:

$$H(f) = \frac{s_o(f)}{s_i(f)} = \sum_{r=0}^{N-1} |a_r| e^{jr\theta} e^{j2\pi frT}, \tag{3.3}$$

where the tap amplitude, a_r, the basic delay, T, and the basic phase shift, θ, can be controlled by properly adjusting the output power of each optical source in the laser array, the dispersive profile of the delaying element and the phase-shift feature of the phase shifter, respectively. In this particular case, the T is fixed, whereas the θ is controllable.

As already discussed in Sec. 3.3, the amplitude transfer function for a SOI-based MRR is featured by a resonant-type response. In the over-coupled regime, a full 2π optical phase shift occurs in each notch position. This fact in combination with using OSSB modulation has already been exploited in the implementation of RF photonic phase shifters [82, 83, 85, 86]. Here, the optical phase of a single MRR is used for simultaneous and independently phase shifting all the samples comprising the MWP filter. Consequently, controllable basic phase shift is performed.

The principle of operation is depicted in Fig. 3.4, in which both the gain and phase transfer functions of the MRR, together with the sample spectral positions are shown. As an exemplary case, 4 samples are considered. However, this case can be extended to any arbitrary number of samples. For simplicity purposes, a single spectral line is plotted as modulation sideband, however, in practice it consists of a wideband signal. It basically relies on the fine adjustment of the emission wavelengths for all the N optical carriers within the phase transfer function of the MRR. In particular, the phase of the *r-th* sample, $r\theta$, is given by the phase difference between the *r-th* optical carrier and its corresponding modulation sideband. In this way, the mechanism for phase synthesis focusses on the proper adjustment of each laser emission wavelength, in accordance with the MRR optical phase transfer function. In Fig. 3.4(a), $\theta = 0$, since the relative phase shift between adjacent samples is zero. Conversely, $\theta \geq 0$ in Fig. 3.4(b). Consequently, filter response tunability is performed when changing from the scenario depicted in Fig. 3.4(a) to that shown in Fig. 3.4(b).

The center frequency of the MWP filter is limited by the optical phase transfer function of the MRR. In particular, the abruptness of the phase slopes establish

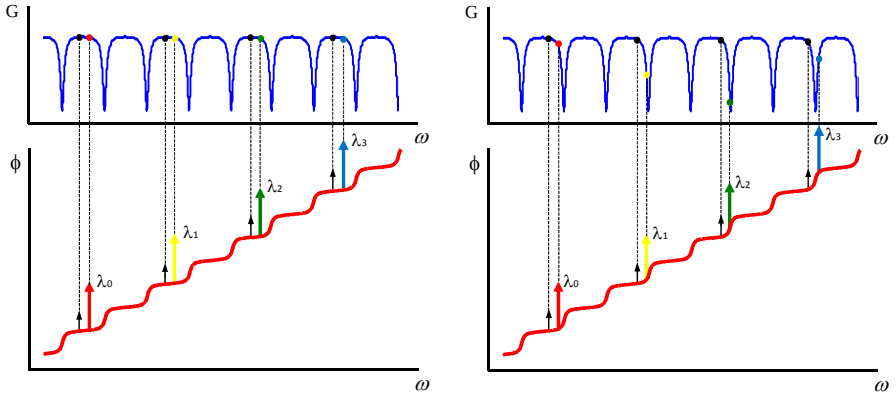

(a) (b)

Figure 3.4: Spectral position of the samples within the amplitude and phase transfer functions for (a) $\theta = 0$ and (b) $\theta \geq 0$.

the minimum RF frequency able to obtain the maximum phase shift between an optical carrier and its corresponding modulation sideband. Moreover, due to the resonant-type nature of the MRR response, a phase shift is also accompanied by a power penalty in accordance with the amplitude transfer function. This fact can be particularly observed in Fig. 3.4(b). The mentioned power penalty can be readily compensated by adjusting the output power for all the N laser sources independently. Moreover, the control of the emission power for all the samples can be also exploited for implementing windowed samples. This fact at the end results in enhanced filter responses in terms of quality factor (Q) or side-lobe level (SLL), as will be shown in Sec. 3.4.1.3. It is important to remark that the technique of combining OSSB modulation with passive optical filtering to implement complex-valued filters was originally proposed in [87], where phase shifters based on fiber Bragg gratings (FBG) instead of SOI MRR were considered.

3.4.1.2 Theoretical and experimental results

In this section, theoretical and experimental results of the SOI MRR-based reconfigurable and tunable filter are presented. First, the SOI MRR characterization is accomplished. Secondly, the tuning range of the filter response is studied as a function of the number of samples.

The assembled experimental setup aiming at characterizing the MRR transfer function is sketched in Fig. 3.5. Both the gain and phase transfer functions over a huge frequency range were measured using the method proposed in [88]. For this purpose, a CW tunable laser generating a weak spectral line with 0-dBm-power was used. The optical emission frequency was swept from 192.7 THz to 193 THz approximately. A 500 MHz modulating signal generated by the VNA fed the IM, which was set in single-drive configuration by terminating one electrical input port with an impedance of 50 Ω. The electrical power of the modulating signal was adjusted in order to

obtain a modulation depth of 0.5%. At the IM output, a booster EDFA was used to compensate the excess loss due to fiber-to-chip and chip-to-fiber coupling. Then, the 10-dBm-power optical signal was input to the 250-μm-radius MRR. The 200 nm ring-to-waveguide gap fix the power coupling factor, which is around 68%. The footprint area including the MRR, the metal pads and the tapered ports is around 10 mm^2. Polarization controllers were inserted at both the modulator and MRR inputs to avoid power penalty derived from polarization mismatching. Finally, the optical signal exiting the MRR was collected by a HBW PD and acquired by the VNA.

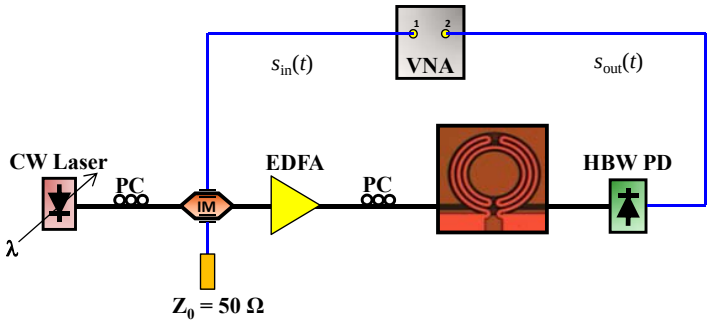

Figure 3.5: Experimental setup used for characterization purposes.

The bias-free transmission and phase characteristics of the MRR are displayed in Fig. 3.6. Both the experimental and theoretical results are shown. Misalignments in the resonance amplitudes are mainly due to fabrication-related inaccuracy. Calculated results have been obtained following the theoretical analysis presented in Sec. 3.3. The values of the main parameters used for the calculations are given in Table 3.1. As expected, the gain experiences a resonant-type response with a FSR of roughly 44.35 GHz. The width and depth of the periodic response notches mainly depends on k. In particular, the MRR is over-coupled since 2π phase-shift occurs at each notch position.

Symbol	Definition	Value
R	MRR radius	250 μm
k	Power coupling factor	68 %
Z_0	Detector input impedance	50 Ω
α	Internal loss	2 dB/cm
n_g	Group index	4.306
T	Temperature	25°C

Table 3.1: Main parameters used for calculations.

Once the MRR has been characterized, the suitability for implementing complex-valued coefficients in tunable filtering schemes is next demonstrated.

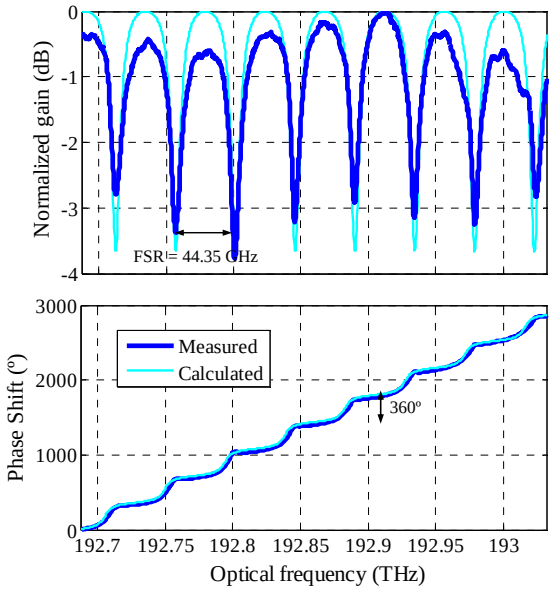

Figure 3.6: MRR transmission and phase characteristics.

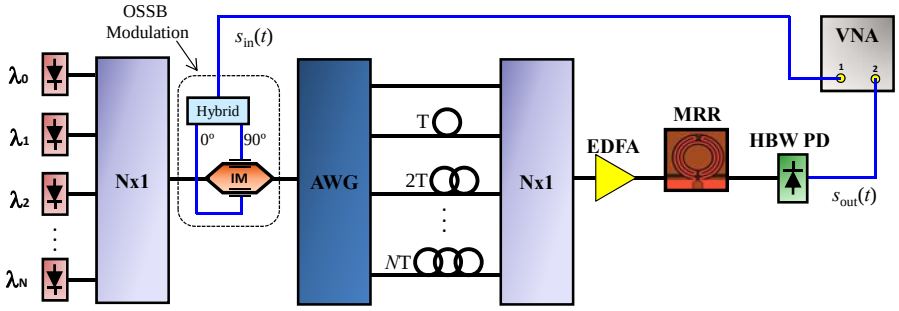

Figure 3.7: Experimental setup for the MWP reconfigurable and tunable filter.

Figure 3.7 sketches the experimental setup of the MRR-based MWP filter. The approach implements a FIR filter, in which a number of taps N were generated by using an array of optical sources made of N tunable lasers operating in CW. The input RF signal, $s_{in}(t)$, was transferred on all the N optical carriers by means of an IM operated in dual-drive configuration, giving as a result OSSB modulation, as seen in Fig. 3.8(a). A center frequency of 20 GHz was chosen aiming at allowing large phase shift between the *r-th* optical carrier and its corresponding sideband according to the MRR phase transfer function. Besides, zero phase imbalance between the minimum and maximum frequencies along the filter band is required to avoid the degradation due to distortion in the filter transfer function. Consequently, the bandwidth was limited to 1 GHz spanning from 19.5 GHz to 20.5 GHz. The modulation index was

fixed to be 0.5 %. Then the N modulated optical carriers were sampled by an arrayed waveguide grating (AWG), which is featured by a channel spacing of 0.8 nm. This fact limits the emission wavelength of all the N CW tunable lasers, however, it is not an issue in our particular approach. Each sample was independently delayed through the propagation along different optical delay lines. The delay difference between all the samples was $T = 5.8$ ns, as is shown in Fig. 3.8(b) within the filter bandwidth. Moreover, all the samples were combined again, amplified using an EDFA and injected into the MRR. The samples were then weighted and phase-shifted according to the MRR transfer function, which has already been shown in Fig. 3.6. Finally, the optical signal exiting the MRR was photodetected and acquired by a VNA. In such a way, at the HBW PD output the RF signal, $s_{out}(t)$, was composed of the interference of all the N weighted, delayed and phase-shifted samples.

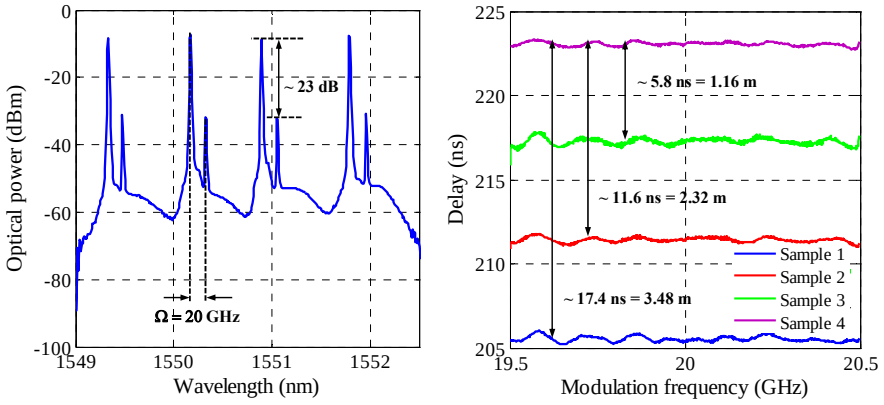

Figure 3.8: (a) OSSB modulation spectrum (b) Delay within the filter bandwidth for each sample.

Proof-of-concept implementations involving $N = 2$, 3 and 4 samples have been considered. However, the design can be extrapolated to any arbitrary number of samples. By exploiting the MRR periodical phase response, the phase shifts are independently implemented for all the two, three and four coefficients designs respectively, a feature which is required in a multi-tap complex-valued tunable MWP filter.

Firsty, Fig. 3.9 shows the spectral placement of the optical carriers and the corresponding 1 GHz bandwidth sideband range on the MRR optical phase response when considering the two-tap implementation. Figure 3.9(a) shows the scenario in which the phase difference between carrier and sideband for both samples is the same and minimum, being around 38°. This fact results in $\theta = 0$. In contrast, Fig. 3.9(b) shows the samples spectral placement when θ is the maximum and equal to 276°. To increase θ, the emission wavelength of the *sample 2* was changed. In this way, the phase shift between the optical carrier and modulation sideband of the *sample 2* was adjusted to 314°, resulting in 276° of phase imbalance between both samples, i.e., θ.

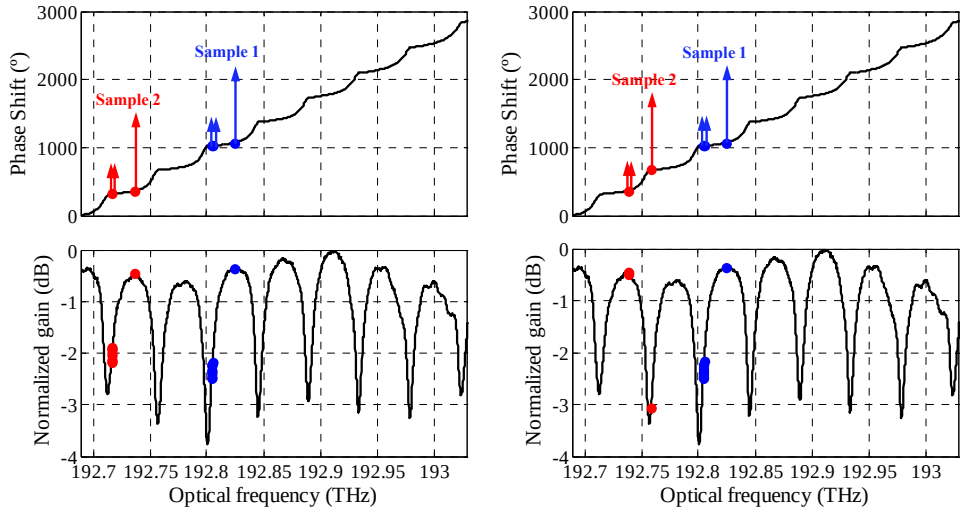

Figure 3.9: Samples spectral placement on the MRR transfer function for (a) $\theta = 0$ and (b) $\theta = 276^{\circ}$ when $N = 2$.

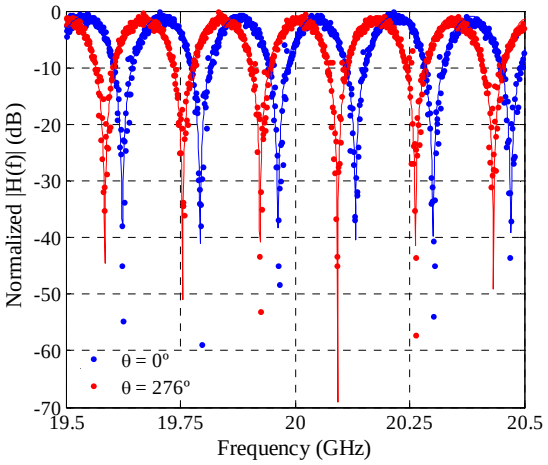

Figure 3.10: Filter responses for the minimum and maximum θ when $N = 2$.

Figure 3.10 displays the filter frequency response. As expected, a notch-type response featuring a FSR of approximately 172 MHz is obtained. Experimental (markers) and theoretical (solid curves) results show good agreement. Small deviations are attributed to reflections in the electrical part of the setup and the residual unwanted sideband in the OSSB modulation. By progressively sweeping the emission wavelength of the *sample 2* while keeping fixed that corresponding to the *sample 1*, a continuously tunable θ from 0° to 276° can be implemented. This fact leads to continuously tunable

77% fractional tuning over the FSR. The excess loss affecting the *sample 2* derived from the θ tunability was compensated by adjusting the corresponding laser emission output power in order to implement uniformly apodized filter responses.

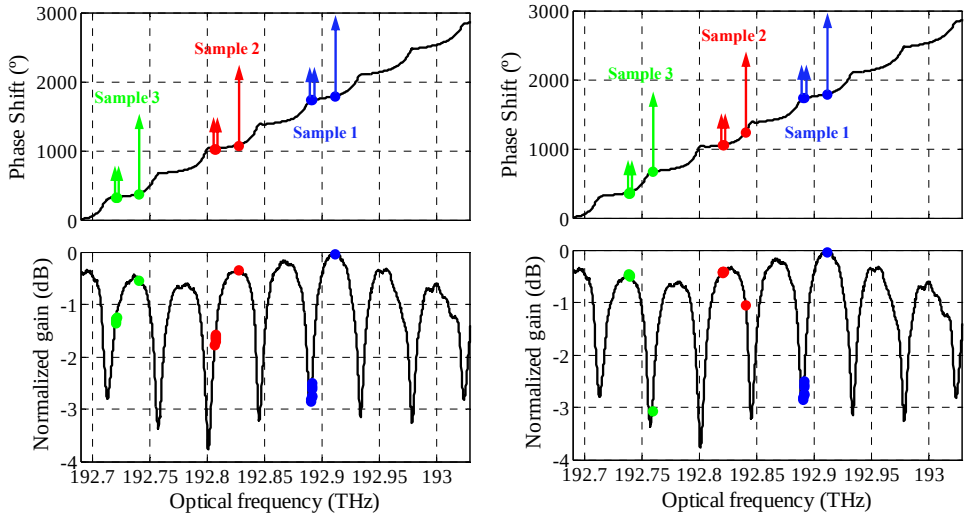

Figure 3.11: Samples spectral placement on the MRR transfer function for (a) $\theta = 0$ and (b) $\theta = 135^{\circ}$ when $N = 3$.

Then, Fig. 3.11 shows the spectral placement of the optical carriers and the corresponding 1 GHz bandwidth sideband range on the MRR optical phase response when considering the three-tap implementation. Figure 3.11(a) shows the scenario in which the phase difference between the carrier and the sideband for all the three samples is the same and minimum (around 50°), resulting in a $\theta = 0$. Conversely, Fig. 3.11(b) shows the samples spectral placement when θ is the maximum and equal to 135°. To increase θ, the emission wavelength of the *sample 2* and *sample 3* were changed. In this respect, the phase shift between the optical carrier and modulation sideband of the *sample 2* and *sample 3* were adjusted to 185° and 320° respectively. As a consequence, a 135° phase imbalance between all the three samples, i.e. θ, is realized.

The filter frequency response is shown in Fig. 3.12. This time, a bandpass-type response is obtained, featuring the same FSR of approximately 172 MHz. Again, experimental (markers) and theoretical (solid curves) results show good agreement. By progressively sweeping the emission wavelength of the *sample 2* and the *sample 3* while keeping fixed that corresponding to the *sample 1*, a continuously tunable θ from 0° to 135° can be implemented. This range corresponds to continuously tunable 38% fractional tuning over the FSR. Likewise the previous implementation involving 2 taps, uniform window was applied. For this purpose, the excess loss affecting both the *sample 2* and *sample 3* was compensated.

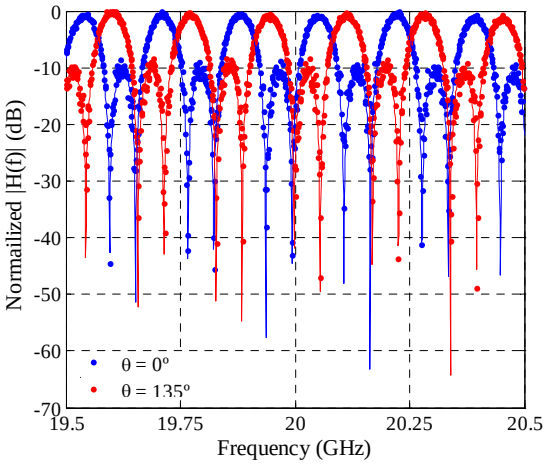

Figure 3.12: Filter responses for the minimum and maximum θ when $N = 3$.

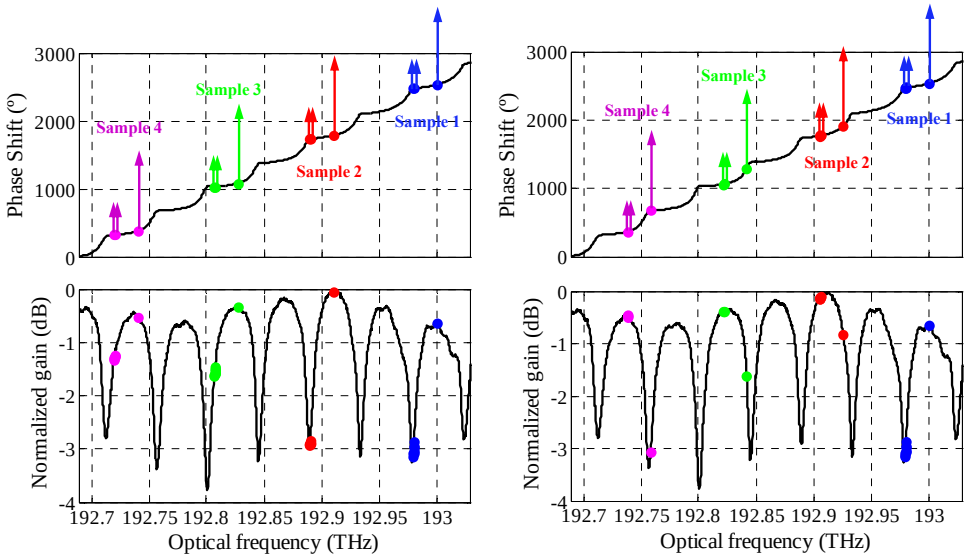

(a) (b)

Figure 3.13: Samples spectral placement on the MRR transfer function for (a) $\theta = 0$ and (b) $\theta = 90^{\circ}$ when $N = 4$.

Finally, the spectral placement of the optical carriers and the corresponding 1 GHz bandwidth sideband range on the MRR optical phase response when considering the four-tap implementation are depicted in 3.13. Figure 3.13(a) shows the scenario in which the phase difference between carrier and sideband for all the four samples is the same and minimum (around 51° in this case), resulting in $\theta = 0$. On the other

hand, Fig. 3.13(b) shows the samples spectral placement when θ is the maximum and equal to 90°. Similarly, in order to increase θ, the emission wavelength of the *sample 2*, *sample 3* and *sample 4* were changed. To this aim, the phase shift between the optical carrier and modulation sideband of the *sample 2*, *sample 3* and *sample 4* were adjusted to 141°, 231° and 321° respectively. Consequently, a 90° phase imbalance between all the four samples, i.e. θ, is accomplished.

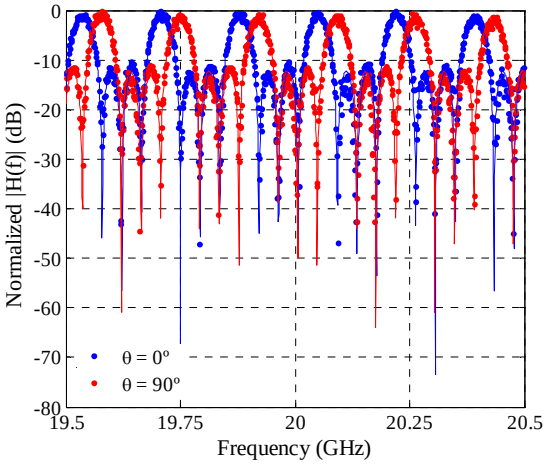

Figure 3.14: Filter responses for the minimum and maximum θ when $N = 4$.

The filter frequency response is illustrated in Fig. 3.14. Likewise the previous configuration, a bandpass-type response featuring a FSR of approximately 172 MHz is obtained, but this time more selective since the number of samples is increased from three to four. Experimental (markers) and theoretical (solid curves) results also show good agreement. By progressively sweeping the emission wavelength of the *sample 2*, *sample 3* and *sample 4* while keeping fixed that corresponding to the *sample 1*, a continuously tunable θ from 0° to 90° can be implemented. This θ range corresponds to continuously tunable 24% fractional tuning over the FSR. Likewise the previous implementations, rectangular window was applied. For this purpose, the excess loss affecting the *sample 2*, *sample 3* and *sample 4* was compensated according to the θ value.

As expected from Eq. 3.3, measurements corroborate that both the FSR and shape of the filter have not been altered when its frequency response is tuned. Ideally, fractional tunings following FSR/(N −1) could be reached. However, zero minimum RF phase shift has not been obtained in practice. In particular, minimum phase shifts of 38°, 50° and 51° for the two, three and four samples approaches have been respectively obtained due to the MRR phase response nature. That is the reason why fractional tunings of the 100%, 50% and 33% have not been respectively achieved. Hence, there exists a trade-off between the tuning range and the number of samples. Specifically, the larger the number of samples, the lower the tuning range. However, the use of cascaded MRRs represents a suitable solution to enhance the fractional tuning. In particular, by cascading m identical MRRs, the maximum θ can be extended by a factor of m. To get fully tunability, controllable θ spanning from 0° to 360° must

be implemented. This means that the cascade of 4 MRRs could enable fully tunable responses in the previous four-tap configuration.

3.4.1.3 Enhancing the performance through windowed samples

Windowed samples have been demonstrated so far to reduce the undesirable effects related to spectral leakage in harmonic processing systems [89]. Within the filtering field, a considerable variety of windows have been evaluated [89]. Different performance improvements have been obtained in terms of Q and SLL according to the window features [89].

Window	Definition
Rectangular	$w(n) = 1$
Triangular	$w(n) = 1 - \frac{\lvert n \rvert}{N/2}$
Hamming	$w(n) = B + (1 - B)\cos\left(\frac{2\pi}{N} n\right)$

Table 3.2: Windows.

Figure 3.15 shows the theoretical and experimental results for the four-tap filter response when applying four different kind of windows. Good agreement between calculated data (solid curve) and measurements (markers) is reached. Specifically, rectangular (uniform), triangular and Hamming based windows have been studied. More details about the windows used can be found in Tab. 3.2. In the case of the Hamming window, two different values of the B-parameter have been considered. In particular, no changes in the approach scheme are required and windowed samples can be readily implemented acting on the emission power of the N sources comprising the laser array.

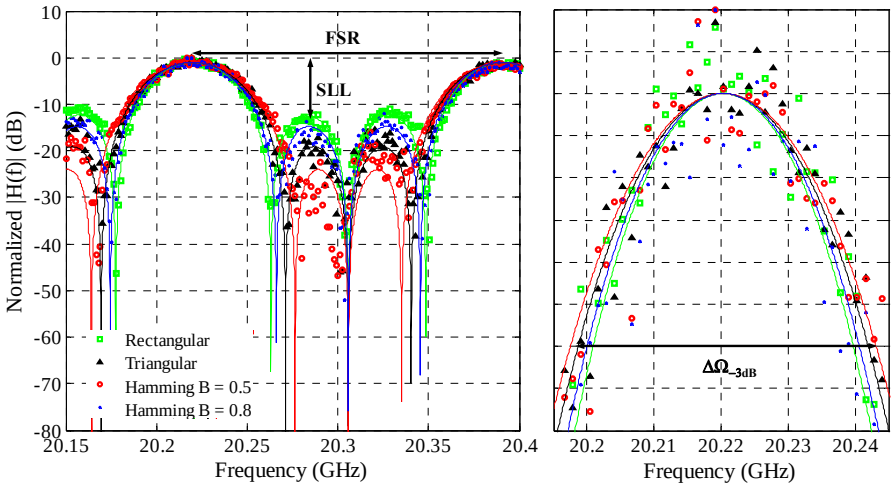

Figure 3.15: Filter responses as a function of the sample windowing when $N = 4$.

Different performance in terms of selectivity and SLL are obtained as a function of the sample apodization, as shown in Fig. 3.16. The filter selectivity is evaluated using the Q, which is defined as the ratio between the FSR and the resonance bandwidth measured at -3 dB from the maximum, $\Delta\Omega_{-3dB}$. Results show an SLL improvement by more than 12 dB when considering the Hamming window with $B = 0.5$ regarding the uniform window based scenario. The best selectivity is obtained by using the rectangular window. However, the out-of-band rejection level given by the SLL is the lowest. On the other hand, the maximum performance attending to the SLL is obtained by the Hamming window with $B = 0.5$, but it is characterized by the worst selectivity. The Hamming with $B = 0.8$ and triangular windows establish intermediate cases. Hence, improvements on both the selectivity and the SLL cannot be simultaneously obtained and the choice of using a certain window is application-dependent.

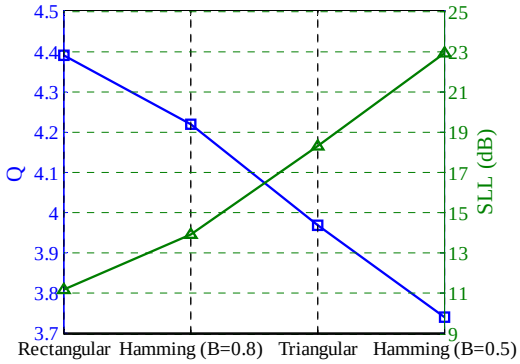

Figure 3.16: Q and SLL results as a function of the sample windowing when $N = 4$.

3.4.2 Multi-channel true time delaying line

3.4.2.1 Principle of operation. Extended Separate Carrier Tuning (E-SCT) technique

Since the first observation of SFL regime in MRRs [90], intensive efforts have been put in the development of efficient and broadband optical delay lines and buffers. High-index-contrast silicon MRRs having extremely small footprints and a high intrinsic Q have been demonstrated, as already mentioned in Sec. 1.2. However, as in any arbitrary resonant system, the enhancement of group delay in a high-Q MRR is always associated with a narrowed spectral bandwidth, thus limiting the maximum bit rate of the optical signal that can be delayed without distortion. Cascading several MRRs with relatively low coupling-dominated Q is therefore viewed as a winning design strategy for facing the trade-off between the footprint, delay and spectral bandwidth [22, 91].

Despite enhanced constant-delay bandwidths in the order of several GHz can be achieved by using special designs [92, 93], in most practical cases is still insufficient

for developing certain RF photonic signal processing tasks. To overcome this limitation, the so-called SCT technique leads to significant performance improvement [94]. Normally, in MWP systems, the RF subcarrier frequency is much higher than the bandwidth of the conveyed signal. Therefore, no information is carried in the broad frequency spacing between the optical carrier and the single-sideband microwave envelope. In this particular context, to separately tuning the optical phase of the carrier results in a useful solution. Thus, the requirement of constant group (time) delay across the entire bandwidth can potentially be relaxed across this region as long as an appropriate phase-shift is also imparted to the carrier.

Hereafter, an extrapolation of the SCT technique, from now on named extended SCT (E-SCT), is proposed. The E-SCT technique enables the implementation of multi-channel true time delaying lines by exploiting the unique features of MRRs. The principle of operation is illustrated in Fig. 3.17(a).

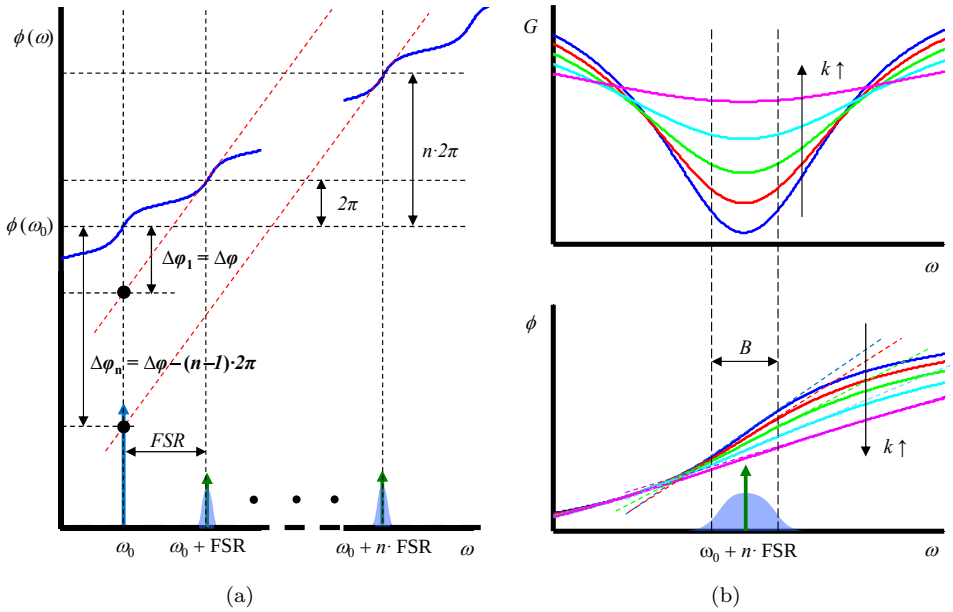

Figure 3.17: (a) Principle of operation of E-SCT MRR-based multi-channel TTD line. (b) Detail of the gain and phase response as a function of the k.

A OSSB modulated signal composed of N RF carriers is considered. Information from N channels with bandwidth B Hz is conveyed on each RF carrier. The technique relies on accommodating all the N RF carriers in different resonances of the MRR transfer function. Therefore, the RF modulation frequency for the *n-th* carrier must be n times the MRR FSR. Moreover, to avoid distortion on the delayed output signal, the channel bandwidth B must fit in the linear phase region occurring in each resonance, i.e., where flat delay is reached. However, to meet the TTD condition, the phase response must be a linear function of frequency over the whole usable bandwidth [94], i.e., $\tau_{a,n} = \tau_{b,n}$ for $n \in [1, N]$ being:

$$\tau_{a,n} = \left. \frac{d\phi(\omega)}{d\omega} \right|_{\omega_0 + n \cdot FSR} \tag{3.4}$$

$$\tau_{b,n} = \frac{\phi(\omega_0 + n \cdot FSR) - \phi(\omega_0)}{n \cdot FSR} \tag{3.5}$$

For this purpose, an extra phase shift $-\Delta\varphi_n$ must be induced on the optical carrier since the real phase value $\phi(\omega_0)$ deviates from the one which guarantees TTD operation.

$$\Delta\varphi_n = \Delta\varphi - (n-1) \cdot 2\pi \tag{3.6}$$

It is important to remark that the same phase slope is affecting all data channels, as well as a 2π phase-shift occurs between adjacent resonances as shown in Fig. 3.17(a). As a result, $\Delta\varphi_n = \Delta\varphi, \forall n \in [1, N]$, because it is modulus 2π. In this context, the carrier phase correction $\Delta\varphi$ is always valid in this scenario, independently the number of multiplexed RF channels in consideration.

By acting on the coupling status of the MRR, the phase response slope in the vicinity of all the resonances can be simultaneously adjusted [84]. A zoomed in image of a resonance as a function of the k is displayed in Fig. 3.17(b). It is important to mention that over-coupled regime is desired since large and linear phase shifts are obtained. A change in the phase slope is always accompanied by a notch power variation. This fact results in power variation of the delayed output signal as a function of the imprinted delay. However, it is not an issue since exactly the same power variation is affecting all the channels and therefore can be easily compensated.

3.4.2.2 Design of a 4-channel TTD line based on MRRs

A proof-of-concept implementation of a TTD line based on an array of SOI MRRs followed by a SCT unit is presented. The generalized system setup is illustrated in Fig. 3.18. It basically consists of N data channels whose information is conveyed on N different RF carriers. The N modulated RF carriers are then transferred on the optical carrier by means of an IM operated in dual-drive configuration, resulting in OSSB modulation. The optical signal at the IM output, which is composed by the optical carrier and N data-modulated RF sidebands, is launched into the $1 \times M$ coupler after amplification. Following, the M coupler outputs are connected in parallel to an on-chip array of M SOI MRRs, each one featuring identical radius but different coupling factor. The k for each MRR is set by properly designing its ring-to-waveguide gap. A $M \times 1$ micro-electro-mechanical system (MEMS) [95] is used for selecting the desired delay. Therefore, M different delay values can be adjusted using a M-bit control signal. At the MEMS output, a SCT unit aiming at inducing the corresponding extra phase shift on the optical carrier is used, in order to meet the TTD condition. The SCT unit is implemented by means of a single over-coupled SOI MRR. By adjusting the electrical power delivered to the micro-heater pads, tunability on the phase response is accomplished by the thermo-optic effects, leading to controllable phase change of the optical carrier. Finally, the optical signal exiting the SCT unit is collected by a HBW PD.

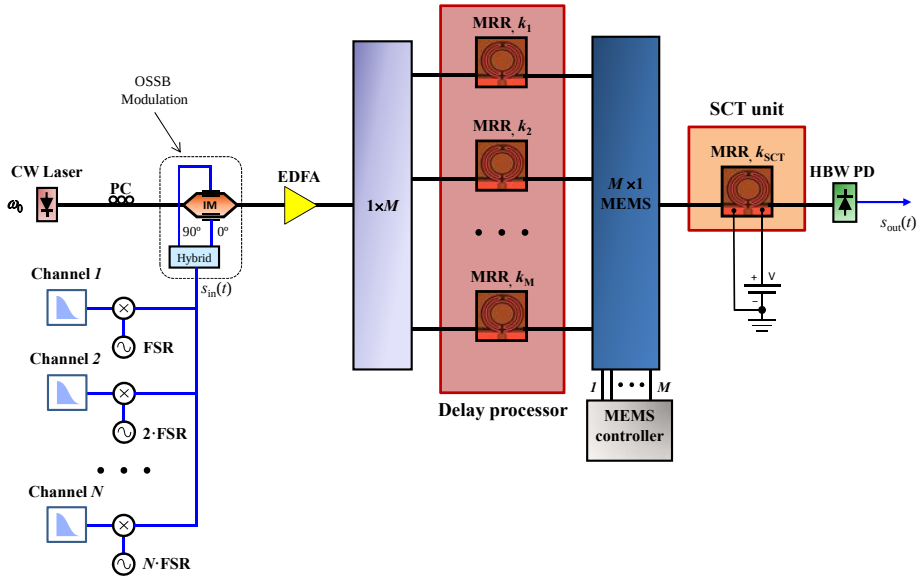

Figure 3.18: Generalized setup for the multi-channel TTD line based on an array MRRs.

In this particular case, 4 data channels operating at 1 Gbps are on-off-keying-modulated (OOK) on a multiplex composed of 12.5 GHz frequency-spaced 4 RF carriers ($N = 4$). Therefore, the aggregate bit data rate is 4 Gbps and the bandwidth spans from 0 to 50 GHz. The array is made up by 4 SOI MRR ($M = 4$), whose k are 0.99, 0.95, 0.9 and 0.85 respectively. The achieved delay can be discretely adjusted between 4 different values. The FSR of all the 4 MRRs must be equal to the RF carriers frequency spacing, i.e., 12.5 GHz. Hence, by assuming a group index value, n_g, of 4.306 and being c_0 the speed of light in the vacuum, the radius for all the 4 MRRs must be

$$R = \frac{c_0}{2\pi n_g FSR} = 887.069\mu\text{m} \tag{3.7}$$

The calculated gain, phase shift and delay features for all the 4 SOI MRRs are shown in Fig. 3.19. The lower k, the larger the power notch. A deeper notch leads to a higher phase slope in the vicinity of the resonance, giving as a result a larger delay. However, the delay bandwidth is directly related to the k. By increasing k, lower but broader delays can be reached. Hence, there exists a trade-off between the maximum delay and the delay bandwidth. The requirement of implementing a delay whose variation is lower than the 1% of the maximum delay value over the signal bandwidth is imposed. This requirement is certainly application-dependent. Table 3.3 shows the maximum delay, τ_{max}, and the spectral bandwidth, Δf for which the condition $\tau \geq \tau_{\max}(1 - 0.01)$ is met as a function of k. Consequently, the delay can be discretely adjusted from 100 to 229 ps.

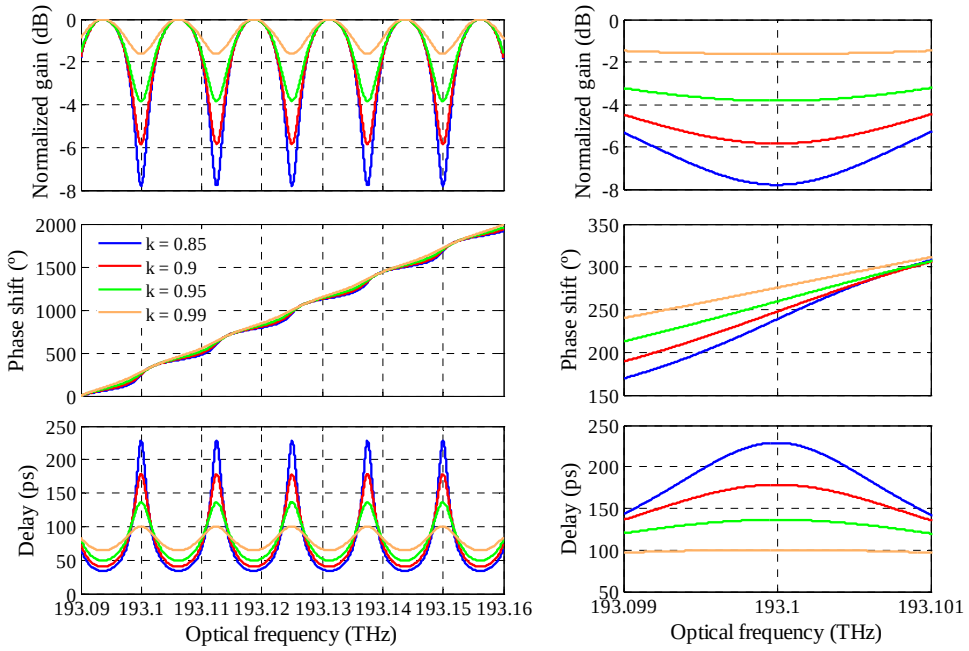

Figure 3.19: Calculated gain, phase shift and delay as a function of k.

k	τ_{max}	Δf
0.85	229 ps	235 MHz
0.9	178.5 ps	333 MHz
0.95	136.3 ps	531 MHz
0.99	100.3 ps	1.17 GHz

Table 3.3: Maximum delay and delay bandwidth as a function of k.

From Tab. 3.3, the delay bandwidth for the MRR featuring $k = 0.85$ limits the data rate of the information channels. According to the Nyquist-Shannon theorem [96] and taking into account that the information is conveyed on the RF carriers via OOK modulation, the maximum distortion-free bit rate is then limited to 235 Mbps. Therefore, this approach cannot support the processing of 1 Gbps data signals, unless the distortion criterion ($\tau \geq \tau_{\max}(1 - 0.01)$) is relaxed or more complex modulation schemes are used.

To overcome this drawback, a second approach is proposed. Now, SOI MRRs featuring the calculated radius in Eq. 3.7 and $k = 0.99$ are used. The generalized system setup is illustrated in Fig. 3.20. It basically consists of the same approach presented in Fig. 3.18 particularized to $N = 4$ and $M = 8$, but the on-chip delay processor is characterized by a new design based on an array of SCISSORs.

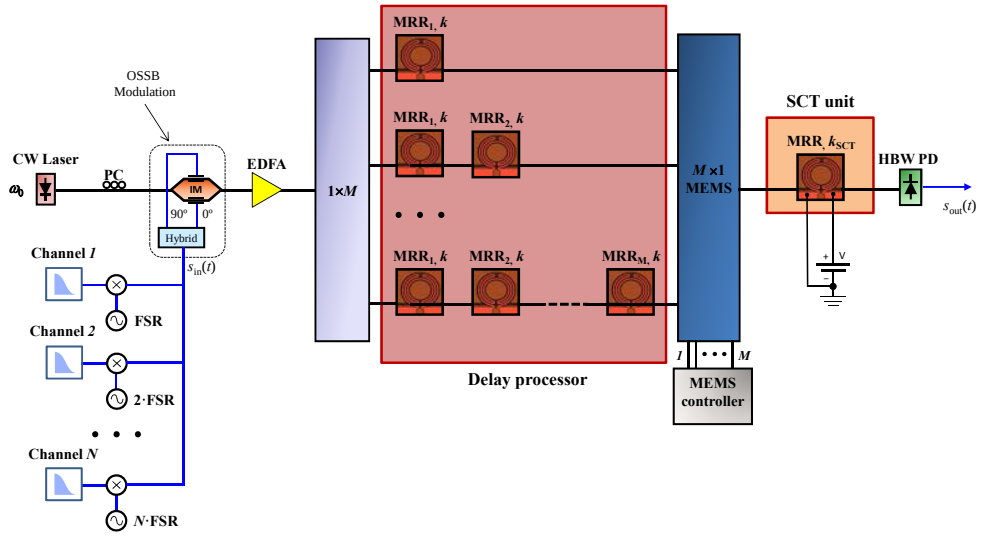

Figure 3.20: Generalized setup for the multi-channel TTD line based on an array of cascaded MRRs.

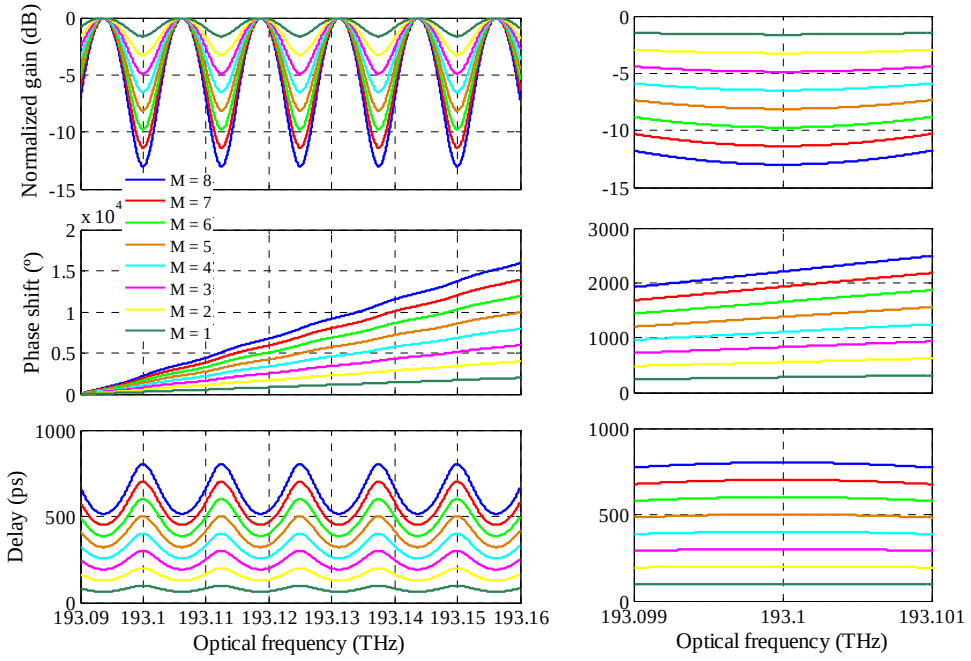

Figure 3.21: Calculated gain, phase shift and delay as a function of the number of cascaded MRRs (M).

Previously, a delay of 100 ps over a bandwidth of 1.17 GHz has been demonstrated by deploying a MRR with $k = 0.99$. The cascade of M identical MRRs results in a reachable delay of M times 100 ps, keeping unaltered the bandwidth on which the condition $\tau \geq \tau_{\max}(1 - 0.01)$ is met. Therefore, the delay can be discretely adjusted from 100 ps to 800 ps with steps of 100 ps by selecting the corresponding line of the array by means of the MEMS. As shown in Fig. 3.21, the optical power penalty affecting each RF carrier varies from 1.6 to 13 dB when sweeping the delay from 100 ps to 800 ps. By cascading M SOI MRRs, the phase slope becomes M times higher than that reached by a single MRR.

Once designed the delay processor, the SCT unit must be accurately implemented in order to achieve TTD operation. For this purpose, a fully tunable 360° phase shifter is required. In particular, a single SOI MRR is used. By placing a resonance in the vicinity of the optical carrier spectral position, the dispersive phase response of the MRR can be exploited to imprint on it the desired phase shift. Aiming at enabling controllable phase shift on the optical carrier, fact which is essential in this approach to achieve TTD operation as shown in Fig. 3.17(a), thermo-optic effects on silicon are used [81]. By changing the voltage applied to the micro-heater pads, the temperature of the SOI-based compound is varied due to power dissipation [97]. Since the group index is strongly dependent on the temperature, the FSR can be adjusted and therefore the resonance spectral positions. For highly confined waveguides, the thermo-optic coefficient in SOI circuits at telecommunications wavelengths is $dn_g/dT = 1.8 \cdot 10^{-4}/°C$ [98, 99].

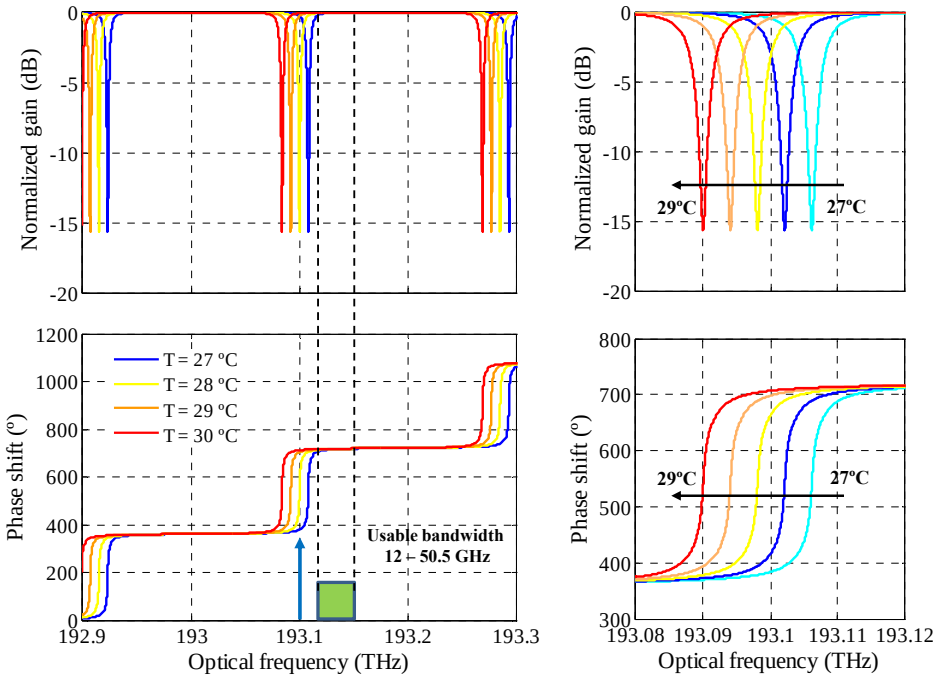

Figure 3.22: Calculated gain and phase shift as a function of the temperature of the SOI compound. Detail of the optical carrier and usable bandwidth.

Together with performing controllable phase-shifting tasks on the optical carrier, the MRR phase feature must be flat at least over the usable bandwidth, i.e., from 12 to 50.5 GHz. A possible solution consists of implementing a MRR featuring a FSR much higher than the usable bandwidth. Moreover, a resonance must be spectrally placed in the vicinity of the optical carrier wavelength, i.e., 193.1 THz. Because of these facts, a SOI MRR featuring a radius of 60 μm is used. At 25°, the measured group index is 4.306 as already shown in Fig. 3.5. Consequently, the FSR is roughly 185 GHz, which is indeed high enough to avoid interference of near resonances on the usable bandwidth. On the other hand, sharp phase response is required since flat amplitude and phase must experience the first data channel placed at 12.5 GHz from the optical carrier. For this purpose, k must be slightly higher than that yielding critical coupling in order to assure a sharp 2π phase shift [84]. Due to this fact, $k = 0.12$ is chosen.

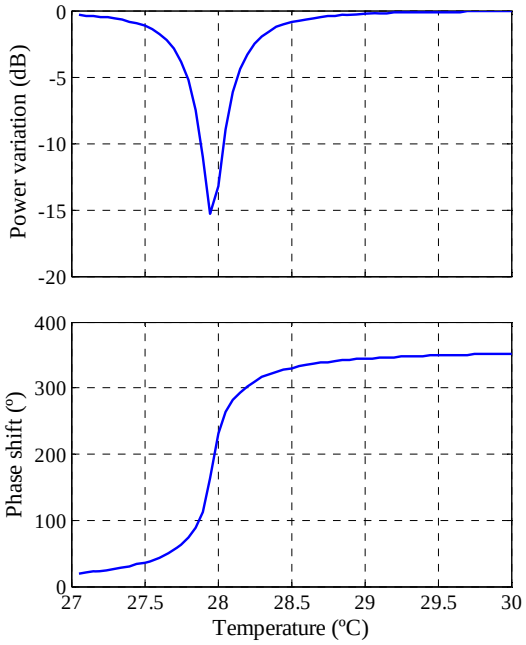

Figure 3.23: Calculated gain and phase shift imprinted on the optical carrier as a function of the temperature of the SOI compound.

The calculated gain and the phase responses as a function of the temperature are shown in Fig. 3.22. When increasing the temperature from 27 to 30°C, a red-shift of the resonance position by more than 24 GHz occurs. At frequencies belonging to the usable bandwidth, both the gain and phase features show a flat behavior. The resonance wavelength change results in a continuously controllable phase shift on the optical carrier of 332° when rising up the temperature as displayed in Fig. 3.23. The power variation of the optical carrier varies by more than 15 dB within the temperature range as also shown in Fig. 3.23. Depending on the application, this fact can be a problem. A possible solution consists of using a SOI dual-MRRs (DMRRs) properly designed as already reported in [83]. By deploying the DMRRs

based configuration, the power variation can be substantially lowered while yielding large phase shift [83].

After separately designing the delay processor and the SCT unit of the approach illustrated in Fig. 3.20, the performance of the complete TTD line is evaluated. Firstly, the phase offset to be induced on the optical carrier ($\Delta\varphi$) by the SCT unit as a function of the synthesized delay must be obtained. For a certain delay, the phase offset on the optical carrier is independent on the number of multiplexed RF carriers, as already demonstrated in Sec. 3.4.2.1. The phase transfer function centred at frequencies comprising the optical carrier and the first data-modulated RF carrier is displayed in Fig. 3.24 as a function of M, that is, the delay. Besides, the linear fitting carried out on the usable bandwidth of the lowest frequency RF carrier extended towards the optical carrier spectral position is also depicted with respect to M. These results show that a phase correction on the optical carrier must be accomplished in order to meet the TTD condition, i.e., linear phase shift with the frequency.

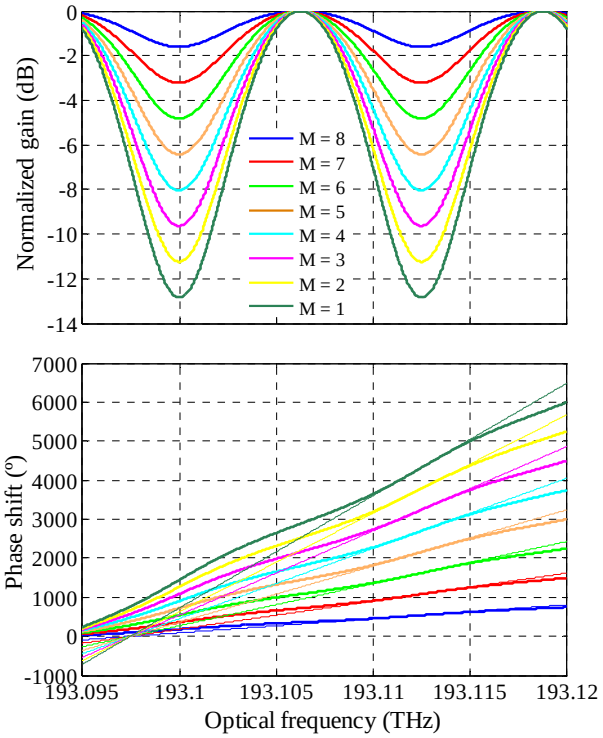

Figure 3.24: Calculated gain and phase shift responses as a function of the M. Linear fitting to meet the TTD condition as a function of the M.

A zoom of the spectral region in the vicinity of the optical carrier position is displayed in Fig. 3.25(a). If attention is paid at 193.1 THz, the larger the delay τ, the larger the phase offset $\Delta\varphi$ is, with the aim of achieving equivalent linear phase behavior. The phase offset values expressed in modulus 2π as a function of the delay are depicted in Fig. 3.25(b). It is remarkable that the phase offset as a function

of the delay features a periodical behavior with a period of 400 ps. This periodical function can be modelled as $\Delta\varphi_M = -M \cdot \pi/2$. Consequently, the temperature is also a periodical function with the same period. The temperature has to be properly set in the range from 27 to 28.2°C approximately.

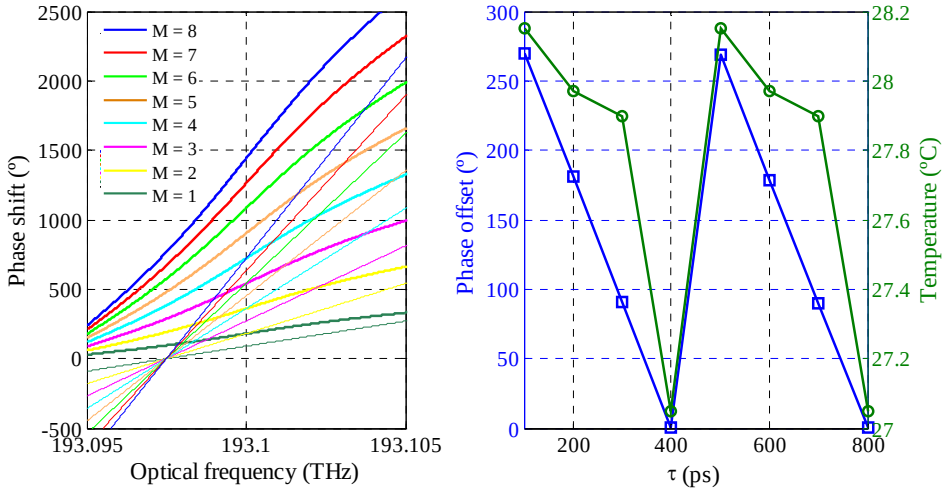

(a) (b)

Figure 3.25: (a) Detail of the phase response and the linear fitting in the vicinity of the optical carrier wavelength as a function of the M. (b) Phase offset and the corresponding temperature of the SOI compound as a function of the delay.

The detected RF power spectrum as a function of M is displayed in Fig. 3.26. At the end, the final average power level depends on M, as well as the phase offset induced on the optical carrier. When selecting the array lines comprising 2 or 6 cascaded MRRs, the SCT unit adds the maximum attenuation since a phase offset of 180° is required, corresponding to the notch minimum value (see Fig. 3.23). The delay of the detected signal as a function of the RF frequency is also depicted in Fig. 3.26. As expected, controllable delays from 100 ps to 800 ps can be adjusted depending on the array line selected by the MEMS. Out-of-band delays, more in particular at low frequencies, exhibit irregular behavior due to the SCT MRR transfer function used for achieving the desired optical carrier phase offset. However, the condition $\tau \geq \tau_{\max}(1 - 0.01)$ is met along the channel bandwidth centered at each RF carrier, resulting in the TTD operation.

From the results shown in Fig. 3.26, a power penalty of more than 64 dB occurs at each channel when changing the delay from 100 ps to 800 ps. Despite the large attenuation affecting to large delays, this fact is not a problem. The proposed structure equally attenuates all the data channels, so it can be easily compensated by both optical or electrical amplification before or after the detection respectively. An accurate solution consists of using automatic gain control (AGC) systems, which automatically adjusts the gain depending on its input power.

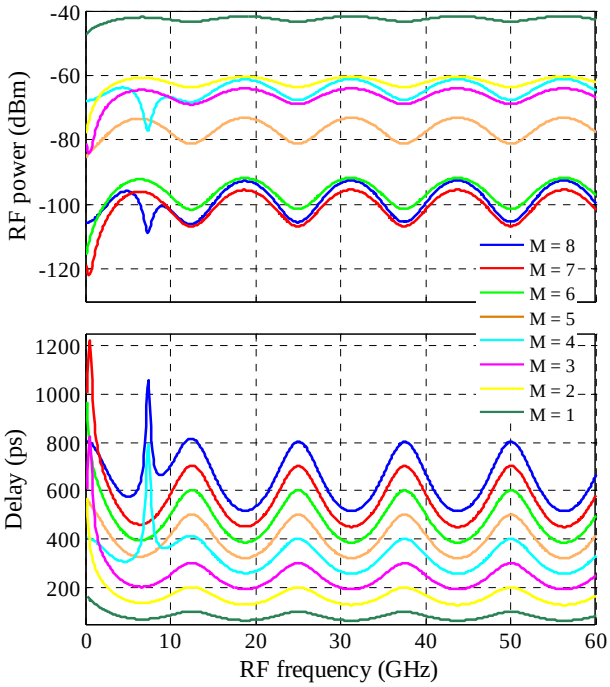

Figure 3.26: Calculated RF power spectra and delays as a function of the M.

3.5 Summary and conclusions

In this chapter, SFL effects in SOI based MRRs have been observed. These effects, which allows for controllable group index, have been exploited for the implementation of several functionalities within the field of photonic RF signal processing.

Firstly, a novel tunable complex-valued multi-tap microwave photonic filter based on a single SOI MRR has been proposed and demonstrated. Filter response tunability without changing the FSR can be accomplished by properly setting the emission wavelength of N tunable lasers. The trade-off between the filter selectivity, given by the number of samples N, and the degree of tunability has been studied in-depth. Fractional tuning greater than 77% has been obtained when implementing two taps, whereas in the case of four taps it has been above 24%. These fractional tunings can be enhanced by using cascaded MRRs. The performance in terms of SLL can be improved by properly engineering window based samples. Different window taps schemes have been evaluated. In particular, the Hamming window with $B = 0.8$ has yielded the maximum SLL levels, up to 23 dB.

Secondly, the unique dispersion features of SOI MRRs have been exploited for designing a multi-channel TTD line. After introducing a new concept named as E-SCT, which benefits from resonant-type structures aiming at partially overcoming the limitation in terms of small delay bandwidth, a novel approach has been proposed. It is mainly based on an array of cascaded SOI MRRs in combination with the SCT

unit. Discretely controllable delays from 100 ps to 800 ps with step of 100 ps has been achieved on a multiplex based signal comprising 4 data-modulated RF carriers. Simultaneous delay over aggregate instantaneous bandwidth exceeding 4.5 GHz has been reached. Furthermore, the inherent structure of the proposed approach allows for flexible designs in terms of maximum delay, RF channel spectral separation and number of channels.

The objectives of this chapter have been fulfilled and recognized by the community in the following international publications:

1. **J. Lloret**, J. Sancho, M. Pu, I. Gasulla, K. Yvind, S. Sales, and J. Capmany, "Tunable complex-valued multi-tap microwave photonic filter based on single silicon-on-insulator microring resonator", Optics Express, vol. 19, no. 13, pp. 12402-12407, 2011.

2. **J. Lloret**, J. Sancho, I. Gasulla, S. Sales, and J. Capmany, "Complex-coefficient microwave photonic tunable filter using slow light silicon-on-insulator-based microring resonator", in IEEE Topical Meeting Microwave Photonics (MWP), Singapore (Singapore),paper 2167, 2011.

Chapter 4

SFL effects in III-V/SOI microdisks resonators

4.1 Introduction

As shown in the preceding chapter, SOI has arisen as the preferred technology platform for implementing passive photonic functionalities over the past years. Features such as the transparency of silicon at telecom wavelengths, the high refractive index contrast, which leads to high-density integration, or the CMOS compatibility offer the possibility of device fabrication in the sub-micron scale [64, 65, 100]. However, a major obstacle for large-scale silicon-based electronic-photonic integration is the indirect band gap of silicon. Although light emission [73,74], detection [69,101] and amplification [75,76] functionalities implemented on silicon have already been demonstrated, in practice the low-efficiency hampers the assembly of high-performance active devices. Therefore, silicon-based integrated optics has little prospect for the implementation of active devices despite of the relatively low cost compared to other technologies.

A very promising solution for implementing active functionalities using SOI platforms consists of bonding on a direct band gap material, especially those belonging to the III-V group. Researchers from *University of California* in Santa Barbara demonstrated in 2005, for the first time, a hybrid evanescent laser fabricated with AlGaInAS offset quantum wells on a silicon-based waveguide [102]. During the next years, impressive development on this device has been accomplished up to now. In particular, accurate designs for all-optical silicon-based integrated transmitters [103], as well as DFB-based structures [104] have been carried out. Besides, advanced architectures involving the integration of both a photodetector and a preamplifier have been reported [77].

On the other hand, in 2006, researchers from *imec* (Belgium) successfully demonstrated laser emission and photodetection using an InP/InGaAsP thin film epitaxial layer bonded onto a SOI waveguide circuit [105]. A short while later, a new device composed of an InP-based MDR heterogeneously integrated on and coupled to a nanophotonic SOI waveguide was developed, in the search of a multi-purpose

device. The technology evolved by *imec* enabled the fabrication of ultra-compact cavities with low optical loss, together with sufficient confinement factor [106, 107]. This fact opened a wide range of possibilities for implementing different applications. Among them, tunable single-wavelength [108] and multi-wavelength [109] lasers, detectors [105], optical gating [110], electro-optical switchers [111], wavelength converters [112, 113], optical couplers [114, 115], all-optical flip-flops [116] and electro-optical amplitude modulators [117] have already been reported. However, to the best of our knowledge, no efforts have been accomplished so far using such a device within the field of MWP.

In this chapter, the unique features of InP/SOI MDR have been exploited with the aim of implementing signal processing of RF and digital signals. Firstly, the device structure and the fabrication process of III-V-on-silicon MDRs will be detailed. Next, a fully tunable MWP phase shifter based on a single MDR will be presented. The performance will be evaluated through experimental and numerical results. Then, the phase shifter will be used as a key element in a notch-type filtering scheme enabling the implementation of complex-valued coefficients. This fact results in tunable filtering responses. Finally, an electro-optical phase modulator based on a MDR will be demonstrated. The advantages and drawbacks of this approach compared with other existing phase modulators will be described.

4.2 Device structure and fabrication

The device is composed of an InP/InGaAsP microdisk cavity which is bonded on top of a SOI waveguide circuit. Vertical grating couplers in combination with tapered ports are used to input and output light to the MDR, as illustrated in Fig. 4.1(a). The schematic drawing of the heterogeneous MDR final structure consisting of the InP cavity, the SOI waveguide, the bottom and top metal contacts, the tunnel junction and the active layer, is shown in Fig. 4.1(b).

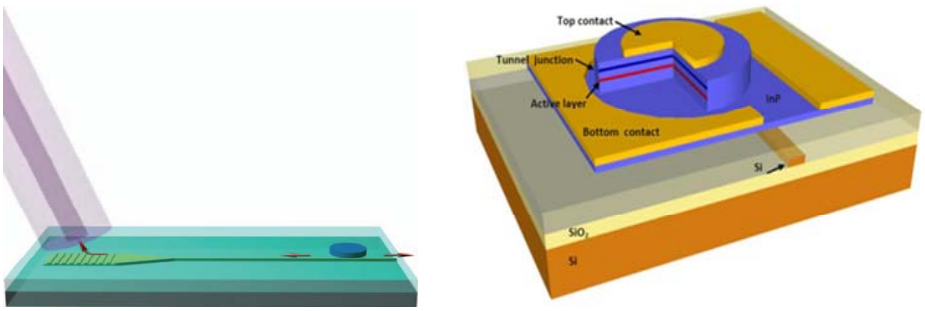

(a) (b)

Figure 4.1: (a) Schematic structure of the whole circuit (the vertical grating coupler is depicted only on one end of the SOI waveguide) [116]. (b) Schematic drawing of the heterogeneous MDR structure [111].

The MDR structure shown above is as a result of the processing cycle illustrated in Fig. 4.2(a) [118]. First, a SOI circuit containing a 750-nm-wide and 220-nm-high silicon strip waveguide was etched on a 1-μm-thick SiO_2-based buffer layer. Next, the SOI wafer was cleaned using $3H_2SO_4$:$1H_2O_2$ and $1NH_3$:$4H_2O_2$:$20H_2O$ to remove the hydrocarbon contamination and the particles that were pinned to the surface, respectively [105]. On the other hand, the epitaxial growth of the InP wafer was accomplished. The heterostructure was grown at 490 ˚C using solid source molecular beam epitaxy (SSMBE) on a two inch InP wafer. The layer structure is schematically shown in Fig. 4.1(b). An InGaAs sacrificial etch-stop layer was grown first. The structure starting from the bottom layer consists of a 95-nm-thick $5{\cdot}10^{18}$ cm^3 Si-doped InP bottom contact layer, a 120-nm-thick InGaAsP quaternary emitting at 1.2 μm (Q1.2) $1{\cdot}10^{18}$ cm^3 Si doped n-layer, a 25 nm Q1.2 spacer layer, three 6-nm-thick compressively strained InAsP quantum wells (QWs) embedded in 15 nm Q1.2 barriers, a 25 nm Q1.2 spacer layer and a 135-nm-thick $5{\cdot}10^{17}$ cm^3 to $1{\cdot}10^{18}$ cm^3 Be doped InP layer. A p+/n+ tunnel junction in combination with a n+ contact layer were used to avoid the large absorption due to the proximity between the top contact layer and the upper QW [111]. Then, the heterostructure was molecularly bonded onto the SOI wafer. After that, the InGaAs sacrificial etch-stop layer was removed by grinding and wet chemical etching. Subsequently, the disk was realized in the heterostructure using contact lithography and inductively coupled plasma (ICP) etching until the bottom contact layer was reached. Finally, the contacts were deposited using evaporation [118].

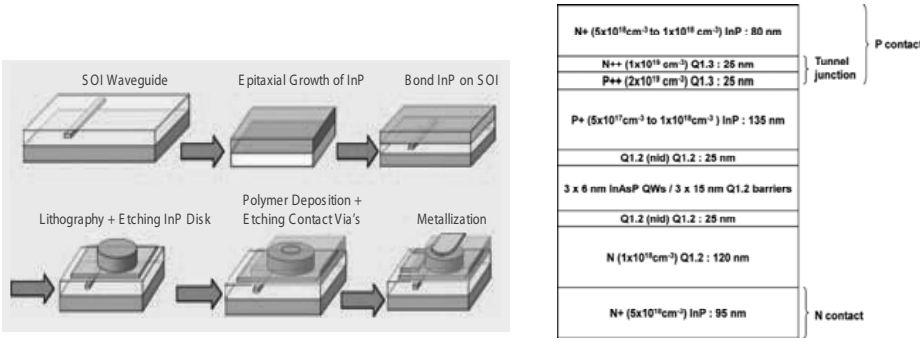

(a) (b)

Figure 4.2: (a) Overview of the fabrication process [118]. (b) Layer structure [111].

A top-view micrograph fabricated devices showing the MDR cavities, the metal contacts and the vertical grating couplers is displayed in Fig. 4.3(a). In Fig. 4.3(b), a scanning electron microscope picture of a MDR cross-section is shown. The top and bottom metal contacts, together with the disk and the SOI waveguide can be discerned.

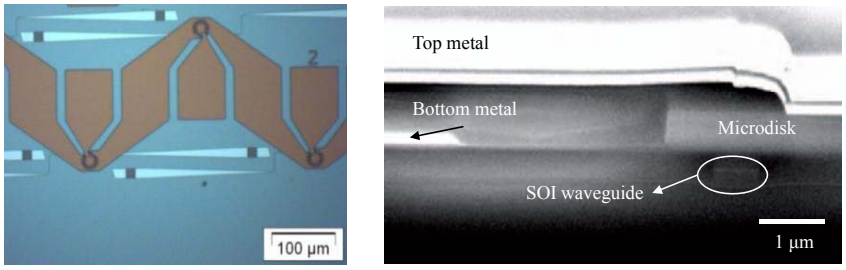

(a) (b)

Figure 4.3: (a) Top-view micrograph of fabricated devices. (b) SEM image of the MDR cross-section [118].

4.3 Basic properties of III-V/SOI MDRs

The operating basics of the III-V/SOI MDR lies in the well-known semiconductor theory energy model based on electronic bands [119]. By applying electrical pumping in the metal contacts of the structure, the carriers are concentrated and forced to recombine in the active layer, where the energy gap reaches its lower value. From the recombination process, an amount of energy is released. This energy is used for creating a photon whose oscillation frequency is proportional to the Plank's constant according to the quantum theory.

The light resulting from the recombination process is guided through the cavity. The propagation is governed by the so-called whispering-gallery modes (WGMs), which are confined to the edges of the MDR and only occur at particular resonance wavelengths for a given MDR size. Due to the structure topology, the light propagates in the clockwise (CW) and counter-clockwise (CCW). Thereby, a pair of counter-propagating longitudinal modes compete inside the cavity [116]. Depending on the current injected into the MDR cavity, both the CCW and the CW propagation modes can be altered, giving as a result different operating regimes. When injecting low current, *bidirectional continuous wave* operating regime is forced, in which the output power associated to both modes is the same. If the current is increased, a second regime called *bidirectional with alternate oscillations* is reached. In this regime, the output power for the counter-propagating modes is characterized by anti-phase harmonic sinusoidal oscillations; i.e. when the CCW mode has a power maximum, CW has a minimum. Finally, by injecting large enough current, as well as sufficiently small coupling between the CW and CCW modes, a third regime called *unidirectional* occurs. This way one of the two modes is roughly suppressed while the other keeps lasing [116].

However, by injecting light with the proper emission wavelength and power into the optical left port, the CCW WGMs inside the cavity locks the injection signal, giving as a result that optical power is directed only towards the output right port, i.e., forcing *unidirectional* regime. Likewise, opposite behavior is reached when injecting light into the optical port at the right.

4.4 Applications

In this section, InP/SOI-based MDRs have been used in the implementation of several applications. In particular, the MDR has been exploited for developing signal processing tasks. First, a tunable and broadband photonic phase shifter operating in the microwave and mm-wave band is demonstrated. Then, the photonic RF phase shifter is used as a key element in MWP filtering schemes. Finally, a MDR-based electro-optical phase modulator is presented and its performance evaluated.

4.4.1 MWP phase shifter

4.4.1.1 Principle of operation

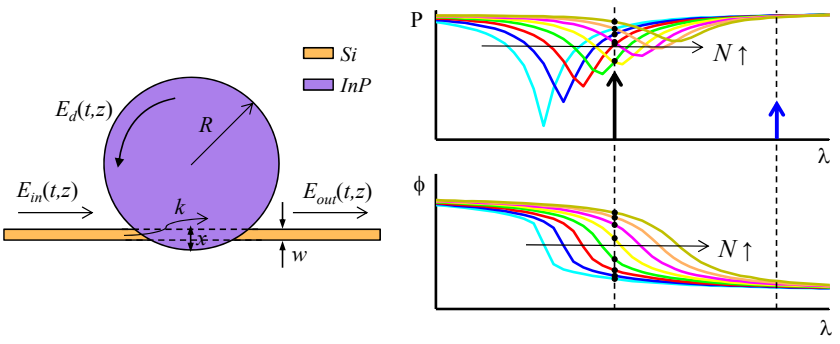

(a) (b)

Figure 4.4: (a) Schematic drawing of the simplified MDR structure. (b) Principle of operation of the MDR-based MWP phase shifter when using OSSB at its input.

A schematic drawing of the simplified device structure is sketched in Fig. 4.4(a). It basically consists of an InP-based MDR cavity with radius R, which is bonded onto a Si waveguide with overlap x, featuring a power coupling factor k. $E_{in}(t,z)$ and $E_{out}(t,z)$ correspond to the input and output electrical fields respectively, whereas $E_d(t,z)$ is the total electrical field propagating inside the cavity. Fig. 4.4(b) shows the principle of operation of the InP/SOI MDR based MWP phase shifter. As already mentioned, the propagation in such a structure is based on WGMs, which are confined to the edges of the MDR resulting in a resonant-type response. If an OSSB modulation signal is launched at the input, therefore forcing *unidirectional* regime, and accurately placed in the vicinity of a resonance, the optical carrier and the modulation sideband will experience different phase changes according to their spectral positions in the MDR phase transfer function. By acting on the carrier injection into the MDR, the effective index can be modified and consequently the spectral positions of the resonances can be shifted. This way the difference between the optical phase shifts experienced by the optical carrier and the sideband can be changed. It must be noticed that both the input optical power and the injection current can be used as control mechanisms for the carrier density (N) thus allowing for controllable

tuning of the phase shift difference. Upon beating at the optical detector, this phase shift difference is impressed onto the resulting microwave carrier.

The technique of combining OSSB modulation with optical filtering to implement complex-valued filters was originally proposed in [87], where phase shifters based on FBG instead of InP/SOI MDRs were considered.

4.4.1.2 Modelling

Hereafter, a comprehensive semi-analytical analysis aiming at predicting the device behaviour is derived. Previously, the principle of operation of the MWP phase shifter based on a single MDR in combination with OSSB has been explained. However, to avoid loss of generality, a double-sideband (DSB) signal comprised of an optical carrier at optical frequency ω_0 and two sidebands at $\omega_0 \pm \Omega$ is considered at the MDR input.

$$E_{in}(t,z) = \left[\begin{array}{l} |E_0(z)|\, e^{j\theta_0} + |E_{-1}(z)|\, e^{j(\Omega t - \theta_{-1})} + \\ \\ |E_{+1}(z)|\, e^{-j(\Omega t - \theta_{+1})} \end{array} \right] e^{-j(\omega_0 t - k_0 z)}, \tag{4.1}$$

where k_0 is the propagation constant and Ω is the modulation frequency. $|E_0|$ and θ_0 correspond to the amplitude modulus and optical phase of the optical carrier, whereas $|E_{+1}|$, $|E_{-1}|$, θ_{+1} and θ_{-1} are those corresponding to both modulation sidebands, respectively. Eq. 4.1 can be particularized for OSSB modulation by assuming $|E_{+1}| = 0$ or $|E_{-1}| = 0$. The optical signal, E_{in}, is as a result of impressing a RF tone at frequency Ω on the optical carrier by means of an IM. Harmonic distortion resulting from the modulating process is neglected because small-signal modulation, as well as the assumption that the IM is biased in the quadrature point are considered.

The output signal, E_{out}, can be expressed as the sum of infinite contributions each one propagating a certain number of roundtrips around the MDR:

$$E_{out}(t,z) = E_{in}(t,z)\, T - E_{in}(t,z)\, k^2\, |H(t,z)|\, e^{j\phi(t,z)} \sum_{r=0}^{\infty} \left(T\, |H(t,z)|\, e^{j\phi(t,z)} \right)^r \tag{4.2}$$

where T corresponds to the transmission coefficient, which is defined in terms of the power coupling factor as $T = (1-k)^{1/2}$. The terms $|H(t,z)|$ and $\phi(t,z)$ are the amplitude modulus and the phase of the resonant cavity's transfer function, $H(t,z) = |H(t,z)|\, e^{j\phi(t,z)}$, respectively. It must be noticed that H is time- and spatial-dependent. However, moderate input power E_{in} is inserted into the MDR. This way a linear behaviour in the semiconductor can be considered. Consequently, time-invariant gain will be assumed, so H is found to be the same in all the contributions appearing in Eq. 4.2. The spatial dependence is taken into account in the analysis, nevertheless, it is omitted in the notation for simplicity hereinafter.

If the condition $T\,|H| < 1$ is fulfilled, convergence is reached. This means that the device must be operated below threshold to avoid lasing. Therefore, Eq. 4.2 can

be expressed in terms of a geometric progression. Hence, the optical complex field at the MDR output can be written as

$$E_{out} = \left(\frac{T - |H| e^{j\phi}}{1 - T |H| e^{j\phi}} \right) E_{in}. \tag{4.3}$$

The derivation of H involves the assessment of the propagation equations for all the three optical waves depending on E_{in}. The propagation equations are formulated in the context of a wave mixing description. Wave mixing in active semiconductor materials has contributions from carrier density depletion, carrier heating, spectral hole burning, two-photon absorption and Kerr effects [120]. However, for modulation frequencies up to some tens of GHz, the dominating mechanism mediating the wave mixing is the carrier density pulsation [121]. In this way, the ultrafast effects as well as the gain saturation due to amplified emission noise are neglected, which are reasonable approximations in the regime of moderate input optical power. Consequently, the wave mixing problem can be simplified by accounting just for the interactions between the three optical waves as [41]

$$\frac{\partial E_{d,0}}{\partial z} = \gamma_0 E_{d,0}, \tag{4.4}$$

$$\frac{\partial E_{d,-1}}{\partial z} = \gamma_0 E_{d,-1} + \varepsilon_{-1} \left\{ |E_{d,0}|^2 E_{d,-1} + {E_{d,0}}^2 E^*_{d,+1} e^{j\Delta k z} \right\}, \tag{4.5}$$

$$\frac{\partial E_{d,+1}}{\partial z} = \gamma_0 E_{d,+1} + \varepsilon_{+1} \left\{ |E_{d,0}|^2 E_{d,+1} + {E_{d,0}}^2 E^*_{d,-1} e^{j\Delta k z} \right\}, \tag{4.6}$$

where γ_0 and $\varepsilon_{\pm 1}$ are the complex first- and third-order susceptibilities, respectively. Δk is the phase-mismatching factor induced by the background and the waveguide dispersions. $\Delta k = 0$ is a good approximation when considering modulating frequencies up to several tens of GHz. $E_{d,0}$, $E_{d,+1}$ and $E_{d,-1}$ refer to the optical waves (carrier and both sidebands) already travelling inside the disk cavity for all the three spectral lines.

$$\gamma_0 = \frac{1}{2} \left[\frac{\Gamma g_0}{1 + S} (1 - j\alpha) - a_{\text{int}} \right], \tag{4.7}$$

$$\varepsilon_{\mp 1} = -\frac{1}{2} \frac{\Gamma g_0}{(1 + S) P_{sat}} \frac{1 - j\alpha}{1 + S \pm j\Omega\tau_s}, \tag{4.8}$$

being Γ the confinement factor, α the linewidth enhancement factor, τ_s the carrier lifetime and a_{int} the internal waveguide loss. The normalized CW optical power, S, the saturation power, P_{sat}, and the small-signal gain g_0 are defined as

$$S = \frac{|E_{d,0}|^2 + |E_{d,+1}|^2 + |E_{d,-1}|^2}{P_{sat}}, \tag{4.9}$$

$$P_{sat} = \frac{A_c \hbar \omega_0}{a \tau_s}, \tag{4.10}$$

$$g_0 = a\,(N - N_t)\,, \tag{4.11}$$

where A_c, a, N and N_t are the effective cross section, the differential gain coefficient, the carrier density and the carrier density at transparency, respectively.

By solving the Eqs. 4.6, 4.7, 4.8 analogously to [41], the electrical field for all the three optical waves after one roundtrip can be expressed (see Appendix A) as

$$E_{d,0}\,(z = L) = E_{d,0}\,(z = 0)\,e^{F(L)}, \tag{4.12}$$

$$E^*_{d,-1}\,(z = L) = e^{F(L)^*}\left\{\frac{1}{2}\left(-v\,(0) + u\,(0)\left[j\alpha\left(e^{G(L)} - 1\right) + e^{G(L)}\right]\right)\right\}, \tag{4.13}$$

$$E_{d,+1}\,(z = L) = e^{F(L)}\left\{\frac{1}{2}\left(v\,(0) + u\,(0)\left[j\alpha\left(1 - e^{G(L)}\right) + e^{G(L)}\right]\right)\right\}, \tag{4.14}$$

with

$$u\,(0) = E_{d,+1}\,(z = 0)\,e^{-F(L)} + E^*_{d,-1}\,(z = 0)\,e^{-F(L)^*}, \tag{4.15}$$

$$v\,(0) = E_{d,+1}\,(z = 0)\,e^{-F(L)} - E^*_{d,-1}\,(z = 0)\,e^{-F(L)^*}, \tag{4.16}$$

being the input conditions. $F(L)$ and $G(L)$ stand for the common and the gain grating related complex amplification factors respectively, for the device length $L = 2\pi R$ [41].

$$F\,(L) = \frac{1}{2\,(\Gamma g_0 - a_{\text{int}})}\left[\begin{array}{l} j\alpha\Gamma g_0 \ln\left(\frac{a_{\text{int}}(S(z=L)+1)-\Gamma g_0}{a_{\text{int}}(S(z=0)+1)-\Gamma g_0}\right) \\ \\ +\,(\Gamma g_0 - j\alpha\Gamma g_0 + a_{\text{int}}) \ln\left(\frac{S(z=L)}{S(z=0)}\right) \end{array}\right], \tag{4.17}$$

$$G\,(L) = A + jB, \tag{4.18}$$

where the parameters A and B are calculated as follows (see details in Appendix A):

$$A = \frac{(\Gamma g_0)^2}{a^2_{\text{int}}(\Omega\tau_s)^2 + (\Gamma g_0)^2}\left\{\begin{array}{l} \ln\left(\frac{\frac{a_{\text{int}}}{\Gamma g_0}(S(z=L)+1)-1}{\frac{a_{\text{int}}}{\Gamma g_0}(S(z=0)+1)-1}\right) - \\ \\ \frac{1}{2}\ln\left(\frac{(S(z=L)+1)^2+(\Gamma g_0)^2}{(S(z=0)+1)^2+(\Gamma g_0)^2}\right) + \\ \\ \frac{a_{\text{int}}\Omega\tau_s}{\Gamma g_0}\left[\begin{array}{l} \arctan\left(\frac{S(z=L)+1}{\Omega\tau_s}\right) - \\ \\ \arctan\left(\frac{S(z=0)+1}{\Omega\tau_s}\right) \end{array}\right] \end{array}\right\}, \tag{4.19}$$

$$B = \frac{(\Gamma g_0)^2}{a_{\text{int}}^2(\Omega\tau_s)^2 + (\Gamma g_0)^2} \left\{ \begin{array}{l} \ln\left(\frac{\frac{a_{\text{int}}}{\Gamma g_0}(S(z=L)+1)-1}{\frac{a_{\text{int}}}{\Gamma g_0}(S(z=0)+1)-1}\right) - \\ \\ \arctan\left(\frac{S(z=L)+1}{\Omega\tau_s}\right) - \\ \\ \frac{1}{2}\frac{a_{\text{int}}\Omega\tau_s}{\Gamma g_0}\ln\left(\frac{(S(z=L)+1)^2+(\Gamma g_0)^2}{(S(z=0)+1)^2+(\Gamma g_0)^2}\right) + \\ \\ \arctan\left(\frac{S(z=0)+1}{\Omega\tau_s}\right) \end{array} \right\}. \tag{4.20}$$

By referring Eqs. 4.12, 4.13, 4.14 to the electrical field at the input, H can be derived for all the three optical waves as

$$H_0 = e^{F(L)}, \tag{4.21}$$

$$H_{-1}^* = \frac{1}{2}\left\{ \begin{array}{l} 1 + \frac{E_{d,+1}(z=0)}{E_{d,-1}^*(z=0)} e^{-F(L)} e^{F(L)^*} \left[j\alpha\left(e^{G(L)}-1\right) + e^{G(L)} - 1\right] + \\ \\ j\alpha\left(e^{G(L)}-1\right) + e^{G(L)} \end{array} \right\}, \tag{4.22}$$

$$H_{+1} = \frac{1}{2}\left\{ \begin{array}{l} 1 + \frac{E_{d,-1}^*(z=0)}{E_{d,+1}(z=0)} e^{F(L)} e^{-F(L)^*} \left[j\alpha\left(1-e^{G(L)}\right) + e^{G(L)} - 1\right] + \\ \\ j\alpha\left(1-e^{G(L)}\right) + e^{G(L)} \end{array} \right\}. \tag{4.23}$$

Equations 4.21, 4.22, 4.23 have to be inserted into Eq. 4.3 to obtain the output complex electrical field for each optical wave, $E_{out,0}$, $E_{out,+1}$ and $E_{out,-1}$, respectively. After photodetection, the current beating term oscillating at Ω is

$$i_\Omega(t) \propto 2\Re\left\{ \begin{array}{l} |E_{out,0}|\,|E_{out,-1}|\cos\left(\Omega t + (\theta_{out,0} - \theta_{out,-1})\right) + \\ \\ |E_{out,0}|\,|E_{out,+1}|\cos\left(\Omega t + (\theta_{out,+1} - \theta_{out,0})\right) \end{array} \right\}, \tag{4.24}$$

where t refers to time, $\Re$ is the detector responsivity and $\theta_{out,i} = arg(E_{out,i})$, for $i = -1{,}0$ or 1.

Finally, the electrical power and the phase shift of the microwave output signal is calculated as

$$P_\Omega = |i_\Omega|^2 Z_0, \tag{4.25}$$

$$\Delta\varphi = \arg(i_\Omega) - \arg(i_\Omega)|_{ref}, \tag{4.26}$$

where Z_0 is the input impedance of the detector. The phase shift is stated relative to a reference, which is defined at the minimum carrier density. In this particular case, $|E_{+1}| = 0$ because OSSB is inserted into the MDR. As one can see, numerical calculation is only required to obtain the electrical field propagating through the MDR as a function of the length unit z. The rest of the modeling is based on analytical description.

4.4.1.3 Numerical and experimental results

In this section, numerical and experimental results of the MDR-based MWP phase shifter are presented. First, a complete device characterization is accomplished. Second, both the amplitude and phase responses for the RF photonic phase shifter are shown, as well as a performance study.

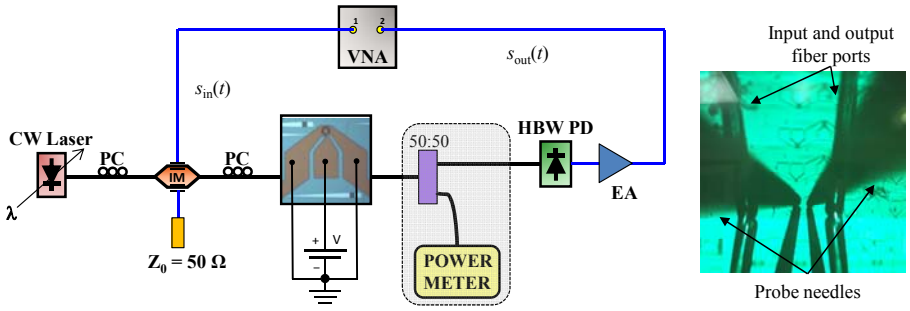

(a) (b)

Figure 4.5: (a) Experimental setup used for characterization purposes. (b) Picture showing a detail of the MDR with the input and output optical fiber ports and the probe needles.

Figure 4.5(a) sketches the experimental setup assembled in order to characterize the MDR transfer function. Firstly, the gain feature over a huge wavelength range was obtained. For this purpose, a CW tunable laser generating a weak spectral line of 9-dBm-power was used. The emission wavelength was swept from 1530 to 1610 nm. In this case, no modulating signal fed the IM, which was set in single-drive configuration by terminating one electrical input port with an impedance of 50 Ω. The 1-dBm-power optical carrier at the output of the IM was sent into the MDR. The 9-μm-diameter MDR was integrated on top of a SOI waveguide circuit containing a 750-nm-wide and 220-nm-high silicon strip waveguide using molecular bonding. The disk-to-waveguide gap and offset fix the coupling factor [107], which in this case was 6%. The total device area, including both the input and output vertical grating couplers was around 0.1 mm^2. A voltage tunable source was connected to the metal contacts with the aim of controlling the carrier injection into the cavity. Polarization controllers were inserted at both the modulator and the MDR inputs to avoid power penalty derived from polarization mismatching. Finally, the optical average power of the signal exiting the MDR was measured by means of a power meter.

A detail of the on-chip MDR showing the input and output optical fiber ports, as well as the probe needles contacting the metals is displayed in Fig. 4.5(b). The angle formed by the fiber ports with the vertical was 10°. Just two probe needles were used due to space constraints, since both ground contacts are shorted. However, the usage of three probe needles usually results in lower input impedance and, consequently, in lower power consumption.

Symbol	Definition	Value
R	MDR radius	4.5 μm
k	Power coupling factor	6 %
Z_0	Detector input impedance	50 Ω
τ_s	Carrier lifetime	90 ps
a	Differential gain	$0.5{\cdot}10^{-20}$ m^2
α	Linewidth enhancement factor	6
a_{int}	Internal loss	4400 m^{-1}
N_t	Carrier density at transparency	$0.8{\cdot}10^{-24}$ m^{-3}
Γ	Confinement factor	0.4
P_{sat}	Saturation power	3 dBm

Table 4.1: Main parameters used for numerical calculations.

Figure 4.6(a) displays the gain and phase responses of the MDR as a function of the injection current. These results have been obtained by using the semi-analytical model presented in the previous section. The values of the main parameters used for the numerical calculations are given in Tab. 5.1. Under bias-free conditions the effective index is found to be 3.474, which corresponds to a FSR of approximately 24.45 nm. The gain parabolic profile is as a consequence of the input and output vertical grating couplers efficiency with the wavelength. This fact was also introduced in the modelling. The notch-type transfer function can be progressively tuned by acting on the carrier density in the MDR cavity. In this case, the tuning mechanism is based on changing the injection current.

The results for the gain response depicted in 4.6(a) are in good agreement with those shown in Fig 4.6(b), which are experimentally obtained. The gain has been obtained by referring the MDR output power to the MDR input power. Numerical calculations also show a phase-shift occurring in each spectral notch position, fact which is in perfect concordance with the Kramers-Kronig relations. The different behaviour of the phase response and the amplitude notch depth with the current is discussed more in detail below.

The resonance placed around 1561.5 nm has been chosen because of two reasons: the first is that minimum insertion loss is achieved; the second, because it is placed inside the telecommunication wavelength region. Fig. 4.7(a) shows a zoomed image of the mentioned resonance. Both the gain and phase transfer functions with the injection current are depicted. In this case, the responses were measured using a low-frequency modulation via the VNA using the method proposed in [88]. A 500-MHz sinusoidal signal, named as $s_{in}(t)$, was transferred onto the optical carrier by means of an IM, giving as a result a DSB signal composed of 3 spectral lines at the MDR input. A modulation depth of 1% was set, guaranteeing small-signal modulation. At the MDR output, the optical signal was detected using a HBW PD. Prior

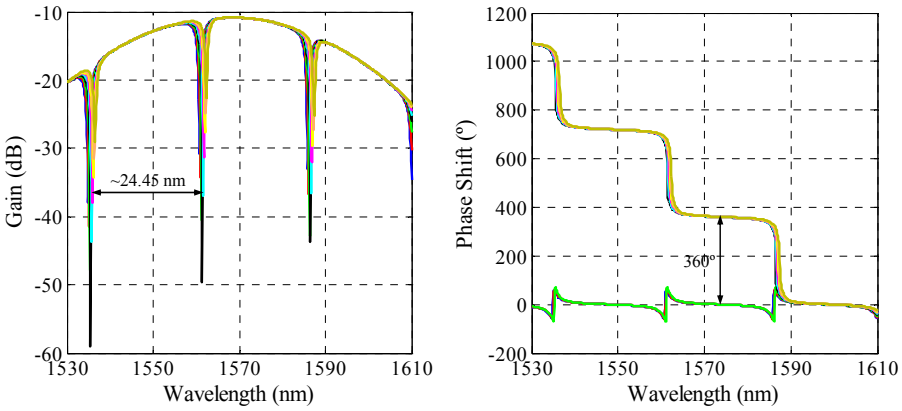

(a)

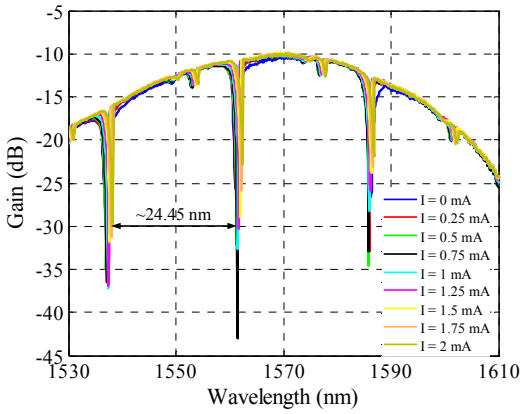

(b)

Figure 4.6: (a) Gain and phase responses of the MDR as a function of the injection current (numerical). (b) Gain response of the MDR as a function of the injection current (measured).

to measure the amplitude and phase by means of the VNA, the electrical signal was amplified. By increasing the current, the roundtrip loss in the cavity decreases due to a higher gain in the III-V layer. Conversely, for lower currents the roundtrip losses are greater than k resulting in sub-coupled regime. Critical coupling gives the maximum notch depth, which occurs for an injection current somewhere close to 0.75 mA, in which both the loss and k are identical. Over-coupled regime, which means a lower loss value than k, is obtained when applying currents from 0.75 mA on approximately. It is important to remark that not only the different operating regimes can be distinguished attending to the gain, but also to the phase-shift feature. Large phase change is only achieved when the structure is under critical or over-coupled regime. To develop phase-shifting functionalities, the over-coupled operating regime is desired because a lower power penalty compared to the critical case is featured and still 2π

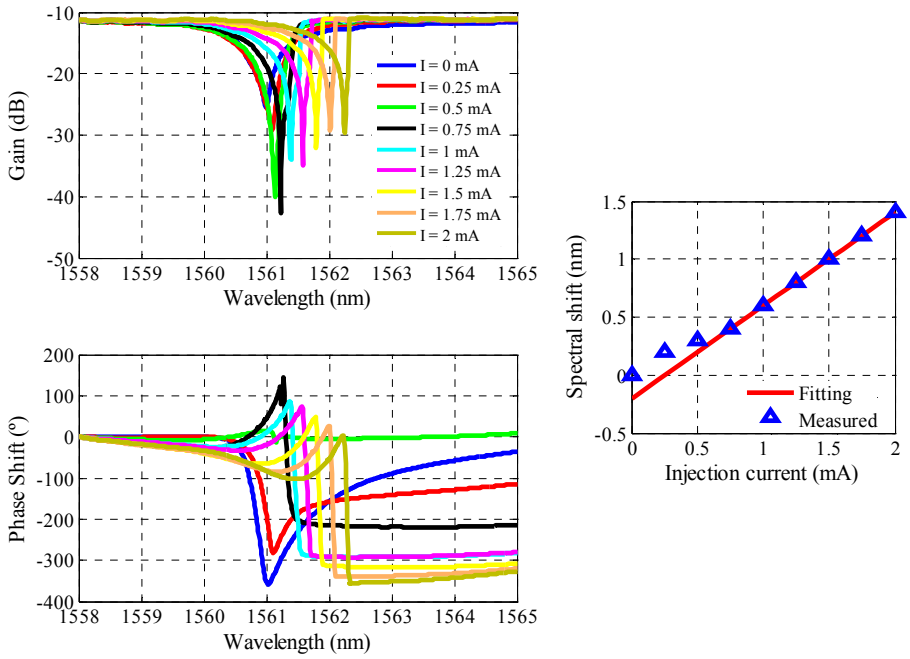

(a) (b)

Figure 4.7: (a) Zoomed image of the measured gain and phase transfer functions of the MDR as a function of the injection current. (b) Spectral shift of the resonance with the current.

phase transitions in each notch are obtained. This fact sets the minimum injection current to be applied. On the other hand, the upper current limit is imposed by the threshold level.

The relative change in the resonance placement as a function of the injected current is plotted in Fig. 4.7(b). This spectral shift is as a result of the effective index modification due to the generation of free carriers in combination with the thermo-optic effect. The thermo-optic effect is as a consequence of the power dissipation in the contact resistance of the metals when injecting current. The larger the injection current, the larger the spectral shift towards higher wavelengths is. The tuning rate is fitted to be 0.8 nm/mA when considering over-coupling.

The effective index can be controlled by acting on the carrier density in the InP cavity. Together with the injection current, the optical power input to the MDR can be also used as an effective index control mechanism. Higher input optical power forces the carrier recombination through the stimulated emission process and therefore the refractive index modification. Fig. 4.8 shows this concept. The gain and phase responses of the MDR as a function of the optical power at the MDR input are depicted in Fig. 4.8(a). The injection current was fixed to 1 mA, whereas the input optical power was swept from 0 to 3 dBm. The device operates under over-coupled regime for these power and current values, since 360°phase shifts are obtained in all

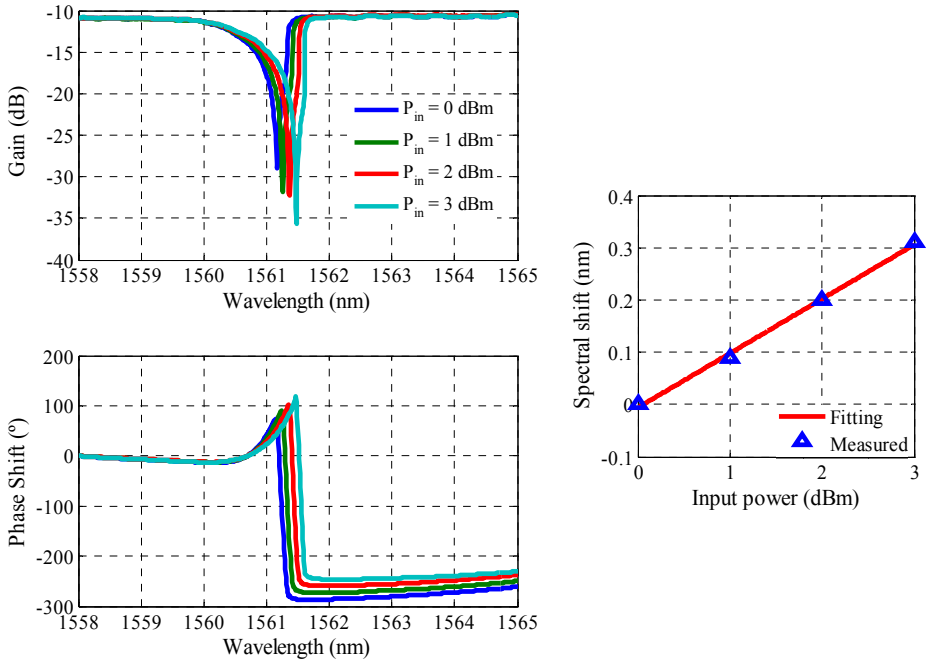

(a) (b)

Figure 4.8: (a) Zoomed image of the measured gain and phase transfer functions of the MDR as a function of the input power into the MDR. (b) Spectral shift of the resonance with the input power into the MDR.

case. Again, a positive spectral shifting is achieved but this time when increasing the input power instead of the injection current. The relative change in the resonance placement as a function of the input optical power is plotted in Fig. 4.8(b). The tuning rate is in this case fitted to be 0.104 nm/dBm.

So far, the MDR has been characterized in terms of the gain and phase responses as a function of the carrier density in the cavity. Now, the unique features offered by MDRs are exploited in order to develop photonic phase shifters for microwave signals.

The accurate exploitation of the MDR phase transfer function in combination with using OSSB modulation results in phase shifting of the detected microwave signal, as already mentioned in Sec. 4.4.1.1. The amount of phase shift can be controlled by the effective index modifications through the carrier injection in the cavity. Figure 4.9 sketches the experimental setup of the InP/SOI MDR based MWP phase shifter. The CW tunable laser generates a weak spectral line centered at 1562 nm. The input RF signal, $s_{in}(t)$, was transferred onto the optical carrier by means of an IM operated in dual-drive configuration, giving as a result OSSB modulation. The signal at the output of the modulator, which is composed of two optical waves, was sent into the MDR. The total optical power inserted at the input vertical grating coupler was 1 dBm. Both optical waves were then weighted and phase-shifted according to the

MDR transfer function, which can be spectrally shifted by modifying the effective index. To this end, a tunable voltage source was connected to the metal contacts of the MDR with the aim of controlling the carrier injection. Polarization controllers were inserted at both the modulator and the MDR input to avoid power penalty derived from polarization mismatching. Finally, the optical signal exiting the MDR output was detected using a HBW PD, amplified by means of an EA and acquired by a VNA.

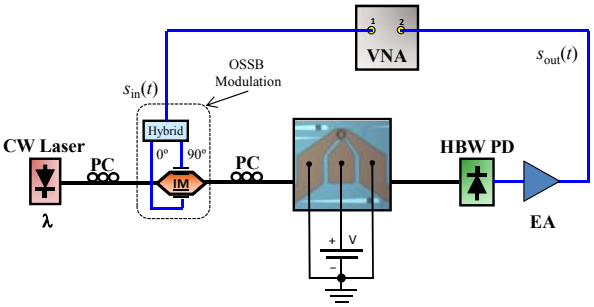

Figure 4.9: Experimental setup for the MWP phase shifter.

Figure 4.10(a) displays a detail of a part of the circuitry used for generating the OSSB modulation, showing among others, the CW laser, the IM operating in dual-drive configuration and the RF hybrid. A picture of the vertical setup for chip characterization and measurement including the input and output optical fiber ports and the XYZ controllers for the probe needles is depicted in Fig. 4.10(b).

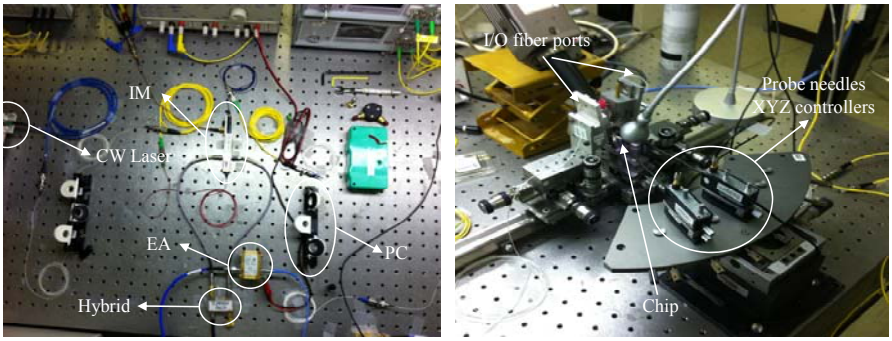

(a) (b)

Figure 4.10: (a) Part of the circuitry used for generating OSSB. (b) Vertical setup for chip characterization and measurement.

Detailed gain and phase transfer functions for a current range between 1.5 and 1.8 mA are illustrated in Fig. 4.11. Both experimental (solid curves) and numerical (dashed curves) results, which have been derived from the model presented in Section 4.4.1.2, show a good agreement. The values of the main parameters used for the numerical calculations have already been given in Tab. 5.1. Misalignments are mostly

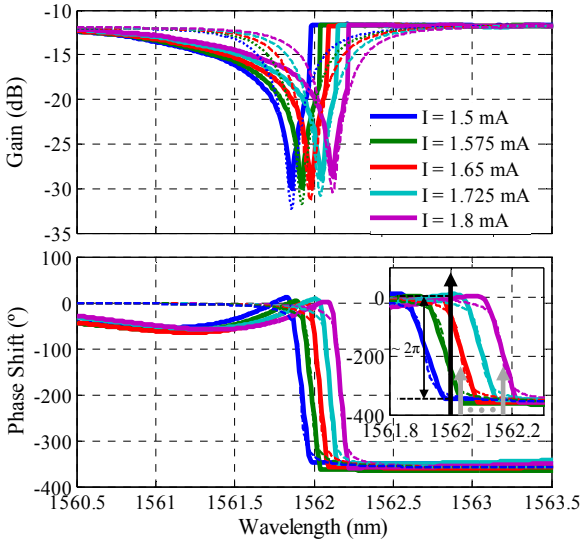

Figure 4.11: Detail of the measured (solid curves) and calculated (dashed curves) transfer functions considering injection currents from 1.5 to 1.8 mA. In the inset, spectral position for both the optical carrier and the modulation sideband within the phase transfer function.

due to the asymmetrical behavior of the resonances. As one can see, the rising edge of the notch in amplitude is more abrupt than the falling one. This fact results in a distorted phase response. In the inset of Fig. 4.11, the spectral position for both the optical carrier and the modulation sideband within the phase transfer function are also depicted. The optical carrier (in black) was fixed and centered at 1562 nm, whereas the frequency of the modulating signal (in grey) was progressively adjusted from 5 to 20 GHz. When sweeping the injection current from 1.5 to 1.725 mA approximately, the carrier experiences a phase change of nearly 2π radians. Conversely, the phase shift induced on the modulation sideband is roughly kept constant. As a result, the phase shift of the optical carrier is transferred to the microwave signal after photodetection.

Figure 4.12 shows the experimental (solid curves) and numerical (dashed curves) results for both the phase shift and the power of the detected microwave signal as a function of the injection current. A good level of agreement between numerical and experimental results is reached. Deviations are attributed to the asymmetrical nature of the resonances, leading to distorted phase transitions. In particular, by using numerical calculations, 2π radians phase shifts are not reached within the current range because the extra phase shift mediated by the distortion in the vicinity of the power deep (see Fig. 4.11) is not taken into account by the semi-analytical model. The differences in the gain response between numerical and experimental results (see Fig. 4.11) are responsible for the deviations in the detected RF power. It can be seen that quasi-linear and continuously tunable phase shifts are obtained. The maximum achievable phase shift at a certain frequency is limited by the abruptness of the transfer function phase slopes. In particular, a minimum modulating frequency

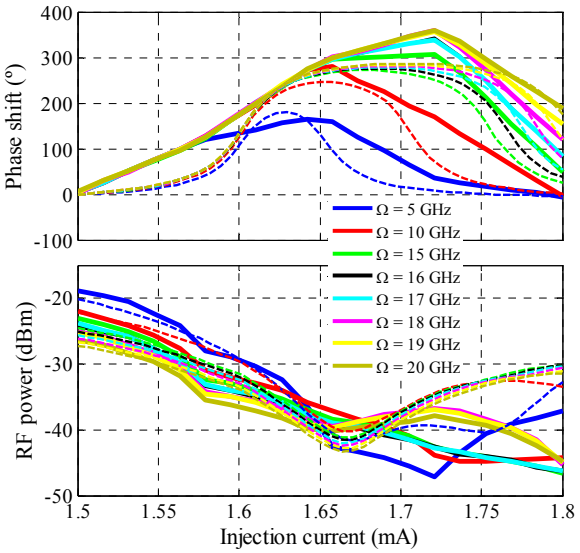

Figure 4.12: Measured (solid curves) and calculated (dashed curves) phase shifts and photodetected powers of the microwave signal as a function of the injection current for different modulating frequencies.

of 18 GHz is required to reach a phase shift of nearby 2π radians. According to the gain transfer function, a phase change is always accompanied by a power penalty. A power variation of roughly 12 dB within the tunability range comprising from 1.5 to 1.725 mA is obtained when the modulating frequency, Ω, is 18 GHz.

Ω (GHz)	5	10	15	16	17	18	19	20
$\Delta\phi$ (°)	165.1	274.6	304.9	336.1	339.5	355.5	352.2	353.8
ΔP (dB)	17.65	15.46	19.53	18.79	18.94	12.29	12.13	11.96

Table 4.2: Maximum phase shift and power variation with the modulating frequency.

Table 4.4.1.3 details both the maximum phase shift, $\Delta\phi$, and the power variation, ΔP, measured for different modulating frequencies. On one hand, $\Delta\phi$ refers to the maximum phase shift, which is stated relative to that obtained when the injection current is 1.5 mA. On the other hand, ΔP is defined as the maximum power variation occurring within the current range from 1.5 mA to the current for which the phase shift is maximum, which is frequency-dependent.

The functionality as a phase shifter is also demonstrated for lower frequencies, however, full 360° phase shifts are not obtained. In such cases, as already mentioned and demonstrated in Chapter 3 when using SOI-based MRRs, the use of cascaded devices represents a suitable solution to enhance the total phase shift. Specifically, by cascading m identical MDRs, the maximum phase shift can be extended by a factor of m.

4.4.2 MWP filter

The suitability of using III-V/SOI-based MDRs for developing MWP phase shifting functionalities has been demonstrated in the previous section. Next, this feature is exploited for the implementation of MWP tunable filtering schemes with complex-valued coefficients. A proof-of-concept approach involving two taps is considered. However, the design can be extended to any arbitrary number of samples.

4.4.2.1 Principle of operation

The general basics of MWP filters has already been covered in-depth in Sec. 1.3. Hereafter, these basic principles are particularized to the implementation of a wide-band and tunable photonic-assisted notch-type filtering scheme for microwave signals using the MDR-based phase shifter as a key element. The principle of operation of rejection-band filters have been presented in Sec. 2.5.1. In this case, the working principle is exactly the same, except a the MDR-based phase shifter is used instead of the cascaded SOA-based configuration.

Hence, the MDR-based MWP phase shifter is inserted in one arm of the interferometric structure in order to provide controllable basic phase shift. Since about 2π phase shifts have been demonstrated using the MDR, almost 100% fractional tuning is reached, as it is demonstrated in the following section.

4.4.2.2 Theoretical and experimental results

The experimental setup for the MDR-based MWP filter is sketched in Fig. 4.13. The MDR was inserted in the lower arm of the interferometric structure. In this manner, the phase shift between both taps can be controlled by properly adjusting the injection current into the MDR. The interferometric structure was characterized by a length imbalance of 1.27 m, which corresponds to a notch-type response with a FSR of about 163 MHz. The emission wavelength of the CW laser was fixed at 1562 nm. A VOA was used in the upper arm to enhance the rejection level. At the output of the IM, the OSSB signal was amplified by means of an EDFA. A 0.8-nm-wide BPF centered at the carrier wavelength was also used for spontaneous noise suppression purposes. The linewidth of the CW laser was around 10 MHz, which results in coherence time of nearly 32 ns. Therefore, to avoid coherency-related problems, a BPD was used since T was around 6.1 ns.

In order to obtain the maximum fractional tuning, the center frequency of the filter must be high enough to be phase-shifted up to 360°. Moreover, zero phase imbalance between the minimum and maximum frequency over the filter operating bandwidth is required to guarantee distortion-free filter transfer function. Fig. 4.14 shows the measured (solid curves) and calculated (dashed curves) gain and phase transfer functions with the injection current. Moreover, a detail of the spectral position for the optical carrier and the filter frequency band is illustrated. The values of the main parameters used for the numerical calculations have already been given in Tab. 5.1. Here, the modulating signal is wideband instead of a single spectral component, whose center frequency and operating bandwidth are f_c and BW respectively. Δf refers to the phase slope bandwidth (see Fig. 4.14).

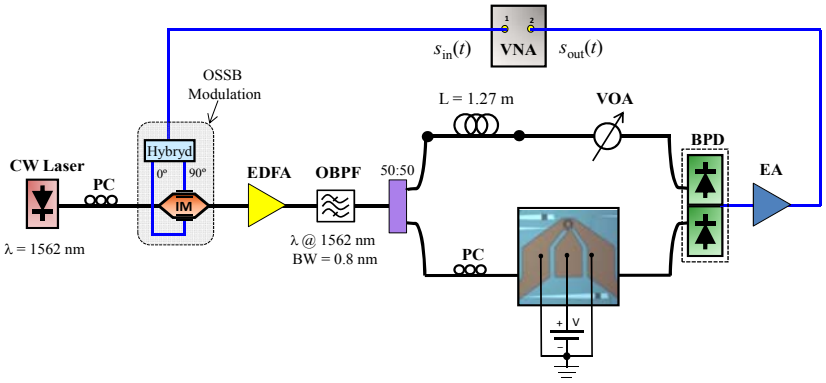

Figure 4.13: Experimental setup for the MDR-based MWP filter.

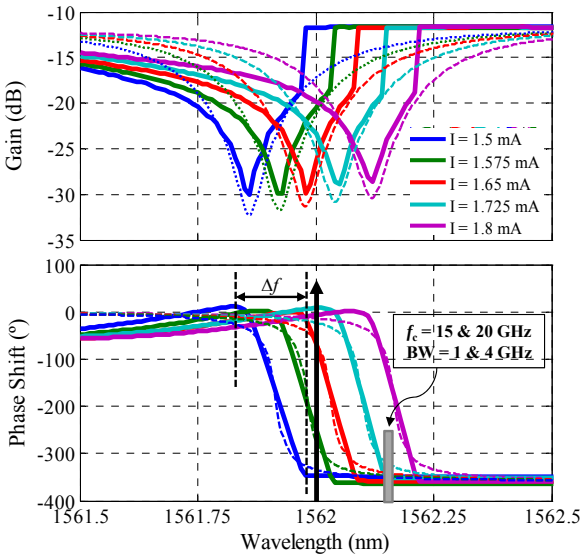

Figure 4.14: Measured (solid curves) and calculated (dashed curves) transfer functions with the injection current. Detail of the spectral position for the optical carrier and the filter frequency band.

Three different combinations for the tandem f_c and BW are taken into account: f_c = 20 GHz and BW = 1 GHz, f_c = 20 GHz and BW = 4 GHz and f_c = 15 GHz and BW = 1 GHz. Let us recall that in the Sec. 4.4.1, the minimum frequency for obtaining fully tunable 2π phase shift has been 18 GHz within the current range from 1.5 to 1.725 mA.

Firstly, an f_c of 20 GHz and a BW of 1 GHz have been chosen, i.e. from 19.5 GHz to 20.5 GHz. Fig. 4.15 displays the normalized filter frequency response for

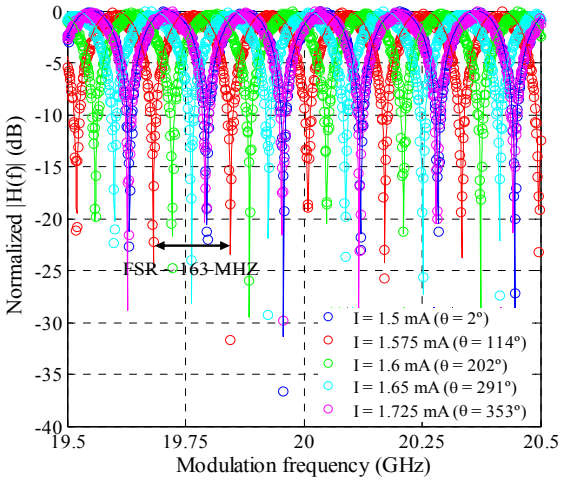

Figure 4.15: Measured (markers) and theoretical (solid curves) normalized $|H(f)|$ of the tunable filter for different I when $f_c = 20$ GHz & BW = 1 GHz.

different injection currents, I, into the MDR. Experimental (markers) and theoretical (solid curves) results show a good agreement. The small deviations are attributed to reflections in the electrical part of the setup, the residual unwanted sideband in the OSSB modulation and the spontaneous noise. The theoretical results have been obtained by using Eq. 2.21. The same power penalty in both branches of the interferometric structure was enabled by adjusting the VOA for each injection current, so $|a_0| = |a_1| = 1$ has been assumed. On the other hand, $T = 6.1$ ns and θ depends on the injection current. Nearly 2π radians controllable θ over the operating bandwidth leads to distortion-free filter responses with continuously tunable 100 % FSR fractional tuning.

Distortion-free responses with enhanced operating bandwidths can be obtained while all the frequency components in the usable bandwidth experience constant phase. In Fig. 4.16 the bandwidth has been enlarged till 4 GHz while keeping the f_c fixed to 20 GHz. The filter frequency band therefore spans from 18 GHz to 22 GHz, where the phase transfer function is flat within the current range from 1.5 to 1.725 mA (see Fig. 4.14). The minimum frequency of the filter band is 18 GHz, which is high enough to be phase-shifted 360°, leading to fully tunable filter response.

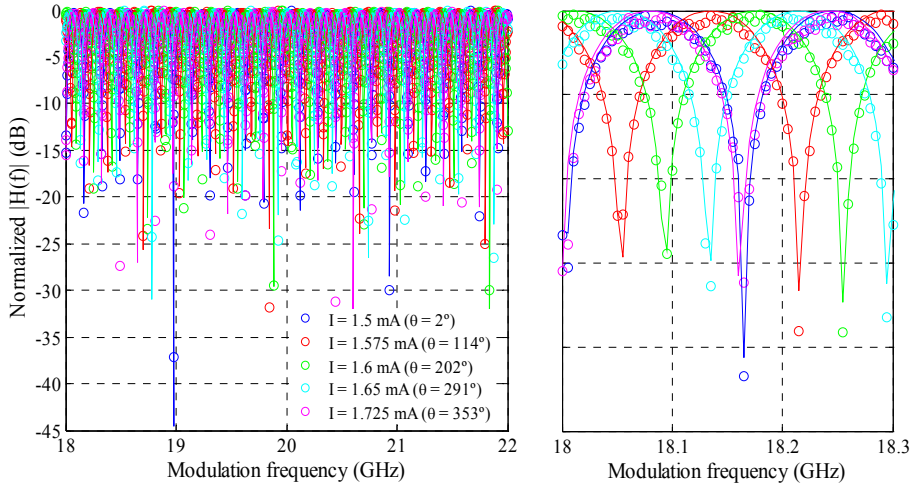

(a) (b)

Figure 4.16: (a) Measured (markers) and theoretical (solid curves) normalized $|H(f)|$ of the tunable filter for different I when $f_c = 20$ GHz & BW = 4 GHz. (b) Zoom-in.

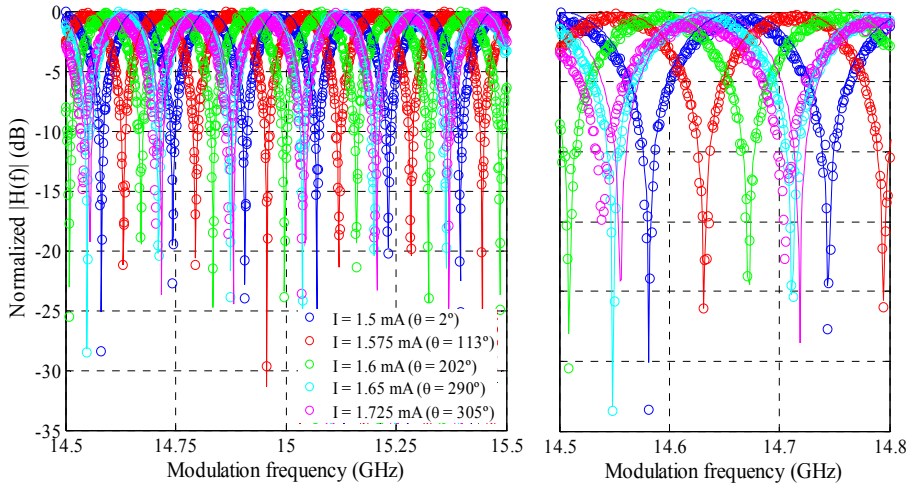

(a) (b)

Figure 4.17: (a) Measured (markers) and theoretical (solid curves) normalized $|H(f)|$ of the tunable filter for different I when $f_c = 15$ GHz & BW = 1 GHz. (b) Zoom-in.

Finally, f_c and BW have been set to 15 GHz and 1 GHz respectively. If attention is paid to the maximum I is injected, i.e. 1.725 mA, distortion can be discerned in the response at lower frequencies. This distortion is due to the fact

that all the frequencies within the usable bandwidth are experiencing non-constant phase shift as a consequence of the slope in the phase transfer function. This fact leads to distorted filter responses, as one can see in Fig. 4.17. Higher frequencies belonging to the usable bandwidth experience constant phase, so distortion have not taken place. Therefore, the maximum operating bandwidth attending to a specific center frequency is completely set by the phase slope abruptness of the MDR phase transfer function. As a result, there exists a trade-off between f_c, BW and Δf in order to get non-dispersive filter responses, which is given by

$$f_c \geq \Delta f + \frac{BW}{2}. \tag{4.27}$$

4.4.3 Electro-optic phase modulator

In previous sections, MWP tunable phase shifter and filter based on III-V/SOI MDRs have been proposed and demonstrated. Here, the unique features provided by the MDRs are exploited to accomplish phase modulation tasks. In particular, an electro-optical phase modulator (EOPM) using a single MDR is presented, showing low power consumption, high-speed operation and low complexity.

4.4.3.1 Context

Phase modulation represents a key functionality in next generation optical networks. Advanced formats involving phase modulation are essential to meet the demanding requirements in terms of efficiency and speed. To date, several approaches integrated on different technology platforms have been reported, such as those based on lithium niobate [122], InP [123], SOI [124, 125], deformable waveguide actuated by MEMS [126], nano-electro-mechanical systems (NEMS) fabricated on SOI [127], liquid crystals [128] or polymers [129]. Among them, SOI-based approaches are preferred due to the possibility of high-density integration, as well as CMOS compatibility [100]. In silicon, phase modulation relies on controllable refractive index modification. The thermo-optic effect and the FCD are the most commonly used mechanisms to implement tunable refractive index. Thermo-optics is the simplest way. However, drawbacks such as the response times in the μs range [130], the thermal crosstalk and the large power consumption due to the continuous current flow hamper its assembly in high-speed optical data links. On the other hand, the response time can be greatly enhanced by exploiting the FCD effect through carrier injection or depletion [131]. Carrier-depletion-based approaches can reach operation speeds of several hundreds of Mbps. Yet large interaction lengths owing to the small light confinement in the depletion region are required. This fact in combination with an optical absorption increase provided by the carrier extraction, result in a modest power handling [132]. Regarding carrier injection, the response time is limited by the carrier recombination process in silicon, i.e. few ns [133]. Nevertheless, the modulation efficiency is improved compared to that obtained by carrier depletion, since extra loss derived from light absorption is avoided. In order to enhance the modulation speed in FCD-based schemes, a special driving technique known as pre-emphasis can be used [134]. As a consequence, the speed of OOK modulated signals has been pushed up to 18

Gbps when using carrier depletion in micro-rings [135]. Advanced modulation formats improves the performance in the context of sensitivity and robustness against non-linear effects. Recently, error-free transmission of differential-phase-shift-keyed (DPSK) modulated signals at 5 Gbps exploiting carrier depletion with pre-emphasis in silicon micro-rings has been demonstrated for the first time [136].

On the other hand, hybrid approaches consisting of bonding active III-V compounds on top of SOI circuits represent a feasible solution in order to enhance the modulation performance [137, 138]. Inherent dynamics in semiconductor materials is faster than in silicon. In particular, carrier depletion has been used in a 1-mm-long hybrid silicon-AlGaInAs waveguide. The speed is not further limited by the carrier dynamics, but by parasitic capacitance in the metal contacts [138]. The bandwidth can be extended to few tens of Gbps assisted by an optimized microwave design [137].

In this section, a novel scheme implementing an EOPM based on a single InP/SOI MDR operating in the microwave band is presented and demonstrated. To the best of our knowledge, it corresponds to the most compact solution reported so far. As a proof-of-concept, binary phase shift keying (BPSK) modulation format is used. Finally, the main advantages and drawbacks are discussed.

4.4.3.2 Principle of operation

The principle of operation of InP/SOI MDR based phase modulators is illustrated in Fig. 4.18(a). The concept is explained attending a 2-level digital phase modulation scheme, although it can be generalized to any arbitrary number of levels without loss of generality. The principle of operation relies on exploiting the phase change which occurs in the vicinity of a resonance under over-coupled regime. This phase change is controlled by the effective index modification through carrier injection. Both the input optical power and the injection current can be used as control mechanisms for altering the carrier density inside the semiconductor compound thus allowing for controllable tuning of the phase shift. In this case, the electrical injection is chosen since the constant output average power of the optical carrier is highly preferable in phase modulation schemes.

Hence, the metal contacts of the MDR are electrically driven by the modulating data signal. The voltages for the high and low levels have to be accurately adjusted in order to reach π phase shift. This way when the voltage level of the modulating signal switches, a 180° phase shift is imprinted on the optical carrier. Moreover, zero power variation when switching from one symbol to the other is desired since residual amplitude modulation must be avoided. Ideally, no power variation is obtained if the emission wavelength is accurately set. Regarding the modulation speed, it is limited by the dynamics in the semiconductor, which typically is of the order of tens of picoseconds. This means that modulation rates as fast as few tens of Gbps can be reached.

4.4.3.3 Proof-of-concept: BPSK modulation format

This section focuses on demonstrating the suitability of using the InP/SOI MDR as an EOPM. For this purpose, the use of the BPSK modulation format has been chosen as a proof-of-concept. BPSK (or 2-PSK) relies on synthesizing a phase difference of

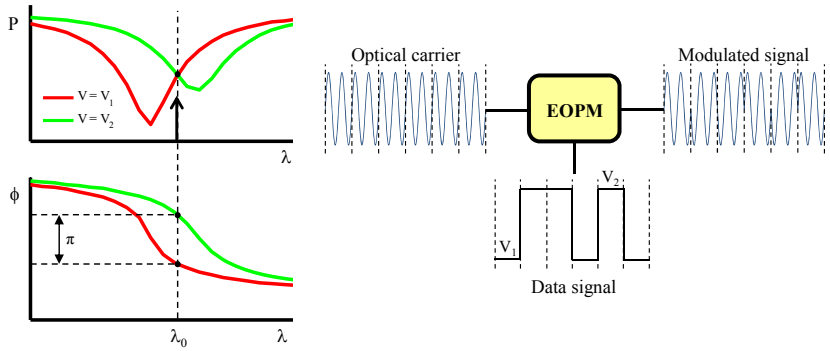

(a) (b)

Figure 4.18: (a) Principle of operation of the InP/SOI MDR based EOPM. (b) Exemplary case.

180° between both modulating symbols. Hence, the modulated signal is as a result of conveying the data signal on the phase of the optical carrier. An exemplary case is illustrated in Fig. 4.18(b), in which the optical carrier, the data and the modulated signals can be seen.

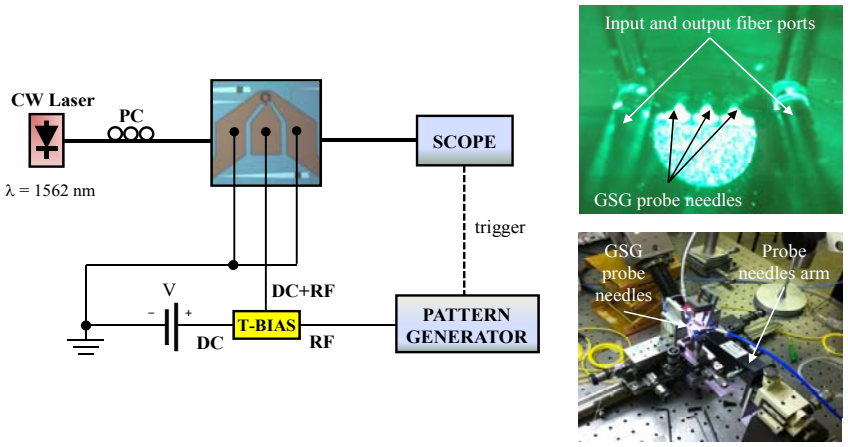

(a) (b)

Figure 4.19: (a) Experimental setup implementing the MDR-based EOPM. (b) Detail of the GSG probe needles on the metal contacts (top) and setup for chip characterization and measurement (bottom).

The experimental setup implementing the EOPM is sketched in Fig. 4.19(a). TE-polarized light from a tunable laser operated in CW was coupled into the MDR. The InP compound of the MDR cavity was heterogeneously integrated on and coupled to a nanophotonic SOI waveguide circuit containing a 650-nm-wide and 220-nm-high

Si strip waveguide using molecular bonding. The 9-μm-diameter MDR includes three strained InP-InGaAsP quantum wells, as well as a tunnel junction for loss minimization purposes, as already detailed in Section 4.2. The modulating signal was generated by a pattern generator in combination with a direct current (DC) voltage source. Therefore, the use of RF probe needles was required. In particular, 100-nm-pitch GSG-type probe needles working up to 40 GHz were utilized. A picture showing a detail of the GSG probe on the metal contacts of the MDR is shown in Fig. 4.19(b) (top). For this purpose, the setup for chip measurement and characterization was modified. In Fig. 4.19(b) (bottom), a picture depicting the probe needles arm is shown. At the MDR output, the light was collected using a high-bandwidth oscilloscope, which was triggered by the pattern generator.

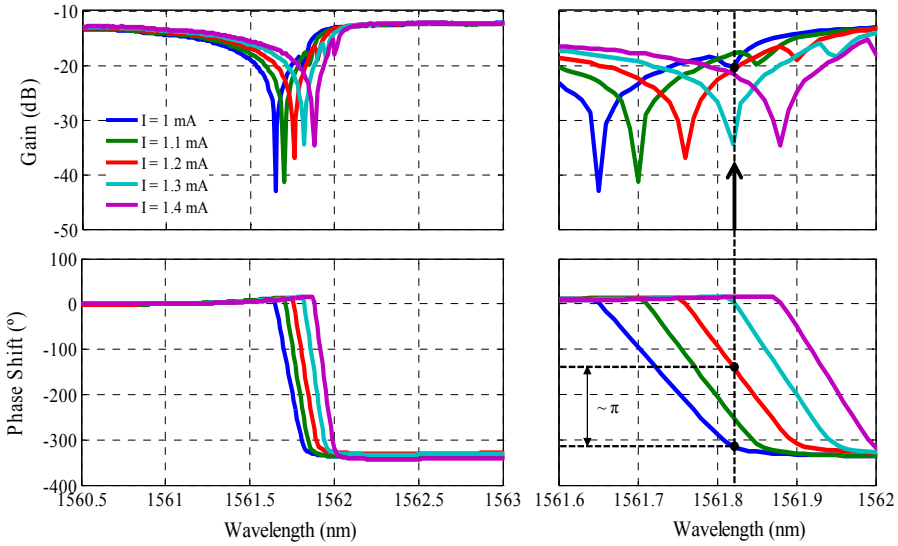

Figure 4.20: Gain and phase transfer function with the current range. Detail of the spectral position of the optical carrier in the transfer function.

Figure 4.20 shows both the gain and phase transfer functions with the current injected into the MDR. The spectral position of the notch can be modified by changing the injection current. Consequently, the phase response is accordingly shifted. As a result, the phase experienced by the optical carrier can be adjusted by means of the injection current. On one hand, the MDR must be operated below threshold to avoid coherency-related problems. On the other hand, the over-coupled regime is required to obtain full 360° phase shifts. These facts limit the injection current range. The emission wavelength of the optical carrier was set to 1561.82 nm in order to achieve 180° phase shift when sweeping the injection current into the MDR from 1 to 1.2 mA. This wavelength was also determined by the gain response, since power variations as low as possible within the current range were desired. A power difference between both modulation symbols of only 0.6 dB was obtained. The output power of the CW laser was set to 2 dBm. A 127-bit non-return to zero (NRZ) square-wave signal at 1.25 Gbps was applied at the metal contacts. The DC source was set to a voltage resulting in 1 mA bias current delivered, while the peak-to-peak level of the NRZ

signal was 0.57 V, corresponding to 200 μA.

Figure 4.21(a) displays the waveform at the MDR output. After reaching the steady state, a power imbalance of nearly 0.6 dB between both levels was measured. This is in perfect agreement with the results derived from Fig. 4.20. From the output waveform, the rise and fall times can be estimated, to be about 400 ps and 150 ps, respectively. Consequently, the maximum modulation speed is estimated to be 1.8 Gbps approximately. The small-signal response of the MDR, known as S_{21}, is shown in Fig. 4.21(b). An injection current of 1 mA and a CW laser output power of 2 dBm were used. The -3 dB bandwidth was around 1.8 GHz. This confirms that modulation rates as high as 1.8 Gbps could be achieved, as previously derived from the output waveform.

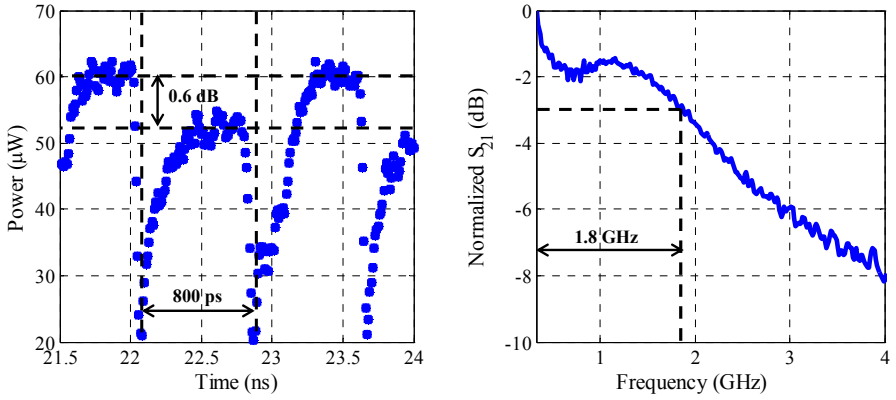

(a) (b)

Figure 4.21: (a) Waveform at the MDR output. (b) Small-signal response, S_21, of the MDR.

Next, the phase shift of the modulated output signal was investigated. For this purpose, a Mach-Zehnder interferometer (MZI) was used with the aim of converting phase-to-intensity modulation (PM-IM). The setup is illustrated in Fig. 4.22. A 4-dBm-power optical signal at 1561.82 nm was split employing a 3 dB coupler. In the lower arm, the MDR-based EOPM was inserted. The length of both branches was perfectly balanced by means of a variable delay line (VDL). The coupled output signal was collected by the oscilloscope. A variable attenuator was also used in the upper arm to compensate the loss derived from the MDR.

Results are displayed in Fig. 4.23. The optical power was measured prior to the output coupler in both arms under static conditions. These powers are named as P_0 and P_1 respectively in Fig. 4.23. The attenuator was adjusted for obtaining the same average power level at the upper and lower arm outputs when considering an injection current of 1 mA. The powers P_0 and P_1 were around 48.2 μW and the attenuation was fixed to 11.6 dB. For the lower arm, P_1 was also measured when injecting 1.2 mA. The average power difference was around 0.6 dB. This value perfectly agrees with the preceding results. Following, dynamic measurements were accomplished by applying the same driving signal which was previously used. When P_0 and P_1 are identical,

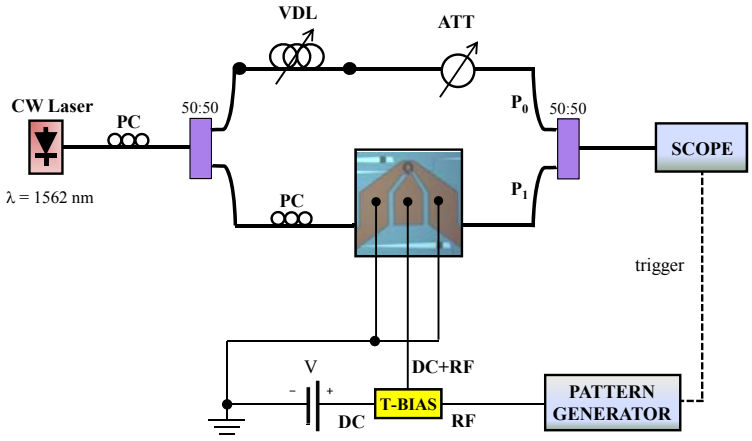

Figure 4.22: Interferometric-based setup for PM-IM conversion.

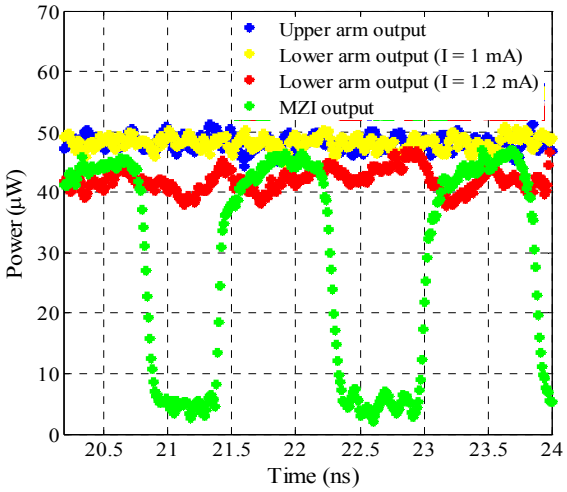

Figure 4.23: Waveforms at the MZI output, as well as at the upper and lower arm outputs prior to the coupler.

as well as the phase imbalance between both arms is zero, constructive interference takes place at the MZI output. This means that the total output power is equal to P_0 or P_1. Conversely, phase imbalance of 180° yields destructive interference, giving as a result no power at the output. The MZI output power is also shown in Fig. 4.23. An extinction ratio of 10.3 dB was obtained, demonstrating the suitability of the MDR to be operated as an EOPM. Larger extinction ratio was not reached as a consequence of the power deviation between both modulation symbols, the slightly different π radians phase shift between both symbols and the spontaneous noise generated by the MDR.

4.4.3.4 Increasing the modulation rate

In the previous section, a modulation rate of nearly 1.8 Gbps has been demonstrated. Yet the semiconductor compound was designed to reach recombination times in the order of several tens of ps, the device has not been able to be operated at modulation rates as high as expected. The reason has been the parasitic effects in the metal contacts, fact which at the end has limited the speed. From the microwave point of view, the MDR can be modelled as a resistor-capacitor (RC) circuit whose behavior corresponds to a low-pass filter. The frequency for which the filter attenuates the half of its original power, i.e. the filter bandwidth is

$$f_{-3dB} = \frac{1}{RC}, \tag{4.28}$$

where R and C are the resistance and the capacitance respectively. The goal deals with minimizing the R and C in order to enlarge the operating bandwidth. The deposition of metals on semiconductor materials is a critical step in the fabrication flow. Other approaches using hybrid technologies consisting on bonding III-V materials on top of SOI circuits reported up to now has faced the same problem [137, 138]. In particular, the reduction of the MQW width has been proposed for decreasing the value of C in [137]. On the other hand, R can be reduced by using thinner metal films based on materials with higher conductivity. These facts in combination with a proper impedance matching result in enhanced modulation rates. These considerations can be directly transferred to the design of the MDR.

If the bandwidth is not limited by the parasitic effects in the metal contacts assisted by a performed microwave design, the carrier dynamics of the semiconductor governs the time response of the MDR. In carrier-injection-based semiconductors, the dynamic bandwidth is limited by the recombination process which is typically in the order of several tens of GHz. The recombination process performance depends on the carrier density. Consequently, higher input optical power and/or bias current enhance the stimulated emission resulting in improved bandwidth. In Fig. 4.24, the measured normalized S_{21} for a MDR whose bandwidth is not limited by the parasitic effects is displayed. The input optical power input to the MDR was fixed to 3 dBm, whereas the bias current was swept from 2 to 3 mA. As one can see, the bandwidth was extended from 2.3 GHz to 3.1 GHz when increasing the current from 2 mA to 3 mA. However, the main drawback consists of a higher power consumption.

Remember that, on one hand, the MDR must be operated below threshold to avoid coherency-related problems. On the other hand, the over-coupled regime is required to obtain full 360° phase shifts. These facts limit at the end the injection current range for a fixed input optical power.

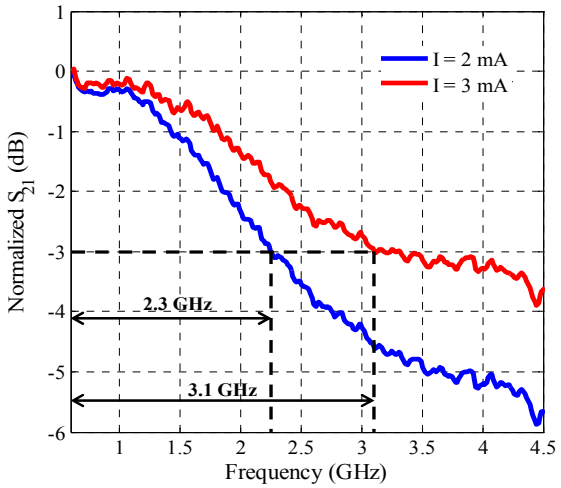

Figure 4.24: Small-signal response, S_{21}, of the MDR when the input optical power is 3 dBm.

Finally, the dynamics can be also speed-up by using special driving techniques. These techniques, which are known in the literature as pre-emphasis, are based on forcing the injection or depletion of carriers through proper modulating signal engineering. Pre-emphasized driving signals have already been successfully demonstrated in SOI-based approaches [135, 136]. In such a way, the rise and fall times can be shortened resulting in modulation rates as high as 18 Gbps [136]. Likewise, pre-emphasis techniques could be also used in hybrid III-V/SOI approaches to enhance the dynamics in the semiconductor.

4.5 Summary and conclusions

In this chapter, SFL effects in a novel ultra-small device (footprint 0.1 mm^2 approximately) based on InP/SOI MDR have been observed. These effects, which allows for controllable group index, have been exploited for the implementation of several functionalities in the fields of photonic RF and digital data signal processing.

Firstly, a broadband MWP phase shifter based on a single III-V/SOI MDR in combination with OSSB modulation has been proposed and demonstrated. Quasi-linear and continuously tunable roughly 360° phase shifts have been experimentally obtained when considering radiofrequencies greater than 18 GHz. Phase shift tunability has been accomplished by modifying the effective index through carrier injection in the III-V layer. As a consequence, the tunability speed was limited by the carrier dynamics in the semiconductor, which is in the scale of hundreds of picoseconds. This fact greatly improves the performance compared to other similar Si-based approaches, in which the thermo-optic effect is used as tunable mechanism. The power consumption has been between 10.1 mW and 13.4 mW approximately within the tuning range. A semi-analytical model has been derived, whose results have been in good agreement

with the measurements. Next, the phase shifter has been exploited for implementing complex-valued coefficients in tunable MWP filtering schemes. A proof-of-concept implementation involving two taps has been demonstrated. Distortion-free and high-bandwidth filter responses with tuning range of approximately 100% over the FSR have been obtained. The trade-off between the center frequency and the operating bandwidth in MDR-based approaches has been defined.

Finally, an EOPM based on III-V-on-silicon MDR has been introduced. Carrier injection has enabled effective index modifications resulting in phase modulation. Proof-of-concept implementation involving BPSK modulation at 1.25 Gbps with a power imbalance of nearly 0.6 dB between both symbols has been demonstrated. A peak-to-peak voltage of just 0.57 V is needed for the modulating signal. The modulation rate could be pushed up to 1.8 Gbps without using any special driving technique according to the time and frequency MDR responses. Furthermore, this modulation rate can be extended to several tens of Gbps assisted by an optimized microwave design in order to minimize the parasitic effects in the metal contacts.

The objectives of this chapter have been fulfilled and recognized by the community in the following international publications:

1. **J. Lloret**, R. Kumar, S. Sales, F. Ramos, G. Morthier, P. Mechet, T. Spuesens, D. Van Thourhout, N. Oliver, J.-M. Fédéli and J. Capmany, "Ultracompact electro-optical phase modulator based on III-V-on-silicon microdisk resonator", Optics Letters, vol. 37, no. 12, pp. 2379-2381, 2012.

2. **J. Lloret**, G. Morthier, F. Ramos, S. Sales, D. Van Thourhout, T. Spuesens, N. Olivier J.-M. Fédéli and J. Capmany, "Broadband microwave photonic fully tunable filter using a single heterogeneously integrated III-V/SOI-microdisk-based phase shifter", Optics Express, vol. 20, no. 10, pp. 10796-10806, 2012.

3. **J. Lloret**, F. Ramos, S. Sales, J. Capmany, G. Morthier, D. Van Thourhout, T. Spuesens, N. Olivier and J.-M. Fédéli, "Fully tunable microwave photonic phase shifter for broadband signals based on a single heterogeneously integrated III-V-on-Silicon microdisk resonator", in European Conference on Optical Integration (ECIO), Sitges (Spain), paper 158, 2012.

Chapter 5

Summary, conclusions and open research lines

5.1 Summary and conclusions

In this PhD thesis, research on slow light effects occurring in ASPICs has been conducted. Slowing down the group speed of light has been exploited for implementing several complex photonic-assisted RF and digital data signal processors. In particular, the PICs have been implemented by using three different technological platforms based on InP/InGaAsP, SOI and III-V-on-silicon hybrid compounds.

The cascade of PSSs composed of an InP/InGaAsP based SOA waveguide followed by a notch-type filter was demonstrated aiming at implementing fully tunable and broadband MWP phase shifters [32, 35]. The use of SOAs is fundamentally accompanied by additive noise due to the spontaneous emission process, whose impact becomes specially important in cascaded configurations. This additive noise degrades the quality of the phase-shifted microwave output signal. Therefore, an accurate characterization of the noise performance in cascaded SOA based MWP phase shifters has been accomplished in this thesis. In particular, a comprehensive numerical model for the purpose of assessing the noise spectrum at the phase shifter output has been derived. The model has been corroborated by means of experimental results showing good agreement. In addition to the ASE noise, other noise sources such as the RIN from the laser and the current source noise have been also considered. The ASE-signal beat-note has been identified as the dominant noise contribution. Relative-intensity-noise levels up to -150 dB/Hz have been obtained at the phase shifter output. The role of the notch filter dispersion resulting in noise enhancement mediated by frequency-to-intensity modulation conversion has been also studied in-depth. A customized solution involving a tailored filter instead of a standard notch filer has been presented, yielding SNR improvement by several dB. Some suggestions on the optimization in terms of the noise performance related to the operating points of the SOAs comprising the phase shifter have been proposed as well. Then, the MWP phase shifter has been

used as a key block in the implementation of a MWP tunable filter. As a proof-of-concept, a notch-type filter centered at 20 GHz has been demonstrated over a 2 GHz bandwidth. A tuning range of nearby 100% over a FSR of nearby 500 MHz has been reached.

SOI MRRs in combination with OSSB modulation were shown as a suitable solution for implementing photonic-assisted phase shifting tasks of microwave and millimiter-wave signals [82, 85]. By exploiting this concept, a novel tunable complex-valued multi-tap transversal microwave photonic filter based on a single SOI MRR has been proposed and demonstrated. Filter response tunability without changing the FSR have been accomplished by properly setting the emission wavelength of N tunable lasers. The trade-off between the filter selectivity, given by the number of samples N, and the degree of tunability has been studied in-depth. Fractional tuning over the FSR greater than 77% has been obtained when implementing two taps, whereas in the case of four taps it has been above 24%. The possibility of enhancing these fractional tunings has been proposed by using cascaded SOI MRRs. The performance in terms of SLL has been improved by properly engineering windowed samples and different window taps schemes have been evaluated. In particular, the Hamming window with $B = 0.8$ has yielded the maximum SLL levels, rising up to 23 dB. Then, the unique dispersion features of SOI MRRs have been exploited for designing a multi-channel TTD line. After introducing a new concept named as E-SCT, which benefits from resonant-type structures aiming at partially overcoming the limitation in terms of small delay-bandwidth product, a novel approach has been proposed. It is mainly based on an array of cascaded SOI MRRs in combination with the SCT unit. Discretely controllable delays from 100 ps to 800 ps with step of 100 ps has been achieved in order to imprint a delay on a multiplex based signal comprising 4 data-modulated RF carriers. Simultaneous delay over aggregate instantaneous bandwidth exceeding 4.5 GHz has been reached. Furthermore, the inherent structure of the proposed approach allows for flexible designs in the context of maximum delay, RF channel spectral separation and number of channels.

III-V/SOI MDRs were used to develop several all-optical signal processing involving digital signals [111]. However, the potential of this device for implementing MWP functionalities was unexplored. In this thesis, controllable group index has been observed in this device enabling the implementation of several tasks in the fields of photonic RF and digital data signal processing. Firstly, a broadband MWP phase shifter based on a single III-V/SOI MDR in combination with OSSB modulation has been proposed and demonstrated. Quasi-linear and continuously tunable roughly 360° phase shifts have been experimentally obtained when considering radiofrequencies greater than 18 GHz. Phase shift tunability has been accomplished by modifying the effective index through carrier injection in the III-V compound. As a consequence, the tunability speed has been limited by the carrier dynamics in the semiconductor, which is in the scale of hundreds of picoseconds. This fact greatly improves the performance compared to other similar Si-based approaches, in which the thermo-optic effect is used as tunable mechanism. The power consumption has been between 10.1 mW and 13.4 mW approximately within the phase tuning range. A semi-analytical model has been derived, whose results have been in good agreement with the measurements. Next, the phase shifter has been exploited for implementing complex-valued coefficients in tunable MWP filtering schemes. A proof-of-concept implementation involving two taps has been demonstrated. Distortion-free and high-

bandwidth filter responses with tuning range of approximately 100% over the FSR have been obtained. The trade-off between the center frequency and the operating bandwidth in MDR-based approaches has been defined. On the other hand, a novel EOPM based on III-V-on-silicon MDR has been introduced. Carrier injection has enabled effective index modifications resulting in phase modulation. A Proof-of-concept implementation involving BPSK modulation at 1.25 Gbps with a power imbalance of nearly 0.6 dB between both symbols has been demonstrated. A peak-to-peak voltage of only 0.57 V is needed for the modulating signal. The possibility of extending up to 1.8 Gbps the modulation rate has been demonstrated without using any special driving technique. Furthermore, the modulation rate limiting factor has been identified to be the parasitic effects in the metal contacts. Mediated by an optimized microwave design, this modulation rate can be extended to several tens of Gbps.

5.2 Performance of microwave and millimeter-wave signal filters. A comparison

The common goal of implementing filtering functionalities by deploying the three different technological platforms dealt with this thesis has been carried out. Cascaded SOA based, SOI MRR based and III-V-on-Si MDR based RF photonic filters have been proposed and demonstrated all over this dissertation. To date, a large number of approaches developing filtering tasks by photonic means have already been published. Hereafter, the most promising schemes so far reported in the literature are compared to the approaches developed in this thesis. Moreover, several purely electronic counterparts have also been considered in the comparison.

A set of FoM including metrics such as bandwidth, operating frequency, size, tuning speed and range, insertion loss, bandpass/rejection level and power consumption has been used. In bandpass filters, *bandwidth* (BW) is defined as the -3 dB or the full width half maximum (FWHM) of the passband, while for notch filters it refers to the spectral width at the rejection level of 20 dB with respect to the maximum. The *operational bandwidth* is defined as the spectral range within which the filter response can be tuned (it may not necessarily be equal to the FSR). The *central frequency* refers, in the case of bandpass filters, to the position of the first maximum without considering baseband, while in notch-type filters it corresponds to the frequency where the operational bandwidth centres. *Size* and *insertion loss* address here only to the subsystem that enables filter tunability, i.e. the cascade of SOAs, the SOI MRR or the III-V-on-Si MDR in our particular filter implementations. In addition, *insertion loss* refers to the overall optical loss in MWP and electrical loss in microwave (MW) filters. The rejection level indicates the SLL ratio for bandpass filters, while it addresses the suppression in the notch-type filters. The *tuning range* is expressed in terms of the FSR for both the bandpass and notch-type filters. The lowest timing scale in order to perform filter tunability is given by the *tunability speed*. Finally, the *power consumption* only refers to the power required to operate the subsystem enabling the filter functionality (SOAs, SOI MRR and III-V-on-Si in our case). The term “high” indicates more than 100 mW while “medium” indicates a power consumption range comprising from 10 and 100 mW.

As derived from Tab. 5.1, the choice of using a certain technology is application-dependent. Purely electronic microwave devices (5BT-1800/2200-1S, 3TNF-3000/4000-N/N and [146]) can implement both notch-type and band-pass-type schemes. Only relatively narrow-band responses with a limited tuning range up to 30% over the central operating frequency are feasible, resulting in poor reconfigurability and flexibility. Besides, slow tuning times in the second or millisecond [146] scale are required. However, high performance is reached in terms of insertion loss and rejection level (5BT-1800/2200-1S, 3TNF-3000/4000-N/N). In general, the photonic-assisted approaches report faster tuning speeds and ranges. Schemes comprising active devices (SOA, III-V-on-Si and [59, 139, 144]) experience a higher power consumption compared to the passive based solutions (SOI and [87,140,142,143,146]). In contrast, the active nature can be used in order to compensate part or the total loss, yielding low or even null insertion loss values, such as Brillouin-based [139,141] or hybrid-based [144] approaches. In terms of size, reduced footprints in the scale of few mm^2 are reported by the integrated technologies, like SOI and III-V/SOI based approaches. In the next step, there are schemes involving mechanical parts, in the scale of cm^2 [146], and highly dispersive pigtails [87] and fibers [143] spanning from several centimetres to few kilometres. The central frequency in resonant-type structures, such as those based on micro-rings and micro-disks are limited by the notch depth properties, which are closely related to the power coupling status and the resonator loss. On the other hand, the central frequency given by PhC-based [145] or Brillouin-based [139, 141] approaches are at the end limited by the detector bandwidth. When using other approaches including SOAs [59], liquid crystals on Si (LCoS) [142] or MEMS [146], it depends on the semiconductor dynamics, the crystal properties or the design characteristics respectively. The operational bandwidth is mainly determined by the spectral range over which flat phase-shift or delay features can be implemented. For instance, by using SOA-based [59], FBG-based [87] or hybrid-based [144] approaches, bandwidths in the order of MHz or few GHz, few tens of GHz and detector-limited are respectively reached. Conversely, special designs like that based on frequency combs [143] are limited by the RF generator. Finally, the selectivity of both the band-pass or the rejection bands are associated with the number of taps and the Q-factor respectively.

In conclusion, depending on the filter spectral specifications and the requirements in terms of size, power consumption or tuning speed, a different technology platform becomes the most appropriate.

5.3 Open research lines

In this PhD work, the design and implementation of novel approaches with the aim at developing novel photonic-assisted RF signal processing tasks by exploiting SFL effects in different media have been performed. For this purpose, technology platforms such as semiconductor waveguides, SOI and III-V compounds based resonant-type structures have been used. However, some important issues are missing in this dissertation and they should be covered in near future research.

The phase-shifting/time-delaying functionalities demonstrated by using the three different technology platforms dealt with this thesis have been mainly exploited in the implementation of MWP tunable filters. However, other potential applications

such as tunable OEOs or controllable narrow-band optically-fed PAAs are readily feasible.

The SOA-based MWP phase shifter noise modelling proposed in this work accounts for all the noise sources involved in such structures for the static regime. Although the noise floor is accurately predicted even in presence of the microwave signal, a complete characterization should include the degradation caused by amplitude and phase fluctuations of the RF synthesizer, which are translated into noise contributions at the phase shifter output.

Commercially available SOAs based on bulk or MQW structures have been used in this work. However nano-engineered SOAs, like QDs, could greatly improve the performance of the cascaded SOA-based MWP phase shifters. In particular, properties such as a fast carrier recovery time, giant linewidth enhancement factor and low saturation power result in larger CPO bandwidth and efficiency, as well as low power consumption respectively. Consequently, larger phase-shifts over broader bandwidths could be implemented while reducing the total power consumption. Besides, the monolithically integrated version of the cascaded SOA-based MWP phase shifter should be fabricated and tested, paving the way towards miniaturization.

The E-SCT concept has been proposed for enlarging the aggregate bit rate in signal processors based on resonant-type structures. It is worthwhile to corroborate the theory with experimental results.

Straight waveguides, micro-ring and micro-disks resonators fabricated on different technologies have been investigated in this thesis. However, it would be worthwhile researching new device geometries, such as PhC waveguides with embedded QDs or PhC ring-type waveguides. Moreover, the study of all the geometries fabricated on more exotic materials belonging to groups III-V could be also interesting. Unique properties in the context of nonlinear effects and dispersive features could be obtained.

The operating bit rate of III-V-on-Si MDR based EOPMs are limited by the parasitic effects in the metal contacts. Therefore, the bit rate could be extended up to several tens of Gbps according to the carrier lifetime in InP compounds, by an optimized microwave design. Once this issue is overcome, special driving techniques could be additionally implemented to further extend the operating bit rate.

Optimize the power coupling factor between the nanophotonic Si waveguide and the InP disk cavity for the purpose of reaching over-coupling status at lower injection current and input optical power. This way customized devices in terms of power consumption could be accomplished.

Technology	Filter type	Bandpass/ rejected BW (GHZ)	Operating BW (GHZ)	Central frequency (GHZ)	Size scale (dB)	Insertion loss (dB)	Rejection level (dB)	Tuning time	Tuning range	Power
SOA (2.5)	Notch	0.02	2	20	cm^2	12	> 20	ps	100%	Medium
SOI (3.4.1)	Notch	0.01	1	20	mm^2	10	> 30	ms	77%	–
III-V/SOI (4.4.2)	Notch	0.01	1	20	μm^2	12	> 30	ps	100%	Medium
SOA [59]	Notch	0.001	0.03	30	mm	10	> 30	ps	100%	Medium
Brillouin [139]	Notch	0.1	PD limited	PD limited	km	0.5	> 30	μs	100%	High
SOI [140]	Notch	0.01	1	1.7	mm^2	10	> 25	ms	100%	–
3TNF-3000/4000-N/N	Notch	0.015	1	3–4	cm^2	0.5	> 40	s	29%	–
SOI (3.4.1)	Bandpass	0.04	1	20	mm^2	10	> 12	ms	24%	–
FBG [87]	Bandpass	0.5	20	6–7.5	cm	6	> 10	ms	70%	–
Brillouin [141]	Bandpass	0.02	PD limited	PD limited	km	0	> 30	μs	100%	High
LCoS [142]	Bandpass	0.3	< 20	2–3	cm	1.75	> 30	s	25%	–
Freq. comb. [143]	Bandpass	0.17–0.36	RF limited	5	km	1	> 60	ns	100%	–
Hybrid [144]	Bandpass	3–14	PD limited	9–37	mm^2	0	> 25	ps	58%	Medium
PhC [145]	Bandpass	8	> 40	> 40	mm	9	> 12	ms	100%	–
MEMS [146]	Bandpass	0.06	0.6	1.2–1.6	cm^2	4.1	> 15	ms	28%	Low
5BT-1800/2200-1S	Bandpass	0.02	0.4	1.8–2.2	cm^3	2	> 30	s	20%	–

Table 5.1: Comparison of the MW and MWP filters against the figures of merit.

Appendix A

Transfer function of the MDR

The set of differential equations modelling the propagation inside the cavity for all the three optical waves comprising $E_d(t,z)$ are defined in terms of a wave mixing description as

$$\frac{\partial E_{d,0}}{\partial z} = \gamma_0 E_{d,0}, \tag{A.1}$$

$$\frac{\partial E_{d,-1}}{\partial z} = \gamma_0 E_{d,-1} + \varepsilon_{-1}\left\{|E_{d,0}|^2 E_{d,-1} + {E_{d,0}}^2 E^*_{d,+1} e^{j\Delta kz}\right\}, \tag{A.2}$$

$$\frac{\partial E_{d,+1}}{\partial z} = \gamma_0 E_{d,+1} + \varepsilon_{+1}\left\{|E_{d,0}|^2 E_{d,+1} + {E_{d,0}}^2 E^*_{d,-1} e^{j\Delta kz}\right\}. \tag{A.3}$$

Eq. A.1 is first solved by applying the method of separation of variables:

$$\begin{aligned} &\int_{z=0}^{z=L} \frac{\partial E_{d,0}(z)}{E_{d,0}(z)} = \int_{z=0}^{z=L} \gamma_0 dz \rightarrow \frac{E_{d,0}(L)}{E_{d,0}(0)} = e^{\int_{z=0}^{z=L} \gamma_0 dz} \rightarrow \\ &E_{d,0}(L) = E_{d,0}(0)\, e^{F(L)}. \end{aligned} \tag{A.4}$$

On the other hand, Eq. A.1 can be written in terms of the optical intensity, S, as

$$\frac{\partial S}{\partial z} = (\gamma_0 + \gamma_0^*) S \rightarrow dz = \frac{dS}{(\gamma_0 + \gamma_0^*) S}. \tag{A.5}$$

A change of variables can be performed in Eq. A.1 and inserted into Eq. A.5

$$\frac{dE_{d,0}}{dS}(\gamma_0 + \gamma_0^*) S - \gamma_0 E_{d,0} = 0 \rightarrow \frac{dE_{d,0}}{E_{d,0}} = \frac{\gamma_0}{(\gamma_0 + \gamma_0^*) S} dS = F(z). \tag{A.6}$$

In this way, the common complex amplification factor $F(L)$ is calculated as:

$$F(L)=\int_{S(0)}^{S(L)}\frac{\gamma_0}{\left(\gamma_0+\gamma_0^*\right)S'}dS'=\int_{S(0)}^{S(L)}\frac{\frac{1}{2}\left[\frac{\Gamma g_0}{1+S'}(1-j\alpha)-a_{\text{int}}\right]}{\left(\frac{\Gamma g_0}{1+S'}-a_{\text{int}}\right)S'}dS'= \\ \int_{S(0)}^{S(L)}\frac{\frac{1}{2}[\Gamma g_0-j\alpha\Gamma g_0-a_{\text{int}}]}{(\Gamma g_0-a_{\text{int}}(1+S'))S'}dS'+\int_{S(0)}^{S(L)}\frac{-\frac{1}{2}a_{\text{int}}S'}{(\Gamma g_0-a_{\text{int}}(1+S'))S'}dS'=I1+I2. \tag{A.7}$$

By separately solving $I1$ and $I2$:

$$I1=\frac{1}{2}\frac{1-j\alpha-\frac{a_{\text{int}}}{\Gamma g_0}}{1-\frac{a_{\text{int}}}{\Gamma g_0}}\left\{\ln\left(\frac{S(L)}{S(0)}\right)-\ln\left(\frac{S(L)+1-\frac{\Gamma g_0}{a_{\text{int}}}}{S(0)+1-\frac{\Gamma g_0}{a_{\text{int}}}}\right)\right\}, \tag{A.8}$$

$$I2=\frac{1}{2}\ln\left(\frac{S(L)+1-\frac{\Gamma g_0}{a_{\text{int}}}}{S(0)+1-\frac{\Gamma g_0}{a_{\text{int}}}}\right). \tag{A.9}$$

Finally, the $F(L)$ can be written as:

$$F(L)=\frac{1}{2}\frac{1-j\alpha-\frac{a_{\text{int}}}{\Gamma g_0}}{1-\frac{a_{\text{int}}}{\Gamma g_0}}\ln\left(\frac{S(L)}{S(0)}\right)+\frac{1}{2}\frac{j\alpha}{1-\frac{a_{\text{int}}}{\Gamma g_0}}\ln\left(\frac{S(L)+1-\frac{\Gamma g_0}{a_{\text{int}}}}{S(0)+1-\frac{\Gamma g_0}{a_{\text{int}}}}\right). \tag{A.10}$$

Then, a new normalized complex amplitude $\tilde{E}_{d,\pm1}\rightarrow E_{d,\pm1}=\tilde{E}_{d,\pm1}e^{F(L)}$ is introduced. Moreover, by assuming that $|E_{d,0}(0)|=E_{d,0}(0)$ without loss of generality, Eqs. A.2 and A.3 can be reformulated as

$$\frac{\partial\tilde{E}_{d,-1}}{\partial z}=\varepsilon_{-1}\left(\tilde{E}_{d,-1}+E_{d,+1}^*\right)|E_{d,0}(z)|^2, \tag{A.11}$$

$$\frac{\partial\tilde{E}_{d,+1}}{\partial z}=\varepsilon_{+1}\left(\tilde{E}_{d,+1}+E_{d,-1}^*\right)|E_{d,0}(z)|^2. \tag{A.12}$$

By defining an extra pair of variables $u=\tilde{E}_{d,+1}+\tilde{E}_{d,-1}^*$ and $v=\tilde{E}_{d,+1}$ - $\tilde{E}_{d,-1}^*$, Eqs. A.11 and A.12 can be rewritten as:

$$\frac{du}{dz}=\left(\varepsilon_{+1}+\varepsilon_{-1}^*\right)|E_{d,0}(z)|^2u, \tag{A.13}$$

$$\frac{dv}{dz}=\left(\varepsilon_{+1}-\varepsilon_{-1}^*\right)|E_{d,0}(z)|^2u. \tag{A.14}$$

where

$$\varepsilon_{+1} + \varepsilon_{-1}^{*} = -\frac{1}{2}\frac{g_{sat}}{P_{sat}}\frac{1}{1+S-j\Omega\tau_s}, \tag{A.15}$$

$$\varepsilon_{+1} - \varepsilon_{-1}^{*} = \frac{1}{2}\frac{g_{sat}}{P_{sat}}\frac{2j\alpha}{1+S-j\Omega\tau_s}. \tag{A.16}$$

By taking into account that ε_{+1} - $\varepsilon_{-1}^{*} = -j\alpha(\varepsilon_{+1} + \varepsilon_{-1}^{*})$, $dz = dS$ / $[(\gamma_0 + \gamma_0^{*})S]$ and $S \approx |E_{d,0}|^2$ / P_{sat}, since small-signal modulation is assumed, then

$$\frac{du}{dS}\left(\gamma_0 + \gamma_0^{*}\right)S = \left(\varepsilon_{+1} + \varepsilon_{-1}^{*}\right)uP_{sat}S \rightarrow \frac{du}{dS} = \frac{\left(\varepsilon_{+1} + \varepsilon_{-1}^{*}\right)uP_{sat}}{\left(\gamma_0 + \gamma_0^{*}\right)}. \tag{A.17}$$

Now, the method of separation of variables can be used to solve A.17, so,

$$\begin{aligned} &\tfrac{du}{u} = \tfrac{\left(\varepsilon_{+1}+\varepsilon_{-1}^{*}\right)}{\gamma_0+\gamma_0^{*}}P_{sat}dS \rightarrow \tfrac{u(L)}{u(0)} = e^{\int_{S(0)}^{S(L)}\frac{\left(\varepsilon_{+1}+\varepsilon_{-1}^{*}\right)}{\gamma_0+\gamma_0^{*}}P_{sat}dS} \rightarrow \\ &u\left(L\right) = u\left(0\right)e^{G(L)}, \end{aligned} \tag{A.18}$$

where $G(L)$ corresponds to the gain grating related complex amplification factor. On the other hand,

$$\frac{dv}{dz} = -j\alpha\frac{du}{dz} \rightarrow v\left(L\right) = v\left(0\right) + j\alpha u\left(0\right)\left[1 - e^{G(L)}\right]. \tag{A.19}$$

Next, the term $G(L)$ must be obtained as

$$\begin{aligned} &G\left(L\right) = \int_{S(0)}^{S(L)} P_{sat}\tfrac{\left(\varepsilon_{+1}+\varepsilon_{-1}^{*}\right)}{\gamma_0+\gamma_0^{*}}dS' = -\int_{S(0)}^{S(L)}\tfrac{\frac{g_{sat}}{1+S'-j\Omega\tau s}}{g_{sat}-a_{\text{int}}}dS' = I1 + jI2 = \\ &-\tfrac{g_{sat}}{g_{sat}-a_{\text{int}}}\left\{\int_{S(0)}^{S(L)}\tfrac{1+S'}{(1+S')^2+(\Omega\tau_s)^2}dS' + j\int_{S(0)}^{S(L)}\tfrac{\Omega\tau_s}{(1+S')^2+(\Omega\tau_s)^2}dS'\right\}, \end{aligned} \tag{A.20}$$

by separately solving the integrals denoted as $I1$ and $I2$.

$$I1 = -\int_{S(0)}^{S(L)} \frac{\Gamma g_0}{\Gamma g_0 - a_{\text{int}}(1+S')} \frac{(1+S')}{(1+S')^2+(\Omega\tau_s)^2} dS' =$$

$$\frac{(\Gamma g_0)^2}{a_{\text{int}}^2(\Omega\tau_s)^2+(\Gamma g_0)^2} \left\{ \begin{array}{l} \ln\left(\frac{\frac{a_{\text{int}}}{\Gamma g_0}(1+S(L))-1}{\frac{a_{\text{int}}}{\Gamma g_0}(1+S(0))-1}\right) - \\ \\ \frac{1}{2}\ln\left(\frac{\left(\frac{1+S(L)}{\Omega\tau_s}\right)^2+1}{\left(\frac{1+S(0)}{\Omega\tau_s}\right)^2+1}\right) + \\ \\ \frac{a_{\text{int}}\Omega\tau_s}{\Gamma g_0}\left[\begin{array}{l} \arctan\left(\frac{1+S(L)}{\Omega\tau_s}\right) - \\ \arctan\left(\frac{1+S(0)}{\Omega\tau_s}\right) \end{array}\right] \end{array} \right\}, \tag{A.21}$$

$$I2 = -\int_{S(0)}^{S(L)} \frac{\Gamma g_0}{\Gamma g_0 - a_{\text{int}}(1+S')} \frac{\Omega\tau_s}{(1+S')^2+(\Omega\tau_s)^2} dS' =$$

$$\frac{(\Gamma g_0)^2}{a_{\text{int}}^2(\Omega\tau_s)^2+(\Gamma g_0)^2} \left\{ \begin{array}{l} \frac{a_{\text{int}}\Omega\tau_s}{\Gamma g_0}\ln\left(\frac{\frac{a_{\text{int}}}{\Gamma g_0}(1+S(L))-1}{\frac{a_{\text{int}}}{\Gamma g_0}(1+S(0))-1}\right) - \\ \\ \frac{1}{2}\frac{a_{\text{int}}\Omega\tau_s}{\Gamma g_0}\ln\left(\frac{\left(\frac{1+S(L)}{\Omega\tau_s}\right)^2+1}{\left(\frac{1+S(0)}{\Omega\tau_s}\right)^2+1}\right) - \\ \\ \arctan\left(\frac{1+S(L)}{\Omega\tau_s}\right) + \arctan\left(\frac{1+S(0)}{\Omega\tau_s}\right) \end{array} \right\}. \tag{A.22}$$

Finally, if the changes of variables are undone,

$$\tilde{E}_{d,+1} = \frac{u+v}{2} = \frac{1}{2}\left(v(0) + u(0)\left[j\alpha\left(1-e^{G(L)}\right) + e^{G(L)}\right]\right), \tag{A.23}$$

$$\tilde{E}^*_{d,-1} = \frac{u-v}{2} = \frac{1}{2}\left(-v(0) + u(0)\left[j\alpha\left(e^{G(L)}-1\right) + e^{G(L)}\right]\right), \tag{A.24}$$

the transfer functions for all the three optical waves are given by

$$H_0 = \frac{E_{d,0}(L)}{E_{d,0}(0)} = e^{F(L)}, \tag{A.25}$$

$$H_{+1} = \frac{E_{d,+1}(L)}{E_{d,+1}(0)} = \frac{1}{2}\left\{ \begin{array}{l} 1 + \frac{E^*_{d,-1}(0)}{E_{d,+1}(0)} e^{F(L)} e^{-F(L)^*}\left[j\alpha\left(1-e^{G(L)}\right) + e^{G(L)} - 1\right] \\ \\ + \left[j\alpha\left(1-e^{G(L)}\right) + e^{G(L)}\right] \end{array} \right\}, \tag{A.26}$$

$$H_{-1}^{*}=\frac{E_{d,-1}^{*}\left(L\right)}{E_{d,-1}^{*}\left(0\right)}=\frac{1}{2}\left\{\begin{array}{l} 1+\frac{E_{d,-1}(0)}{E_{d,-1}^{*}(0)}e^{-F(L)}e^{F(L)^{*}}\left[j\alpha\left(e^{G(L)}-1\right)+e^{G(L)}-1\right] \\ \\ +\left[j\alpha\left(e^{G(L)}-1\right)+e^{G(L)}\right] \end{array}\right\}. \tag{A.27}$$

Appendix B
List of publications

B.1 Journal papers

1. I. Gasulla, J. Sancho, **J. Lloret**, S. Sales and J. Capmany, "Harmonic distortion in microwave photonic phase shifters based on coherent population oscillations in SOAs", IEEE Photonics Technology Letters, vol. 22, no. 12, pp. 899-901, 2010.

2. **J. Lloret**, F. Ramos, J. Sancho, I. Gasulla, S. Sales and J. Capmany, "Noise spectrum characterization of slow light SOA-based microwave photonic phase shifters", IEEE Photonics Technology Letters, vol. 22, no. 13, pp. 1005-1007, 2010.

3. J. Sancho, S. Chin, M. Sagues, A. Loayssa, **J. Lloret**, I. Gasulla, S. Sales, L. Thévenaz and J. Capmany, "Dynamic microwave photonic filter using separate carrier tuning based on stimulated Brillouin scattering in Fibers", IEEE Photonics Technology Letters, vol. 22, no. 23, pp. 1753-1755, 2010.

4. I. Gasulla, J. Sancho, J. Capmany, **J. Lloret**, and S. Sales, "Intermodulation and harmonic distortion in slow light microwave photonic phase shifters based on coherent population oscillations in SOAs", Optics Express, vol. 18, no. 25, pp. 25677-25692, 2010.

5. **J. Lloret**, J. Sancho, I. Gasulla, S. Sales and J. Capmany, "Governing the speed of light and its application to the microwave photonics field", Waves, no. 2, pp. 30-38, 2010.

6. I. Gasulla, J. Capmany, J. Sancho, **J. Lloret**, S. Sales, "Application of slow and fast light effects to microwave photonics", Optica Pura y Aplicada, vol. 44, no.3, pp. 405-415, 2011.

7. **J. Lloret**, F. Ramos, W. Xue, J. Sancho, I. Gasulla, S. Sales, J. Mørk and J. Capmany, "The influence of optical filtering on the noise performance of microwave photonic phase shifters based on SOAs", IEEE Journal of Lightwave Technology, vol. 29, no. 12, pp. 1746-1752, 2011.

8. **J. Lloret**, J. Sancho, M. Pu, I. Gasulla, K. Yvind, S. Sales, and J. Capmany, "Tunable complex-valued multi-tap microwave photonic filter based on single silicon-on-insulator microring resonator", Optics Express, vol. 19, no. 13, pp. 12402-12407, 2011.

9. I. Gasulla, **J. Lloret**, J. Sancho, S. Sales and J. Capmany, "Recent breakthroughs in microwave photonics", IEEE Photonics Journal, vol. 3, no. 2, pp. 311-315, 2011.

10. J. Sancho, **J. Lloret**, I. Gasulla, S. Sales, and J. Capmany, "Fully tunable 360° microwave photonic phase shifter based on a single semiconductor optical amplifier", Optics Express, vol. 19, no. 18, pp. 17421-17426, 2011.

11. **J. Lloret**, R. Kumar, S. Sales, F. Ramos, G. Morthier, P. Mechet, T. Spuesens, D. Van Thourhout, N. Oliver, J.-M. Fédéli and J. Capmany, "Ultracompact electro-optical phase modulator based on III-V-on-silicon microdisk resonator", Optics Letters, vol. 37, no. 12, pp. 2379-2381, 2012.

12. J. Sancho, **J. Lloret**, I. Gasulla, S. Sales and J. Capmany, "Figures of merit for microwave photonic phase shifters based on semiconductor optical amplifiers", Optics Express, vol. 20, no. 10, pp. 10519-10525, 2012.

13. **J. Lloret**, G. Morthier, F. Ramos, S. Sales, D. Van Thourhout, T. Spuesens, N. Olivier J.-M. Fédéli and J. Capmany, "Broadband microwave photonic fully tunable filter using a single heterogeneously integrated III-V/SOI-microdisk-based phase shifter", Optics Express, vol. 20, no. 10, pp. 10796-10806, 2012.

14. J. Sancho, J. Bourderionnet, **J. Lloret**, G. Lehoucqa, P. Colmana, S. Xaviera, S. Sales, J. Capmany, S. Combrie and A. De Rossi, "Integrated microwave photonic crystal signal processor", submitted to Nature Photonics, 2012.

B.2 Conference papers

1. I. Gasulla, J. Sancho, **J. Lloret**, L. Yaron, S. Sales and J. Capmany, "Harmonic distortion in SOA based slow/fast light microwave photonic phase shifters", in IEEE Topical Meeting Microwave Photonics (MWP), Valencia (Spain), paper Th3.6, 2009.

2. I. Gasulla, J. Sancho, **J. Lloret**, S. Sales, and J. Capmany, "Harmonic distortion in slow light SOA based microwave photonic phase shifters", in Optical Fiber Communication Conference (OFC), San Diego (USA), paper JWA52, 2010.

3. **J. Lloret**, F. Ramos, J. Sancho, I. Gasulla, S. Sales and J. Capmany, "On the noise performance of slow light SOA-based microwave photonic phase shifters", in IEEE Topical Meeting Microwave Photonics (MWP), Montreal (Canada), paper TH4-28, 2010.

4. I. Gasulla, J. Sancho, **J. Lloret**, S. Sales and J. Capmany, "Figures of merit for microwave photonic phase shifters based on coherent population oscillation slow and fast light effects", in 12th International Conference on Transparent Optical Networks (ICTON), Munich (Germany), invited paper We.B3.2, 2010.

5. I. Gasulla, J. Sancho, **J. Lloret**, S. Sales, and J. Capmany, "On the use of slow light effects for tunable and reconfigurable microwave photonic filters", in 2nd Mediterranean Photonics Conference, Eilat (Israel), invited paper, 2010.

6. J. Sancho, S. Chin, M. Sagues, A. Loayssa, **J. Lloret**, I. Gasulla, S. Sales, L. Thévenaz and J. Capmany, "True time delay on tunable microwave photonic filter based on stimulated Brillouin scattering in fibers", in 36th European Conference of Optical Communication (ECOC), Turin (Italy), paper P.1.18, 2010.

7. **J. Lloret**, J. Sancho, I. Gasulla, F. Ramos, S. Sales, and J. Capmany, "Noise figure of slow light cascaded SOA based microwave photonic phase shifters", in Slow and Fast Light conference (SL), Toronto (Canada), paper SLWB5, 2011. *Awarded with a registration waiver granted by the Canadian Air Force Office of Scientific Research (AFOSR).*

8. J. Sancho, **J. Lloret**, I. Gasulla, S. Sales, and J. Capmany, "Microwave photonics applications using slow and fast light effects", in Slow and Fast Light conference (SL), Toronto (Canada), invited paper SLMA5, 2011.

9. **J. Lloret**, J. Sancho, I. Gasulla, S. Sales, and J. Capmany, "Performance metrics evaluation of cascaded SOA based slow light microwave photonic phase shifters", in IEEE Topical Meeting Microwave Photonics (MWP), Singapore

(Singapore), paper 2175, 2011.

10. **J. Lloret**, J. Sancho, I. Gasulla, S. Sales, and J. Capmany, "Complex-coefficient microwave photonic tunable filter using slow light silicon-on-insulator-based microring resonator", in IEEE Topical Meeting Microwave Photonics (MWP), Singapore (Singapore),paper 2167, 2011.

11. J. Sancho, **J. Lloret**, I. Gasulla, S. Sales, and J. Capmany, "2π microwave photonic phase shifter based on single semiconductor optical amplifier", in IEEE Topical Meeting Microwave Photonics (MWP), Singapore (Singapore),paper 2181, 2011.

12. J. Sancho, I. Gasulla, **J. Lloret**, S. Sales, and J. Capmany, "Third order intermodulation distortion in a 360 microwave photonic phase shifter based on slow light cascaded SOAs", in International Conference on Information Photonics (IP), Ottawa (Canada), paper 5953771, 2011.

13. **J. Lloret**, J. Sancho, I. Gasulla, S. Sales and J. Capmany, "True time delays and phase shifters based on slow light technologies for microwave photonics applications", in 13th International Conference on Transparent Optical Networks (ICTON), Stockholm (Sweden), invited paper 5971119, 2011.

14. I. Gasulla, J. Sancho, J. Capmany, **J. Lloret**, and S. Sales, "Intermodulation and harmonic distortion in slow light SOA based microwave photonic phase shifters", in Optical Fiber Communication Conference (OFC), Los Angeles (USA), paper JWA051, 2011.

15. **J. Lloret**, F. Ramos, S. Sales, J. Capmany, G. Morthier, D. Van Thourhout, T. Spuesens, N. Olivier and J.-M. Fédéli, "Fully tunable microwave photonic phase shifter for broadband signals based on a single heterogeneously integrated III-V-on-Silicon microdisk resonator", in European Conference on Optical Integration (ECIO), Sitges (Spain), paper 158, 2012.

16. J. Sancho, **J. Lloret**, N. Primerov, S. Sales, L. Thévenaz and J. Capmany, "Recent implementations of fiber and integrated tunable microwave photonics filters", submitted to the 14th International Conference on Transparent Optical Networks (ICTON), Coventry (England), 2012.

17. J. Sancho, **J. Lloret**, J. Bourderionnet, G. Lehoucqa, P. Colmana, S. Xaviera, A. De Rossi, D. Dolfi, S. Sales and J. Capmany, "Microwave photonic signal processor based on an integrated dispersive delay line", submitted to IEEE Topical Meeting Microwave Photonics (MWP), Noordwijk (The Netherlands), 2012.

Bibliography

[1] A. Seeds, "Microwave photonics," *Microwave Theory and Techniques, IEEE Transactions on*, vol. 50, pp. 877–887, Mar 2002.

[2] J. Capmany and D. Novak, "Microwave photonics combines two worlds," *Nature Photonics*, vol. 1, pp. 319–330, 2007.

[3] J. Yao, "Microwave photonics," *Lightwave Technology, Journal of*, vol. 27, pp. 314–335, Feb 2009.

[4] R. Tucker, P.-C. Ku, and C. Chang-Hasnain, "Slow-light optical buffers: capabilities and fundamental limitations," *Lightwave Technology, Journal of*, vol. 23, pp. 4046–4066, Dec 2005.

[5] J. Capmany, I. Gasulla, and S. Sales, "Harnessing slow light," *Nature Photonics*, vol. 5, pp. 731–733, Dec 2011.

[6] M. Santagiustina, G. Eisenstein, L. Thevenaz, J. Capmany, J. Mork, J. Reithmaier, A. De Rossi, S. Sales, K. Yvind, S. Combrie, and J. Bourderionnet, "Slow light devices and their applications to microwaves and photonics," *IEEE Photonics Society Newsletter*, vol. 26, no. 1, pp. 5–12, 2012.

[7] R. W. Boyd and D. J. Gauthier, "Controlling the velocity of light pulses," *Science*, vol. 326, pp. 1074–1077, Nov 2009.

[8] J. Khurgin and R. S. Tucker, *Slow Light: Science and Applications*. CRC Press, 2008.

[9] A. Yariv, *Quantum Electronics*. Wiley, 3 ed., Jan 1989.

[10] L. V. Hau, S. E. Harris, Z. Dutton, and C. H. Behroozi, "Light speed reduction to 17 metres per second in an ultracold atomic gas," *Nature*, vol. 397, pp. 594–598, Feb 1999.

[11] C. J. Chang-Hasnain and S. L. Chuang, "Slow and fast light in semiconductor quantum-well and quantum-dot devices," *Lightwave Technology, Journal of*, vol. 24, pp. 4642–4654, Dec 2006.

[12] P. Lunnemann and J. Mork, "Reducing the impact of inhomogeneous broadening on quantum dot based electromagnetically induced transparency," *Applied Physics Letters*, vol. 94, no. 7, p. 071108, 2009.

[13] P.-C. Ku, F. Sedgwick, C. J. Chang-Hasnain, P. Palinginis, T. Li, H. Wang, S.-W. Chang, and S.-L. Chuang, "Slow light in semiconductor quantum wells," *Opt. Lett.*, vol. 29, pp. 2291–2293, Oct 2004.

[14] J. Mork, P. Lunnenmann, W. Xue, Y. Chen, P. Kaer, and T. R. Nielsen, "Slow and fast light in semiconductor waveguides," *Semiconductor Science and Technology*, vol. 25, p. 83002, Jul 2010.

[15] J. Mork, R. Kjær, M. van der Poel, and K. Yvind, "Slow light in a semiconductor waveguide at gigahertz frequencies," *Opt. Express*, vol. 13, pp. 8136–8145, Oct 2005.

[16] H. Su, P. Kondratko, and S. L. Chuang, "Variable optical delay using population oscillation and four-wave-mixing in semiconductor optical amplifiers," *Opt. Express*, vol. 14, pp. 4800–4807, May 2006.

[17] L. Thévenaz, "Slow and fast light in optical fibres," *Nature Photonics*, vol. 2, pp. 474–481, 2008.

[18] K. Y. Song, M. Herráez, and L. Thévenaz, "Observation of pulse delaying and advancement in optical fibers using stimulated brillouin scattering," *Opt. Express*, vol. 13, pp. 82–88, Jan 2005.

[19] D. Dahan and G. Eisenstein, "Tunable all optical delay via slow and fast light propagation in a raman assisted fiber optical parametric amplifier: A route to all optical buffering," *Opt. Express*, vol. 13, pp. 6234–6249, Aug 2005.

[20] Y. Okawachi, M. Foster, J. Sharping, A. Gaeta, Q. Xu, and M. Lipson, "All-optical slow-light on a photonic chip," *Opt. Express*, vol. 14, pp. 2317–2322, Mar 2006.

[21] M. Santagiustina, "Electromagnetic energy velocity in slow light," in *Slow and Fast Light*, p. SLTuB5, Optical Society of America, 2011.

[22] J. B. Khurgin and P. A. Morton, "Tunable wideband optical delay line based on balanced coupled resonator structures," *Opt. Lett.*, vol. 34, pp. 2655–2657, Sep 2009.

[23] T. Baba, "Slow light in photonic crystals," *Nature Photonics*, vol. 2, no. 8, pp. 465–473, 2008.

[24] T. F. Krauss, "Slow light in photonic crystal waveguides," *Journal of Physics D: Applied Physics*, vol. 40, pp. 2666–2670, Apr 2007.

[25] T. F. Krauss, "Why do we need slow light?," *Nature Photonics*, vol. 2, pp. 448–450, 2008.

[26] I. Gasulla, J. Lloret, J. Sancho, S. Sales, and J. Capmany, "Recent breakthroughs in microwave photonics," *IEEE Photonics Journal*, vol. 3, pp. 311–315, 2010.

[27] J. Capmany, B. Ortega, and D. Pastor, "A tutorial on microwave photonic filters," *Lightwave Technology, Journal of*, vol. 24, pp. 201–229, Jan 2006.

[28] R. J. Mailloux, *Phased Array Antenna Handbook, Second Edition*. Artech House Publishers, 2 ed., Mar 2005.

[29] C. Chang-Hasnain, P.-C. Ku, J. Kim, and S.-L. Chuang, "Variable optical buffer using slow light in semiconductor nanostructures," *Proceedings of the IEEE*, vol. 91, pp. 1884–1897, Nov 2003.

[30] P. Palinginis, F. Sedgwick, S. Crankshaw, M. Moewe, and C. Chang-Hasnain, "Room temperature slow light in a quantum-well waveguide via coherent population oscillation," *Opt. Express*, vol. 13, pp. 9909–9915, Nov 2005.

[31] F. Öhman, K. Yvind, and J. Mørk, "Slow light in a semiconductor waveguide for true-time delay applications in microwave photonics," *Photonics Technology Letters, IEEE*, vol. 19, pp. 1145–1147, Aug 2007.

[32] W. Xue, S. Sales, J. Capmany, and J. Mork, "Microwave phase shifter with controllable power response based on slow- and fast-light effects in semiconductor optical amplifiers," *Opt. Lett.*, vol. 34, pp. 929–931, Apr 2009.

[33] S. Sales, W. Xue, J. Mork, and I. Gasulla, "Slow and fast light effects and their applications to microwave photonics using semiconductor optical amplifiers," *Microwave Theory and Techniques, IEEE Transactions on*, vol. 58, pp. 3022–3038, Nov 2010.

[34] W. Xue, Y. Chen, F. Ohman, S. Sales, and J. Mork, "Enhancing light slowdown in semiconductor optical amplifiers by optical filtering," *Optics Letters*, vol. 33, pp. 1084–1086, May 2008.

[35] W. Xue, S. Sales, J. Capmany, and J. Mork, "Wideband 360° microwave photonic phase shifter based on slow light in semiconductor optical amplifiers," *Opt. Express*, vol. 18, pp. 6156–6163, Mar 2010.

[36] W. Xue and J. Mork, "Tunable true-time delay of a microwave photonic signal realized by cross gain modulation in a semiconductor waveguide," *Applied Physics Letters*, vol. 99, p. 231102, Dec 2011.

[37] P. Berger, J. Bourderionnet, F. Bretenaker, D. Dolfi, and M. Alouini, "Time delay generation at high frequency using SOA based slow and fast light," *Opt. Express*, vol. 19, pp. 21180–21188, Oct 2011.

[38] A. Uskov, J. Mørk, and J. Mark, "Wave mixing in semiconductor laser amplifiers due to carrier heating and spectral-hole burning," *Quantum Electronics, IEEE Journal of*, vol. 30, pp. 1769–1781, Aug 1994.

[39] A. P. Bogatov, P. G. Eliseev, O. G. Okhotnikov, M. P. Rakhvalskii, and K. A. Khairetdinov, "Interaction of modes and self-stabilization of single-frequency emission from injection lasers," *Soviet Journal of Quantum Electronics*, vol. 13, no. 9, p. 1221, 1983.

[40] A. Uskov and C. Chang-Hasnain, "Slow and superluminal light in semiconductor optical amplifiers," *Electronics Letters*, vol. 41, pp. 55–56, Aug 2005.

[41] Y. Chen, W. Xue, F. Ohman, and J. Mork, "Theory of optical-filtering enhanced slow and fast light effects in semiconductor optical waveguides," *Lightwave Technology, Journal of*, vol. 26, pp. 3734–3743, Dec 2008.

[42] E. Shumakher, S. O. Dúill, and G. Eisenstein, "Signal-to-noise ratio of a semiconductor optical-amplifier-based optical phase shifter," *Opt. Lett.*, vol. 34, pp. 1940–1942, Jul 2009.

[43] C. H. Cox, *Analog Optical Links: Theory and Practice*. 2004.

[44] I. Gasulla, J. Sancho, J. Lloret, S. Sales, and J. Capmany, "Figures of merit for microwave photonic phase shifters based on coherent population oscillation slow and fast light effects," in *International Conference on Transparent Optical Networks*, 2010.

[45] J. Sancho, J. Lloret, I. Gasulla, S. Sales, and J. Capmany, "Figures of merit for microwave photonic phase shifters based on semiconductor optical amplifiers," *Opt. Express*, vol. 20, pp. 10519–10525, May 2012.

[46] S. O. Dúill, E. Shumakher, and G. Eisenstein, "Noise properties of microwave phase shifters based on semiconductor optical amplifiers," *J. Lightwave Technol.*, vol. 28, pp. 791–797, Mar 2010.

[47] P. Berger, J. Bourderionnet, M. Alouini, F. Bretenaker, and D. Dolfi, "Theoretical study of the spurious-free dynamic range of a tunable delay line based on slow light in SOA," *Opt. Express*, vol. 17, pp. 20584–20597, Oct 2009.

[48] I. Gasulla, J. Sancho, J. Capmany, J. Lloret, and S. Sales, "Intermodulation and harmonic distortion in slow light microwave photonic phase shifters based on coherent population oscillations in SOAs," *Opt. Express*, vol. 18, pp. 25677–25692, Dec 2010.

[49] I. Gasulla, J. Sancho, J. Lloret, S. Sales, and J. Capmany, "Harmonic distortion in microwave photonic phase shifters based on coherent population oscillations in SOAs," *Photonics Technology Letters, IEEE*, vol. 22, pp. 899–901, Jun 2010.

[50] T. Mukai and Y. Yamamoto, "Noise characteristics of semiconductor laser amplifiers," *Electronics Letters*, vol. 17, pp. 31–33, Aug 1981.

[51] M. Shtaif and G. Eisenstein, "Noise properties of nonlinear semiconductor optical amplifiers," *Optics Letters*, vol. 22, pp. 1851–1853, 1996.

[52] A. Bilenca and G. Eisenstein, "Fokker-Planck and Langevin analyses of noise accompanying the amplification of optical pulses in semiconductor optical amplifiers," *Journal of Optical Society of America B*, vol. 22, pp. 1632–1639, 2005.

[53] M. Shtaif, B. Tromborg, and G. Eisenstein, "Noise spectra of semiconductor optical amplifiers: Relation between semiclassical and quantum descriptions," *Quantum Electronics, IEEE Journal of*, vol. 34, pp. 869–878, May 1998.

[54] P. Berger, M. Alouini, J. Bourderionnet, F. Bretenaker, and D. Dolfi, "Slow light using semiconductor optical amplifiers: Model and noise characteristics," *Comptes Rendus Physique*, vol. 10, pp. 991–999, 2009.

[55] B. Eggleton, G. Lenz, N. Litchinitser, D. Patterson, and R. Slusher, "Implications of fiber grating dispersion for WDM communication systems," *Photonics Technology Letters, IEEE*, vol. 9, pp. 1403–1405, Oct 1997.

[56] J. Capmany, D. Pastor, and B. Ortega, "RIN induced by out-band dispersion in fibre bragg grating based add-drop multiplexers," *Electronics Letters*, vol. 35, pp. 2220–2221, Dec 1999.

[57] S. O. Dúill, E. Shumakher, and G. Eisenstein, "The role of optical filtering in microwave phase shifting," *Optics Letters*, vol. 35, pp. 2278–2280, Jul 2010.

[58] S. O. Dúill, E. Shumakher, and G. Eisenstein, "Large-signal operation of a semiconductor optical amplifier as a phase-shifting element for microwave signals," *Photonics Technology Letters, IEEE*, vol. 21, pp. 679–681, Jun 2009.

[59] W. Xue, S. Sales, J. Mork, and J. Capmany, "Widely tunable microwave photonic notch filter based on slow and fast light effects," *Photonics Technology Letters, IEEE*, vol. 21, pp. 167–169, Feb 2009.

[60] G. T. Reed, *Silicon Photnics: The State of the Art.* John Wiley & Sons, Ltd, 2008.

[61] R. Soref and J. Lorenzo, "Single-crystal silicon: A new material for 1.3 and 1.6 μm integrated-optical components," *Electronics Letters*, vol. 21, pp. 953–954, Oct 1985.

[62] R. Soref and J. Lorenzo, "All-silicon active and passive guided-wave components for $\lambda = 1.3$ and 1.6 μm," *Quantum Electronics, IEEE Journal of*, vol. 22, pp. 873–879, Jun 1986.

[63] R. Soref, "Silicon-based optoelectronics," *Proceedings of the IEEE*, vol. 81, pp. 1687–1706, Dec 1993.

[64] G. T. Reed and A. P. Knights, *Silicon Photonics: An Introduction.* John Wiley, 2004.

[65] B. Jalali and S. Fathpour, "Silicon photonics," *J. Lightwave Technol.*, vol. 24, pp. 4600–4615, Dec 2006.

[66] M. Lipson, "Guiding, modulating, and emitting light on Silicon - challenges and opportunities," *Lightwave Technology, Journal of*, vol. 23, pp. 4222–4238, Dec 2005.

[67] G. T. Reed, G. Mashanovich, F. Y. Gardes, and D. J. Thomson, "Silicon optical modulators," *Nature Photonics*, vol. 4, pp. 518–526, Jul 2010.

[68] D. Liang and J. E. Bowers, "Recent progress in lasers on silicon," *Nature Photonics*, vol. 4, pp. 511–517, July 2010.

[69] J. Michel, J. Liu, and L. C. Kimerling, "High-performance Ge-on-Si photodetectors," *Nature Photonics*, vol. 4, pp. 527–534, Jul 2010.

[70] M. Gnan, S. Thorns, D. Macintyre, R. De La Rue, and M. Sorel, "Fabrication of low-loss photonic wires in silicon-on-insulator using hydrogen silsesquioxane electron-beam resist," *Electronics Letters*, vol. 44, pp. 115–116, Jan 2008.

[71] L. Liao, A. Liu, J. Basak, H. Nguyen, M. Paniccia, D. Rubin, Y. Chetrit, R. Cohen, and N. Izhaky, "40 Gbit/s silicon optical modulator for high-speed applications," *Electronics Letters*, vol. 43, Oct 2007.

[72] D. Gill, M. Rasras, K.-Y. Tu, Y.-K. Chen, A. White, S. Patel, D. Carothers, A. Pomerene, R. Kamocsai, C. Hill, and J. Beattie, "Internal bandwidth equalization in a CMOS-compatible Si-ring modulator," *Photonics Technology Letters, IEEE*, vol. 21, pp. 200–202, Feb 2009.

[73] H. Rong, R. Jones, A. Liu, O. Cohen, D. Hak, A. Fang, and M. Paniccia, "A continuous-wave raman silicon laser," *Nature*, vol. 433, pp. 725–728, Feb 2005.

[74] H. Rong, A. Liu, R. Jones, O. Cohen, D. Hak, R. Nicolaescu, A. Fang, and M. Paniccia, "An all-silicon raman laser," *Nature*, vol. 433, pp. 292–294, Jan 2005.

[75] T. K. Liang and H. K. Tsang, "Efficient raman amplification in silicon-on-insulator waveguides," *Applied Physics Letters*, vol. 85, pp. 3343–3345, Aug 2004.

[76] R. Claps, D. Dimitropoulos, V. Raghunathan, Y. Han, and B. Jalali, "Observation of stimulated raman amplification in silicon waveguides," *Opt. Express*, vol. 11, pp. 1731–1739, Jul 2003.

[77] H. Park, Y.-H. Kuo, A. W. Fang, R. Jones, O. Cohen, M. J. Paniccia, and J. E. Bowers, "A hybrid AlGaInAs-silicon evanescent preamplifier and photodetector," *Opt. Express*, vol. 15, pp. 13539–13546, Oct 2007.

[78] D. Dolfi, P. Joffre, J. Antoine, J.-P. Huignard, D. Philippet, and P. Granger, "Experimental demonstration of a phased-array antenna optically controlled with phase and time delays," *Appl. Opt.*, vol. 35, pp. 5293–5300, Sep 1996.

[79] J. Capmany, B. Ortega, D. Pastor, and S. Sales, "Discrete-time optical processing of microwave signals," *Lightwave Technology, Journal of*, vol. 23, pp. 702–723, Feb 2005.

[80] R. Minasian, "Photonic signal processing of microwave signals," *Microwave Theory and Techniques, IEEE Transactions on*, vol. 54, pp. 832–846, Feb 2006.

[81] G. Cocorullo and I. Rendina, "Thermo-optical modulation at 1.5 μm in silicon etalon," *Electronics Letters*, vol. 28, pp. 83–85, Jan 1992.

[82] M. Pu, L. Liu, W. Xue, Y. Ding, L. Frandsen, H. Ou, K. Yvind, and J. Hvam, "Tunable microwave phase shifter based on silicon-on-insulator microring resonator," *Photonics Technology Letters, IEEE*, vol. 22, pp. 869–871, Jun 2010.

[83] M. Pu, L. Liu, W. Xue, Y. Ding, H. Ou, K. Yvind, and J. M. Hvam, "Widely tunable microwave phase shifter based on silicon-on-insulator dual-microring resonator," *Opt. Express*, vol. 18, pp. 6172–6182, Mar 2010.

[84] J. Heebner, V. Wong, A. Schweinsberg, R. Boyd, and D. Jackson, "Optical transmission characteristics of fiber ring resonators," *Quantum Electronics, IEEE Journal of*, vol. 40, pp. 726–730, Jun 2004.

[85] D. Adams and C. Madsen, "A novel broadband photonic RF phase shifter," *Lightwave Technology, Journal of*, vol. 26, pp. 2712–2717, Aug 2008.

[86] Q. Chang, Q. Li, Z. Zhang, M. Qiu, T. Ye, and Y. Su, "A tunable broadband photonic RF phase shifter based on a silicon microring resonator," *Photonics Technology Letters, IEEE*, vol. 21, pp. 60–62, Jan 2009.

[87] M. Sagues, R. G. Olcina, A. Loayssa, S. Sales, and J. Capmany, "Multi-tap complex-coefficient incoherent microwave photonic filters based on optical single-sideband modulation and narrow band optical filtering," *Opt. Express*, vol. 16, pp. 295–303, Jan 2008.

[88] R. Fortenberry, "Enhanced wavelength resolution chromatic dispersion measurements using fixed sideband technique," in *Optical Fiber Communication Conference, 2000*, vol. 1, pp. 107 –109, 2000.

[89] F. Harris, "On the use of windows for harmonic analysis with the discrete Fourier transform," *Proceedings of the IEEE*, vol. 66, pp. 51–83, Jan 1978.

[90] J. Heebner and R. Boyd, "Slow and fast light in resonator-coupled waveguides," *Journal of Modern Optics*, vol. 49, pp. 2629–2636, Mar 2002.

[91] F. Xia, L. Sekaric, and Y. Vlasov, "Ultracompact optical buffers on a silicon chip," *Nature Photonics*, vol. 1, pp. 65–71, Dec 2006.

[92] J. D. Doménech, P. Munoz, and J. Capmany, "Transmission and group-delay characterization of coupled resonator optical waveguides apodized through the longitudinal offset technique," *Opt. Lett.*, vol. 36, pp. 136–138, Jan 2011.

[93] J. Cardenas, M. A. Foster, N. Sherwood-Droz, C. B. Poitras, H. L. R. Lira, B. Zhang, A. L. Gaeta, J. B. Khurgin, P. Morton, and M. Lipson, "Wide-bandwidth continuously tunable optical delay line using silicon microring resonators," *Opt. Express*, vol. 18, pp. 26525–26534, Dec 2010.

[94] P. Morton and J. Khurgin, "Microwave photonic delay line with separate tuning of the optical carrier," *Photonics Technology Letters, IEEE*, vol. 21, pp. 1686–1688, Nov 2009.

[95] M. C. Wu, O. Solgaard, and J. E. Ford, "Optical MEMS for lightwave communication," *Lightwave Technology, Journal of*, vol. 24, pp. 4433–4454, Dec 2006.

[96] J. Proakis, *Digital Communications*. McGraw-Hill, 4th ed., Nov 2000.

[97] H. H. Li, "Refractive index of silicon and germanium and its wavelength and temperature derivatives," *Journal of Physical and Chemical Reference Data*, vol. 9, no. 3, p. 561, 1980.

[98] I. Kiyat, A. Aydinli, and N. Dagli, "Low-power thermooptical tuning of SOI resonator switch," *Photonics Technology Letters, IEEE*, vol. 18, pp. 364–366, Jan 2006.

[99] J. Teng, P. Dumon, W. Bogaerts, H. Zhang, X. Jian, X. Han, M. Zhao, G. Morthier, and R. Baets, "Athermal silicon-on-insulator ring resonators by overlaying a polymer cladding on narrowedwaveguides," *Opt. Express*, vol. 17, pp. 14627–14633, Aug 2009.

[100] R. Soref, "The past, present, and future of silicon photonics," *Selected Topics in Quantum Electronics, IEEE Journal of*, vol. 12, pp. 1678–1687, Dec 2006.

[101] Y. Kang, H.-D. Liu, M. Morse, M. J. Paniccia, M. Zadka, S. Litski, G. Sarid, A. Pauchard, Y.-H. Kuo, H.-W. Chen, W. S. Zaoui, J. E. Bowers, A. Beling, D. C. McIntosh, X. Zheng, and J. C. Campbell, "Monolithic germanium/silicon avalanche photodiodes with a 340 GHz gain bandwidth product," *Nature Photonics*, vol. 3, pp. 59–63, Dec 2008.

[102] H. Park, A. Fang, S. Kodama, and J. Bowers, "Hybrid silicon evanescent laser fabricated with a silicon waveguide and III-V offset quantum wells," *Opt. Express*, vol. 13, pp. 9460–9464, Nov 2005.

[103] H. Park, M. Sysak, H.-W. Chen, A. Fang, D. Liang, L. Liao, B. Koch, J. Bovington, Y. Tang, K. Wong, M. Jacob-Mitos, R. Jones, and J. Bowers, "Device and integration technology for silicon photonic transmitters," *Selected Topics in Quantum Electronics, IEEE Journal of*, vol. 17, pp. 671–688, Jun 2011.

[104] S. Srinivasan, A. W. Fang, D. Liang, J. Peters, B. Kaye, and J. E. Bowers, "Design of phase-shifted hybrid silicon distributed feedback lasers," *Opt. Express*, vol. 19, pp. 9255–9261, May 2011.

[105] G. Roelkens, D. V. Thourhout, R. Baets, R. Notzel, and M. Smit, "Laser emission and photodetection in an InP/InGaAsP layer integrated on and coupled to a silicon-on-insulator waveguide circuit," *Opt. Express*, vol. 14, pp. 8154–8159, Sep 2006.

[106] J. V. Campenhout, P. R. Romeo, P. Regreny, C. Seassal, D. V. Thourhout, S. Verstuyft, L. D. Cioccio, J.-M. Fedeli, C. Lagahe, and R. Baets, "Electrically pumped InP-based microdisk lasers integrated with a nanophotonic silicon-on-insulator waveguide circuit," *Opt. Express*, vol. 15, pp. 6744–6749, May 2007.

[107] J. Van Campenhout, P. Romeo, D. Van Thourhout, C. Seassal, P. Regreny, L. Di Cioccio, J.-M. Fedeli, and R. Baets, "Design and optimization of electrically injected InP-based microdisk lasers integrated on and coupled to a SOI waveguide circuit," *Lightwave Technology, Journal of*, vol. 26, pp. 52–63, Jan 2008.

[108] L. Liu, T. Spuesens, G. Roelkens, D. Van Thourhout, P. Regreny, and P. Rojo-Romeo, "A thermally tunable III-V compound semiconductor microdisk laser integrated on Silicon-on-Insulator circuits," *Photonics Technology Letters, IEEE*, vol. 22, pp. 1270–1272, Sep 2010.

[109] J. Van Campenhout, L. Liu, P. Romeo, D. Van Thourhout, C. Seassal, P. Regreny, L. Di Cioccio, J.-M. Fedeli, and R. Baets, "A compact SOI-integrated multiwavelength laser source based on cascaded InP microdisks," *Photonics Technology Letters, IEEE*, vol. 20, pp. 1345–1347, Aug 2008.

[110] R. Kumar, L. Liu, G. Roelkens, E.-J. Geluk, T. de Vries, F. Karouta, P. Regreny, D. Van Thourhout, R. Baets, and G. Morthier, "10-GHz all-optical gate based on a III-V/SOI microdisk," *Photonics Technology Letters, IEEE*, vol. 22, pp. 981–983, Jul 2010.

[111] D. Van Thourhout, T. Spuesens, S. Selvaraja, L. Liu, G. Roelkens, R. Kumar, G. Morthier, P. Rojo-Romeo, F. Mandorlo, P. Regreny, O. Raz, C. Kopp, and L. Grenouillet, "Nanophotonic devices for optical interconnect," *Selected Topics in Quantum Electronics, IEEE Journal of*, vol. 16, pp. 1363–1375, Oct 2010.

[112] L. Liu, J. V. Campenhout, G. Roelkens, D. V. Thourhout, P. Rojo-Romeo, P. Regreny, C. Seassal, J.-M. Fedeli, and R. Baets, "Ultralow-power all-optical wavelength conversion in a silicon-on-insulator waveguide based on a heterogeneously integrated III-V microdisk laser," *Applied Physics Letters*, vol. 93, p. 061107, Jun 2008.

[113] R. Kumar, T. Spuesens, P. Mechet, P. Kumar, O. Raz, N. Olivier, J.-M. Fedeli, G. Roelkens, R. Baets, D. V. Thourhout, and G. Morthier, "Ultrafast and bias-free all-optical wavelength conversion using III-V-on-silicon technology," *Opt. Lett.*, vol. 36, pp. 2450–2452, Jul 2011.

[114] G. Roelkens, D. Van Thourhout, and R. Baets, "Coupling schemes for heterogeneous integration of III-V membrane devices and silicon-on-insulator waveguides," *Lightwave Technology, Journal of*, vol. 23, pp. 3827–3831, Nov 2005.

[115] P. Binetti, R. Orobtchouk, X. Leijtens, B. Han, T. de Vries, Y.-S. Oei, L. Di Cioccio, J.-M. Fedeli, C. Lagahe, P. van Veldhoven, R. Notzel, and M. Smit, "InP-based membrane couplers for optical interconnects on Si," *Photonics Technology Letters, IEEE*, vol. 21, pp. 337–339, Mar 2009.

[116] L. Liu, R. Kumar, K. Huybrechts, T. Spuesens, G. Roelkens, E.-J. Geluk, T. de Vries, P. Regreny, D. Van Thourhout, R. Baets, and G. Morthier, "An ultra-small, low-power, all-optical flip-flop memory on a silicon chip," *Nature Photonics*, vol. 4, pp. 182–187, Jan 2010.

[117] L. Liu, J. V. Campenhout, G. Roelkens, R. A. Soref, D. V. Thourhout, P. Rojo-Romeo, P. Regreny, C. Seassal, J.-M. Fédéli, and R. Baets, "Carrier-injection-based electro-optic modulator on silicon-on-insulator with a heterogeneously integrated III-V microdisk cavity," *Opt. Lett.*, vol. 33, pp. 2518–2520, Nov 2008.

[118] G. Morthier, R. Kumar, P. Mechet, T. Spuessens, L. Liu, K. Huybrechts, G. Roelkens, J. V. Campenhout, D. V. Thourhout, and R. Baets, "Microdisk lasers heterogeneously integrated on silicon for low-power, high-speed optical switching," *IEEE Photonics Society Newsletter*, vol. 24, pp. 5–10, Jun 2010.

[119] G. P. Agrawal, *Lightwave Technology: Components and Devices*. 2004.

[120] J. Mork and A. Mecozzi, "Theory of the ultrafast optical response of active semiconductor waveguides," *J. Opt. Soc. Am. B*, vol. 13, pp. 1803–1816, Aug 1996.

[121] G. P. Agrawal, "Population pulsations and nondegenerate four-wave mixing in semiconductor lasers and amplifiers," *J. Opt. Soc. Am. B*, vol. 5, pp. 147–159, Jan 1988.

[122] E. Wooten, K. Kissa, A. Yi-Yan, E. Murphy, D. Lafaw, P. Hallemeier, D. Maack, D. Attanasio, D. Fritz, G. McBrien, and D. Bossi, "A review of lithium niobate modulators for fiber-optic communications systems," *Selected Topics in Quantum Electronics, IEEE Journal of*, vol. 6, pp. 69–82, Feb 2000.

[123] Y. Li, R. Wang, A. Bhardwaj, S. Ristic, and J. Bowers, "High linearity InP-based phase modulators using a Shallow Quantum-Well design," *Photonics Technology Letters, IEEE*, vol. 22, pp. 1340–1342, Sep 2010.

[124] C. E. Png, S. P. Chan, S. T. Lim, and G. T. Reed, "Optical phase modulators for MHz and GHz modulation in silicon-on-insulator (SOI)," *J. Lightwave Technol.*, vol. 22, pp. 1573–1582, Jun 2004.

[125] P. Hewitt and G. Reed, "Improving the response of optical phase modulators in SOI by computer simulation," *Lightwave Technology, Journal of*, vol. 18, pp. 443–450, Mar 2000.

[126] W.-C. Chiu, C.-C. Chang, J.-M. Wu, M.-C. M. Lee, and J.-M. Shieh, "Optical phase modulators using deformable waveguides actuated by micro-electro-mechanical systems," *Opt. Lett.*, vol. 36, pp. 1089–1091, Apr 2011.

[127] K. Van Acoleyen, J. Roels, T. Claes, D. Van Thourhout, and R. Baets, "NEMS-based optical phase modulator fabricated on silicon-on-insulator," in *Group IV Photonics (GFP), 2011 8th IEEE International Conference on*, pp. 371–373, Sep 2011.

[128] Y.-H. Lin and Y.-S. Tsou, "A polarization independent liquid crystal phase modulation adopting surface pinning effect of polymer dispersed liquid crystals," *Journal of Applied Physics*, vol. 110, p. 114516, Dec 2011.

[129] S.-K. Kim, W. Yuan, K. Geary, Y.-C. Hung, H. R. Fetterman, D.-G. Lee, C. Zhang, C. Wang, W. H. Steier, G.-C. Park, S.-J. Kang, and I. Oh, "Electro-optic phase modulator using metal-defined polymer optical waveguide," *Applied Physics Letters*, vol. 87, p. 011107, Jun 2005.

[130] R. Espinola, M. Tsai, J. Yardley, and J. R.M. Osgood, "Fast and low-power thermooptic switch on thin silicon-on-insulator," *Photonics Technology Letters, IEEE*, vol. 15, pp. 1366–1368, Oct 2003.

[131] R. Soref and B. Bennett, "Electrooptical effects in silicon," *Quantum Electronics, IEEE Journal of*, vol. 23, pp. 123–129, Jan 1987.

[132] N.-N. Feng, S. Liao, D. Feng, P. Dong, D. Zheng, H. Liang, R. Shafiiha, G. Li, J. E. Cunningham, A. V. Krishnamoorthy, and M. Asghari, "High speed carrier-depletion modulators with 1.4V-cm $V_\pi L$ integrated on 0.25μm silicon-on-insulator waveguides," *Opt. Express*, vol. 18, pp. 7994–7999, Apr 2010.

[133] Q. Xu, B. Schmidt, S. Pradhan, and M. Lipson, "Micrometre-scale silicon electro-optic modulator," *Nature*, vol. 435, pp. 325–327, May 2005.

[134] Q. Xu, S. Manipatruni, B. Schmidt, J. Shakya, and M. Lipson, "12.5 Gbit/s carrier-injection-based silicon micro-ring silicon modulators," *Opt. Express*, vol. 15, pp. 430–436, Jan 2007.

[135] S. Manipatruni, Q. Xu, B. Schmidt, J. Shakya, and M. Lipson, "High speed carrier injection 18 Gb/s silicon micro-ring electro-optic modulator," in *Lasers and Electro-Optics Society, 2007. LEOS 2007. The 20th Annual Meeting of the IEEE*, pp. 537–538, Oct 2007.

[136] K. Padmaraju, N. Ophir, Q. Xu, B. Schmidt, J. Shakya, S. Manipatruni, M. Lipson, and K. Bergman, "Error-free transmission of DPSK at 5 Gb/s using a silicon microring modulator," in *Optical Communication (ECOC), 2011 37th European Conference and Exhibition on*, pp. 1–3, Sep 2011.

[137] Y.-H. Kuo, H.-W. Chen, and J. E. Bowers, "High speed hybrid silicon evanescent electroabsorption modulator," *Opt. Express*, vol. 16, pp. 9936–9941, Jun 2008.

[138] H.-W. Chen, Y.-H. Kuo, and J. Bowers, "A hybrid Silicon-AlGaInAs phase modulator," *Photonics Technology Letters, IEEE*, vol. 20, pp. 1920–1922, Dec 2008.

[139] A. Loayssa, J. Capmany, M. Sagues, and J. Mora, "Demonstration of incoherent microwave photonic filters with all-optical complex coefficients," *Photonics Technology Letters, IEEE*, vol. 18, pp. 1744–1746, Aug 2006.

[140] M. Burla, D. Marpaung, L. Zhuang, C. Roeloffzen, M. R. Khan, A. Leinse, M. Hoekman, and R. Heideman, "On-chip CMOS compatible reconfigurable optical delay line with separate carrier tuning for microwave photonic signal processing," *Opt. Express*, vol. 19, pp. 21475–21484, Oct 2011.

[141] W. Zhang and R. Minasian, "Widely tunable single-passband microwave photonic filter based on stimulated Brillouin scattering," *Photonics Technology Letters, IEEE*, vol. 23, pp. 1775–1777, Dec 2011.

[142] T. X. H. Huang, X. Yi, and R. A. Minasian, "Single passband microwave photonic filter using continuous-time impulse response," *Opt. Express*, vol. 19, pp. 6231–6242, Mar 2011.

[143] V. R. Supradeepa, C. M. Long, R. Wu, F. Ferdous, E. Hamidi, D. E. Leaird, and A. M. Weiner, "Comb-based radiofrequency photonic filters with rapid tunability and high selectivity," *Nature Photonics*, vol. 6, pp. 186–194, Feb 2012.

[144] E. Norberg, R. Guzzon, J. Parker, L. Johansson, and L. Coldren, "A monolithic programmable optical filter for RF-signal processing," in *Microwave Photonics (MWP), 2010 IEEE Topical Meeting on*, pp. 365–368, Oct 2010.

[145] J. Sancho, J. Lloret, J. Bourderionnet, G. Lehoucq, P. Colman, S. Xavier, A. De Rossi, D. Dolfi, S. Sales, and J. Capmany, "Microwave photonic signal processor based on an integrated dispersive delay line." submitted to 2012 IEEE Topical Meeting Microwave Photonics, MWP 2012, Noordwijk, (2012).

[146] V. Sekar, M. Armendariz, and K. Entesari, "A 1.2-1.6-GHz substrate-integrated-waveguide RF MEMS tunable filter," *Microwave Theory and Techniques, IEEE Transactions on*, vol. 59, pp. 866–876, Apr 2011.